

**BUCKLING AND FREE VIBRATION OF
CYLINDRICAL PANELS UNDER NON-UNIFORM
EDGE LOADS**

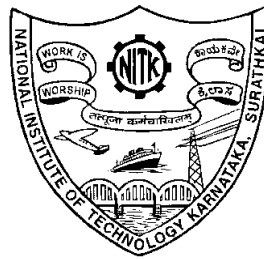
Thesis

Submitted in partial fulfilment of the requirements for the degree of

DOCTOR OF PHILOSOPHY

by

TWINKLE C M



**DEPARTMENT OF MECHANICAL ENGINEERING
NATIONAL INSTITUTE OF TECHNOLOGY KARNATAKA
SURATHKAL, MANGALURU - 575025, INDIA**

April 2023

DECLARATION

by the Ph D Reasearch Scholar

I hereby *declare* that the Research Thesis entitled “**BUCKLING AND FREE VIBRATION OF CYLINDRICAL PANELS UNDER NON-UNIFORM EDGE LOADS**” which is being submitted to the **National Institute of Technology Karnataka, Surathkal** in partial fulfilment of the requirements for the award of the Degree of **Doctor of Philosophy** in **Department of Mechanical Engineering** is a *bonafide report of the research work carried out by me*. The material contained in this Research Thesis has not been submitted to any University or Institution for the award of any degree.

Name of the Research Scholar: **TWINKLE C M**

Register No.: **197018ME017**

Signature of Research Scholar:



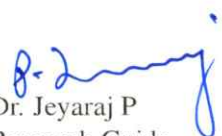
Department of Mechanical Engineering

Place: NITK - Surathkal

Date: **19-09-2023**

CERTIFICATE

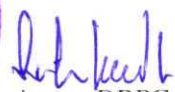
This is to *certify* that the Research Thesis entitled “**BUCKLING AND FREE VIBRATION OF CYLINDRICAL PANELS UNDER NON-UNIFORM EDGE LOADS**”, submitted by **Mr. TWINKLE C M (Register Number: 197018ME017)** as the record of the research work carried out by him, is *accepted as the Research Thesis submission* in partial fulfilment of the requirements for the award of degree of **Doctor of Philosophy**.


Dr. Jeyaraj P

Research Guide

Date: 19/04/2023




Chairman-DRPC

Date: 19.4.2023

ACKNOWLEDGEMENTS

I would like to express my sincere gratitude to my supervisor, Dr. Jeyaraj P, Associate Professor, Department of Mechanical Engineering for his guidance, support and valuable insights provided throughout my research work. I have extremely benefited from his research insights and wealth of knowledge. I am indebted to him for training me to carry forward research in my career.

I would like to thank my thesis committee members Dr. Nasar T and Dr. Mritunjay Doddamani, for their constant encouragement and valid feedbacks which has helped me to timely progress in my research work. I am also thankful to Dr. Ravikiran Kadoli, Professor and Head, Department of Mechanical Engineering for his support throughout the research work.

I would like to thank my lab mates Mr. Ashish kumar, Mr. Harsha Patil, Dr. Satheesh kumar, Mr. Nithun C, Dr. Sunil Waddar and Dr. Vijay G for constructive technical discussions which undoubtedly helped in betterment of the research work. I would like to remember M Tech students Mr. Sumodh Kumar, Mr. Amol Gilorkar and Ms. Richa Priyanka for technical discussions. I would like to thank my friends Mr. Sailesh R, Mr. Justin Antony, Mr. Neeraj M P, Mr. Arjun P S, Mr. Avinash G S and Mr. Shyamraj P for constant support and encouragement during my stay at NITK.

Many thanks to my wife, Mrs. Rosmymol vargheese for trusting me, providing immense emotional support and for sacrifices she made for carrying out my research. I would like to thank my parents, Mr. C J Monsy and Mrs. Annamma Monsy for their endless support. Thanks to my brother, Dr. Jijomon C M for his constant encouragement and my sister, Ms. Pinky C M for her continued support. Finally, I would like to dedicate this thesis to my daughter, Ms. Noella Twinkle who is my source of encouragement.

(TWINKLE C M)

ABSTRACT

Introduction of lightweight materials for different structural members of aerospace, marine, civil and automobile sectors are being made possible by utilizing nano reinforcements and addition of porosity in the bulk composite. Cylindrical curved panel structures are extensively utilized in different engineering applications owing to their better structural stability characteristics. Stability and dynamic behaviour analysis of these lightweight cylindrical panel structures is essential for the satisfactory design. In general, the buckling and dynamic characteristics of these panels are mostly studied under uniform edge load (UEL) conditions. However, the panels are exposed to non-uniform and partial edge loads in practical situation. Hence, the prediction of buckling and free vibration characteristics of the panels under different non-uniform edge loads (NELs) will help the designers in avoiding the failure of these structures.

The buckling and free vibration characteristics of different nano composite panels namely, GPL reinforced porous, GPL reinforced porous core sandwich, CNT and GOP reinforced cylindrical panels under NELs are calculated using semi analytical method in the present study. Considering a higher order shear deformation theory, Hamilton's principle is used to formulate the governing differential equations and buckling and free vibration solutions are obtained by employing the semi analytical method based on Galerkin's approach. Initially, the membrane stress resultants due to the applied edge loads are represented through Airy's stress function expansion. Then the stress resultants are evaluated through the minimisation of strain energy. Followed by this, equations of motion are obtained based on Hamilton's principle and the stress resultants. The Eigen value problems of buckling and free vibration are solved using the semi analytical method.

Buckling and free vibration characteristics of graphene nano platelets (GPL) reinforced porous cylindrical panel under the influence of NELs is studied first. The distribution of GPL and porosity is varied in a layer wise fashion through the thickness. The effective mechanical properties are calculated using extended rule of mixture together with Halpin-Tsai micromechanics model and open-cell metal foam properties. It is found that the type of NEL greatly influences the critical buckling load of the cylindrical panel. Further, the critical buckling load and natural frequency varies with a particular combination of porosity and GPL distributions.

Next, a sandwich cylindrical panel with GPL reinforced porous core and metal facing sheets is analyzed. The effective mechanical properties are obtained by using properties of open cell foams and Halpin–Tsai micro mechanical model. Effects of nature of in-plane edge load, distribution of porosity and GPL, porosity coefficient, GPL loading, core to total thickness ratio are analyzed in detail. It is found that for the panel with high core thickness, even for the higher amount of porosity, the buckling resistance and free vibration frequency can be improved by properly tailoring the graded distribution of both the GPL and pores. Furthermore, a significant variation in buckling load and free vibration frequencies is observed with respect to the type of in plane loading. Remarkable change in buckling mode and free vibration mode shape (with increase in the load intensity) is observed for panels having higher aspect ratio. The sandwich cylindrical panel with a core having a distribution of less porosity and high GPL content at the extreme surfaces provides maximum buckling strength and free vibration frequency value.

Next, buckling and free vibration characteristics of agglomerated carbon nanotubes (CNTs) reinforced nano cylindrical panels are studied considering nonlocal elasticity theory. Effective material properties of the agglomerated CNT reinforced composite are obtained using a two-parameter micro-mechanics model while Eringen's non-local theory is used to account the size effect. A comprehensive study is carried out to an-

alyze the influence of various degrees of agglomeration (complete, partial), nature of edge load , and non-local effects on the buckling and free vibration response of CNT reinforced nano cylindrical panel. The results revealed that non-local size effect leads to a reduction in stiffness and thus reduces buckling and dynamic characteristics. It is also observed that critical buckling load varies with type of in plane load. The reduction in natural frequency with increase in the edge load intensity is different for different type of NEL.

Finally, the buckling and free vibration characteristics of graphene oxide powder (GOP) reinforced cylindrical panels are studied. Influence of loading of GOP quantity, nature of grading of GOP, nature of non-uniform and partial edge loads on critical buckling coefficient and fundamental frequency and mode shapes are investigated. It is noted that the buckling and vibration characteristics are sensitive to the nature of GOP grading, GOP loading and nature of variation in edge loads. Furthermore, the fundamental buckling mode is not always the typical (1, 1) mode instead of that (2, 1) mode is observed as the buckling mode according to the variation in aspect ratio and nature of edge loads. It is found that near critical buckling load, the fundamental vibration mode changes to (2,1) from (1,1) for parabolic and partial edge loading cases for the panels with aspect ratio higher than 1.3.

KEYWORDS: Cylindrical Panel, Non-uniform Edge Loading, Buckling, Porosity, Nano composite, Functional grading

TABLE OF CONTENTS

ACKNOWLEDGEMENTS

ABSTRACT

LIST OF TABLES	ix
-----------------------	-----------

LIST OF FIGURES	xv
------------------------	-----------

NOMENCLATURE	xv
---------------------	-----------

ABBREVIATIONS	xvii
----------------------	-------------

1 INTRODUCTION	1
-----------------------	----------

1.1 Introduction	1
----------------------------	---

1.1.1 Types of Edge Loads	2
-------------------------------------	---

1.1.2 Light Weight Cylindrical Panels	3
---	---

1.1.3 Nanocomposites	4
--------------------------------	---

1.1.4 Graphene Nano Platelets (GNP) Reinforced Composites . .	5
---	---

1.1.5 Graphene Oxide Powder (GOP) Reinforced Composites . .	6
---	---

1.1.6 Carbon Nano Tube (CNT) Reinforced Composites	6
--	---

1.1.7 Porous Nano-Composites	7
--	---

1.1.8 Porous Nano-Composite Sandwich Material	8
---	---

1.2 Literature Review	8
---------------------------------	---

1.2.1 Introduction	8
------------------------------	---

1.2.2 Buckling Analysis Under Uniform and Non Uniform Edge Loads	9
--	---

1.2.2.1 Isotropic and Laminated Composites	9
--	---

1.2.2.2	Porous Cellular Materials	10
1.2.2.3	Graphene Nano Platelet (GPL) Nano-Composites	11
1.2.2.4	Porous Nano-Composites	12
1.2.2.5	Porous Nano Composite Sandwich Material . . .	12
1.2.2.6	Carbon Nano Tube (CNT) Nano-Composites . . .	13
1.2.2.7	Graphene Oxide Powder (GOP) Nano-Composites	14
1.2.3	Free Vibration Analysis	15
1.2.3.1	Isotropic and Laminated Composites	15
1.2.3.2	Porous Cellular Materials	16
1.2.3.3	Graphene Nano Platelet (GPL) Nano-Composites	17
1.2.3.4	Porous Nano-Composites	18
1.2.3.5	Carbon Nano Tube (CNT) Nano-Composites . . .	19
1.2.3.6	Graphene Oxide Powder (GOP) Nano-Composites	21
1.2.4	Closure	22
1.3	Objectives and Scope of Study	23
1.4	Outline of the Thesis	24
2	METHODOLOGY	26
2.1	Introduction	26
2.2	Analysis Approach	26
2.3	Formulation	27
2.4	Solution Procedure	33
2.4.1	Pre-Buckling Analysis	35
2.4.2	Semi-Analytical Procedure	38
2.5	Validation	40
2.5.1	Buckling Load Calculation	41
2.5.2	Free Vibration Frequency Calculation	42
2.6	Closure	42

3	FREE VIBRATION-BUCKLING ANALYSIS ON GPL-POROUS CYLINDRICAL PANEL	45
3.1	Introduction	45
3.2	Modelling of GPL-Porous Cylindrical Panel	45
3.3	Validation of the Material Modelling	50
3.4	Free Vibration and Buckling Characteristics for GPL-Porous Cylindrical Panel	51
3.4.1	Buckling Studies	51
3.4.2	Free Vibration Studies	57
3.5	Closure	64
4	FREE VIBRATION-BUCKLING ANALYSIS ON GPL-POROUS SANDWICH CYLINDRICAL PANEL	65
4.1	Introduction	65
4.2	Modelling of Sandwich Cylindrical Panel with GPL-Porous Core	65
4.2.1	Mathematical Material Modelling	65
4.2.2	Inertia and Stiffness Coefficients	71
4.3	Validation of Sandwich Material Modelling	73
4.4	Free Vibration and Buckling Characteristics for GPL-Porous Sandwich Cylindrical Panel	75
4.4.1	Buckling Studies	75
4.4.2	Free Vibration Studies	86
4.5	Closure	92
5	FREE VIBRATION-BUCKLING ANALYSIS ON CNT REINFORCED CYLINDRICAL PANEL	94
5.1	Introduction	94
5.2	Non-Local Elasticity Modelling of CNT Reinforced Cylindrical Panel	94
5.2.1	Mathematical Material Modelling	94
5.2.2	Nonlocal Elasticity Theory	98
5.3	Validation	99

5.3.1	Verification of Material Properties Estimation	100
5.3.2	Buckling Load Calculation	100
5.3.3	Free Vibration Frequency Calculation	102
5.4	Free Vibration and Buckling Characteristics for CNT Reinforced Cylindrical Panel	103
5.4.1	Buckling Analysis	103
5.4.2	Free Vibration Analysis	110
5.5	Closure	113
6	FREE VIBRATION-BUCKLING ANALYSIS ON GOP REINFORCED CYLINDRICAL PANEL	116
6.1	Introduction	116
6.2	Material Modelling of GOP Reinforced Composite	116
6.3	Validation of Material Modelling	118
6.4	Free Vibration and Buckling Characteristics for GOP Reinforced Cylindrical Panel	120
6.4.1	Buckling Studies	120
6.4.1.1	Influence of GOP Distribution and Its Volume Fraction	121
6.4.1.2	Influence of Aspect Ratio	123
6.4.2	Free Vibration Studies	124
6.4.2.1	Influence of GOP Volume Fraction and Its Distribution	125
6.4.2.2	Influence of Type of NEL and Aspect Ratio	126
6.4.2.3	Comparison of Buckling Loads for Different Types of Nano Filler Reinforced Cylindrical Panels	129
6.5	Closure	132
7	SUMMARY AND CONCLUSIONS	136
7.1	Summary	136
7.2	Conclusions	137

7.2.1	Free Vibration-Buckling Analysis on GPL-Porous Cylindrical Panel	137
7.2.2	Free Vibration-Buckling Analysis on GPL-Porous Sandwich Cylindrical Panel	138
7.2.3	Free Vibration-Buckling Analysis on CNT Reinforced Cylindrical Panel	139
7.2.4	Free Vibration-Buckling Analysis on GOP Reinforced Cylindrical Panel	139
7.3	Scope for Future Work	141
	REFERENCES	142
	LIST OF PUBLICATIONS	158
	CURRICULUM VITAE	160

LIST OF TABLES

2.1	Different materials and properties used in the present study	33
2.2	Comparison of critical buckling load $\left(\bar{N}_0 = N_{cr}\left(\frac{b^2}{\pi^2 D}\right); D = \frac{Eh^3}{12(1-\nu^2)}\right)$ of a SSSS square isotropic plate under different NELs.	41
2.3	Buckling load $\left(\bar{N}_0 = N_{cr}\left(\frac{b}{D}\right); D = \frac{Eh^3}{12(1-\nu^2)}\right)$ validation for an isotropic plate simply supported (SSSS) at its ends under partial edge loading.	41
2.4	Comparison of non-dimensional fundamental frequency $\left(\Omega = \omega_n\left(\frac{a^2}{h}\sqrt{\frac{\rho_m}{E_m}}\right)\right)$ of an isotropic cylindrical panel $\left(\frac{a}{b} = 1, \frac{a}{h} = 20\right)$ and $R = 10m$) with Van Do and Lee (2020)	42
3.1	Alternate naming for different distributions	46
3.2	Variations of material properties for different types of porosity distributions	48
3.3	Porosity coefficients for different distributions	50
3.4	Comparison of dimensionless fundamental frequency $\left(\Omega = \omega_n a\left(\sqrt{\frac{I^*}{A^*}}\right)\right)$ for GPL reinforced porous nano composite plate under different boundary conditions $(a/b=1, a/h=20, \Lambda_{GPL} = 1.0wt\%, e_0 = 0.5)$	52
3.5	Different combinations in distributions of porosity and GPL	53
3.6	Buckling coefficients $\left(\frac{N_{cr}b^2}{100E^m h^3}\right)$ for GPL reinforced porous nano composite cylindrical panel under SSSS boundary condition $\left(\frac{a}{b} = 1, \frac{a}{h} = 20, \Lambda_{GPL} = 1.0wt\%, e_0 = 0.4\right)$ subject to different inplane loadings	55
3.7	Non-dimensional frequency $\left(\Omega = \omega_n\left(\frac{a^2}{h}\sqrt{\frac{\rho_m}{E_m}}\right)\right)$ for GPL reinforced porous nano composite cylindrical panel under different boundary condition $(a/b=1, a/h=20, \Lambda_{GPL} = 1.0wt\%, e_0 = 0.4)$	58

4.1	Naming for different distributions	66
4.2	Porosity coefficients for different distributions	69
4.3	Comparison of critical buckling values $\bar{N}_0 = N_{cr}(\frac{b^2}{100h^3E_m})$ of open foam cell core sandwich flat panel under uni-axial compression with Yaghoobi and Taheri (2020)	74
4.4	Buckling coefficient value of GPL reinforced porous sandwich cylindrical panel subjected to different NELs under SSSS boundary condition($\frac{a}{b} = 1, e_o = 0.4, \Lambda_{GPL} = 1wt\%, \frac{h_c}{h_t}=0.8$) : variation with radius ratio ($\frac{R}{a}$)	76
4.5	Buckling coefficient value of GPL reinforced porous sandwich cylindrical panel subjected to different NELs under SSSS boundary condition($\frac{a}{b} = 1, e_o = 0.4, \Lambda_{GPL} = 1wt\%, \frac{R}{a} = 20$) : variation with core to total thickness ratio($\frac{h_c}{h_t}$)	78
4.6	Non-dimensional fundamental frequency of GPL reinforced porous sandwich cylindrical under different boundary condition($\frac{a}{b} = 1, e_o = 0.4, \Lambda_{GPL} = 1wt\%, \frac{h_c}{h_t}=0.8$) : variation with radius ratio ($\frac{R}{a}$)	88
4.7	Non-dimensional frequency of GPL reinforced porous sandwich cylindrical under different boundary condition($\frac{a}{b} = 1, e_o = 0.4, \Lambda_{GPL} = 1wt\%, \frac{R}{a} = 20$) : variation with core to total thickness ratio($\frac{h_c}{h_t}$)	89
5.1	Comparison of Young's modulus of completely agglomerated CNTs ($\eta = 1$) reinforced composite with Bisheh <i>et al.</i> (2020) for different agglomeration parameter	101
5.2	Comparison of Young's modulus of partially agglomerated CNTs ($\epsilon = 0.5$) reinforced composite with Bisheh <i>et al.</i> (2020) for different agglomeration parameters	101
5.3	Elastic properties comparison of composite reinforced with uniformly dispersed CNTs ($\epsilon = \eta = 1$)	101
5.4	Comparison of buckling coefficients $\left(\frac{N_{cr}a^2}{D}\right)$ for CNT reinforced simply supported flat panels with Hosseini-Hashemi <i>et al.</i> (2015)	102
5.5	Non-dimensional frequency $\left(\Omega = \omega_n\left(\frac{a^2}{h}\sqrt{\frac{\rho_m}{E_m}}\right)\right)$ for CNT reinforced simply supported flat panels with Phung-Van <i>et al.</i> (2017)	102
5.6	Properties of matrix and CNT(Chakraborty <i>et al.</i> 2019; Shi <i>et al.</i> 2004)	103
5.7	Buckling coefficients $\left(\frac{N_{cr}b^2}{100\rho_r h^3}\right)$ for CNT reinforced nano composite cylindrical panel under SSSS boundary condition($a/b=1, a/h=20, r_v = 0.1$)subject to different NELs	105

5.8	Non-dimensional frequency ($\Omega = \omega_n \left(\frac{a^2}{h} \sqrt{\frac{\rho_m}{\rho_r}} \right)$) for CNT reinforced nano composite cylindrical panel under SSSS boundary condition ($a/b=1$, $a/h=20$, $r_v = 0.1$).	112
-----	---	-----

LIST OF FIGURES

1.1	Different types of edge loads	3
1.2	Graphene-1 layer molecular model (Young <i>et al.</i> 2012)	5
2.1	Flow chart of the present work	27
2.2	Geometry and coordinate system of the cylindrical panel studied. . .	28
2.3	Different types of loadings considered	35
3.1	Different GPL patterns	46
3.2	Different porosity distributions	47
3.3	Variation of material properties for different porosity distributions .	47
3.4	Buckling coefficients $\left(\frac{N_{cr}b^2}{100E^m h^3}\right)$ for GPL reinforced porous nano composite cylindrical panel under SSSS boundary condition($a/b=1$, $a/h=20$, $\Lambda_{GPL} = 1.0wt\%$, $R=20$): effect of porosity coefficient	56
3.5	Buckling coefficients $\left(\frac{N_{cr}b^2}{100E^m h^3}\right)$ for GPL reinforced porous nano composite cylindrical panel under SSSS boundary condition($a/b=1$, $a/h=20$, $e_0 = 0.4$, $R=20$): effect of graphene grading	59
3.6	Buckling coefficients $\left(\frac{N_{cr}b^2}{100E^m h^3}\right)$ for GPL reinforced porous nano composite cylindrical panel under SSSS boundary condition($a/b=1$, $a/h=20$, $e_0 = 0.4$, $R=20$): effect of aspect ratio	60
3.7	Non-dimensional frequency ($\Omega = \omega_n(\frac{a^2}{h} \sqrt{\frac{\rho_m}{E_m}})$) for GPL reinforced porous nano composite cylindrical panel under different boundary condition($\frac{a}{b} = 1$, $\frac{a}{h} = 20$, $\Lambda_{GPL} = 1.0wt\%$, $e_0 = 0.4$, $\frac{R}{a} = 20$): effect of porosity coefficient	61
3.8	Effect of compressive load on the non-dimensional frequency ($\Omega = \omega_n(\frac{a^2}{h} \sqrt{\frac{\rho_m}{E_m}})$) for GPL reinforced porous SSSS nano composite cylindrical panel for all the type of loadings.	62

3.9	Effect of type of edge load on the on-dimensional frequency ($\Omega = \omega_n(\frac{a^2}{h} \sqrt{\frac{\rho_m}{E_m}})$) for GPL reinforced porous SSSS nano composite cylindrical panel	63
4.1	Cylindrical sandwich panel with porous FG-GPL core	66
4.2	Metal foam core with different types of graded porosity	67
4.3	Core with different types of GPL patterns	67
4.4	Variation in buckling coefficient value with core to total thickness ($\frac{h_c}{h_t}$) of GPL reinforced porous sandwich cylindrical panel subjected to uniform edge load under SSSS boundary condition($\frac{a}{b} = 1, e_o = 0.4, \Lambda_{GPL} = 1wt\%, \frac{R}{a} = 20$)	79
4.5	3D surface plots of buckling coefficient of sandwich cylindrical panel indicating the effect of GPL weight fraction and core to total thickness ratio under uniform loading (Case-a) (a)porosity coefficient(e_0)=0.2 (b)porosity coefficient(e_0)=0.6	80
4.6	3D surface plots of buckling coefficient of sandwich cylindrical panel indicating the effect of GPL weight fraction and core to total thickness ratio under trapezoidal loading (Case-b) (a)porosity coefficient(e_0)=0.2 (b)porosity coefficient(e_0)=0.6	81
4.7	3D surface plots of buckling coefficient of sandwich cylindrical panel indicating the effect of GPL weight fraction and core to total thickness ratio under parabolic loading (Case-e) (a)porosity coefficient(e_0)=0.2 (b)porosity coefficient(e_0)=0.6	82
4.8	Variation of buckling coefficient of GPL reinforced sandwich panel under SSSS boundary condition subject to uniform edge loading($e_o = 0.4, \Lambda_{GPL} = 1wt\%, \frac{h_c}{h_t}=0.8$ and $\frac{R}{a} = 20$): effect of aspect ratio	83
4.9	Variation of buckling coefficient of D-PD & I-GPL-P sandwich panel under SSSS boundary condition subject to uniform, NEL-I ($e_o = 0.4, \Lambda_{GPL} = 1wt\%, \frac{h_c}{h_t}=0.8$ and $\frac{R}{a} = 20$): effect of aspect ratio	84
4.10	Variation of buckling coefficient of D-PD & I-GPL-P sandwich panel under SSSS boundary condition subject to uniform, NEL-II ($e_o = 0.4, \Lambda_{GPL} = 1wt\%, \frac{h_c}{h_t}=0.8$ and $\frac{R}{a} = 20$): effect of aspect ratio	85
4.11	Buckling mode of D-PD & I-GPL-P sandwich panel for aspect ratio $a/b=1.2$ for uniform and different edge loads (Parabolic, Reverse Sinusoidal, Increasing Parabolic.)	86

4.12	Buckling mode of D-PD & I-GPL-P sandwich panel for aspect ratio $a/b=1.6$ for (a) Uniform (b) Parabolic (c) Reverse Sinusoidal (d) Increasing Parabolic.	87
4.13	3D surface plots of non dimensional frequency of sandwich cylindrical panel indicating the effect of GPL weight fraction and core to total thickness ratio under uniform loading (a)porosity coefficient(e_0)=0.2 (b)porosity coefficient(e_0)=0.6	90
4.14	Variation of non-dimensional frequency with uniform compressive load for GPL reinforced porous sandwich cylindrical panel under SSSS boundary condition	91
4.15	Variation of non-dimensional frequency with compressive load of D-PD & I-GPL-P sandwich panel under SSSS boundary condition subject to uniform, linearly and non-linearly varying in-plane compressive loads.	91
5.1	CNT bundling model with agglomeration	95
5.2	The variation of material properties of a partially agglomerated ($\epsilon = 0.5$) CNT reinforced cylindrical panel with increase in agglomeration parameter η	98
5.3	Schematic representation of different level of agglomeration	104
5.4	Effect of a) non-local parameter(μ) b) radius ratio($\frac{R}{a}$) c)agglomeration on buckling coefficient ($\frac{N_{cr}b^2}{100p_rh^3}$) for different type of loading.	106
5.5	Variation of buckling coefficient ($\frac{N_{cr}b^2}{100p_rh^3}$) considering complete agglomeration ($\eta = 1$) with change in agglomeration parameter(ϵ) for different CNT volume fractions(v_r)	108
5.6	Variation of buckling coefficient ($\frac{N_{cr}b^2}{100p_rh^3}$) considering partial agglomeration ($\epsilon = 0.5$) with change in agglomeration parameter(η) for different CNT volume fractions(v_r)	109
5.7	Variation of buckling coefficient ($\frac{N_{cr}b^2}{100p_rh^3}$) considering full agglomeration ($\eta = 1$) with change in non-local parameter(μ) for different combinations of ϵ and η	110
5.8	Variation of buckling coefficient ($N_{cr}b^2/100p_rh^3$) considering partial agglomeration ($\epsilon = 0.5$) with change in non-local parameter(μ) for different combinations of ϵ and η	111
5.9	Variation of non-dimensional frequency ($\Omega = \omega_n(\frac{a^2}{h} \sqrt{\frac{\rho_m}{p_r}})$) considering partial agglomeration ($\epsilon = 0.5$) with change in agglomeration parameter(η) for different CNT volume fractions(v_r)	113

5.10	Effect of compressive load on non-dimensional frequency ($\Omega = \omega_n(\frac{a^2}{h} \sqrt{\frac{\rho_m}{p_r}})$) of SSSS cylindrical panel for all the type of loadings	114
5.11	Effect of compressive load on non-dimensional frequency ($\Omega = \omega_n(\frac{a^2}{h} \sqrt{\frac{\rho_m}{p_r}})$) of uniformly distributed CNT reinforced cylindrical panel under SSSS boundary condition for different loadings	115
6.1	Different types of GOP distribution patterns	117
6.2	Comparison of dimensionless buckling load ($\bar{N}_0 = N_{cr}(\frac{R\sqrt{3(1-\nu_m)}}{100E_m h^3})$) of SSSS GOP cylindrical shell	119
6.3	Buckling coefficients ($N_{cr}(\frac{b^2}{100E_m h^3})$) for a square, SSSS, GOP reinforced nano composite cylindrical panel under different edge loading: Influence of various distribution and weight fraction of GOP.	122
6.4	Increase of buckling coefficients ($N_{cr}(\frac{b^2}{100E_m h^3})$) for various distributions of GOP (SSSS square cylindrical panel) with increase in GOP content (a)uniform loading (b)partial edge loading.	123
6.5	Variation of buckling coefficients ($N_{cr}(\frac{b^2}{100E_m h^3})$) for simply supported, GOP reinforced cylindrical panel subjected different edge loading: Influence of aspect ratio	125
6.6	Variation of buckling coefficients ($N_{cr}(\frac{b^2}{100E_m h^3})$) with aspect ratio for a simply supported, GOP reinforced cylindrical panel under X-GOPRC distribution: Influence of edge loading.	126
6.7	Variation of non dimensional frequency ($\Omega = \omega(\frac{a^2}{h} \sqrt{\frac{\rho_m}{E_m}})$) of clamped and simply supported GOP reinforced cylindrical panel: Influence of various distribution and weight fraction of GOP.	127
6.8	Non dimensional frequency ($\Omega = \omega_n(\frac{a^2}{h} \sqrt{\frac{\rho_m}{E_m}})$) change for a simply supported GOP reinforced cylindrical panel(aspect ratio 1) : Influence of increase in compressive load.	128
6.9	Non dimensional frequency ($\Omega = \omega_n(\frac{a^2}{h} \sqrt{\frac{\rho_m}{E_m}})$) change for a simply supported GOP reinforced cylindrical panel (aspect ratio 1.3) : Influence of increase in compressive load.	130
6.10	Comparison of buckling load per unit mass ($\frac{N_{cr}}{I_{1ab}}$) for different nano composite cylindrical panels.	131
6.11	Comparison of buckling load per unit mass ($\frac{N_{cr}}{I_{1ab}}$) for different nano composite cylindrical panels.	133

NOMENCLATURE

$[K]$	Stiffness matrix of the cylindrical panel
a, b	Length and width of the cylindrical panel
$[K_G]$	Geometric stiffness matrix of the cylindrical panel
R	Radius of curvature of the cylindrical panel
h	Thickness of the cylindrical panel
$[M]$	Mass matrix of the cylindrical panel
u_0, v_0	Displacement of the mid plane in x and y directions
E	Young's modulus
G	Shear modulus
w_0	Displacement of the mid plane in z direction
ν	Poisson's ratio
ρ	Density
N_0	Highest intensity value of the load
\bar{N}_0	Buckling coefficient
ω	Circular frequency
Ω	Non-dimensional frequency
N_{cr}	Critical buckling load
r, s	Number of half waves in x and y directions
ϵ_{xx}	Normal strain in x direction
γ_{xy}	Shear strain in in-plane direction
ϵ_{yy}	Normal strain in y direction
γ_{xz}, γ_{yz}	Shear strains in transverse directions
ω_n	Circular natural frequency
n_{xx}	In-plane stress resultant in x direction

n_{yy}	In-plane stress resultant in y direction
n_{xy}	In-plane stress resultants in x-y direction
δ	Variational operator
σ_{xx}	Normal stress in x direction
τ_{xy}	Shear stress in in-plane direction
σ_{yy}	Normal stress in y direction
τ_{xz}, τ_{yz}	Shear stress in transverse directions
δK	Kinetic energy
δU	Strain energy
$\aleph(x, y)$	Stress function

ABBREVIATIONS

GPL	Graphene nano platelet
PD	Porosity distribution
CNT	Carbon nano tube
CVD	Chemical vapour deposition
GPa	Gigapascal
NEMS	Nano electro mechanical systems
2D	Two dimensional
MEMS	Micro electro mechanical systems
3D	Three dimensional
GOP	Graphene oxide powder
FGM	Functionally graded material
FEM	Finite element method
HSDT	Higher order shear deformation theory
SSDT	Sinusoidal shear deformation theory
NEL	Non-uniform edge load
UEL	Uniform edge load

CHAPTER 1

INTRODUCTION

1.1 Introduction

Thin walled cylindrical panels are extensively used as structural members in high speed rail, automotive, aerospace and marine industries. These curved cylindrical panel structures, due to the presence of curvature, provides higher in plane load resistance compared to flat panels thereby gaining practical significance. When these cylindrical panels are subjected to edge compressive loads, a sudden change in shape can happen at a certain level of load and this phenomenon is known as buckling. By definition, for a structural element, the sudden change in present state of equilibrium to unstable from stable happens at a particular value of load known as buckling load (Jones 2006). In other words, the sudden change of equilibrium state to a distinctive stable configuration from former stable configuration happens at the buckling load whether or not followed by a large deformation (Jones 2006). Imagine the cylindrical panel like structural elements of an aircraft, ship or high-speed train changes its shape suddenly while in service. These sudden shape changes can cause change in dynamic performance leading to high fuel consumption, passenger discomfort or even failure. Hence, the buckling phenomenon is undesirable and need to be analysed for better design of structures.

The free vibration characteristics namely, natural frequency and mode shapes of structural members are properties of the system established by distribution of mass and stiffness (Thomson 2018). The consideration of natural frequency is important due to the fact that whenever an excitation frequency matches with the natural frequency, resonance will happen. The resonance is the condition in which the amplitude of vibration becomes dangerously high. Consider the practical situation in which an automobile or

an aircraft cylindrical panel member is excited by external load at natural frequency. The resulting high amplitude of vibration causes noise, passenger discomfort or even failure.

The prime source of compressive edge loadings in the cylindrical panel is by the process of load bearing/transfer. However, these edge loadings vary in magnitude along the length or width of the cylindrical panel due to the process of load distribution and lead to non-uniform distribution of loads. For instance, the wings of the aircraft and stiffened plates in ship structures are practical examples in which structures are subjected to non uniform edge loads (Hamedani and Ranji 2013). The in plane stresses developed due to these edge loads induces buckling and may change the free vibration characteristics of the cylindrical panel structure. In literature, however most of the studies are carried out by assuming uniform edge load (UEL) assumption. The important aspect of structures subjected to compressive edge loads is that the presence edge loads alters the stiffness resulting in changes of natural frequency. Thus analysis of free vibration characteristics of structures under the influence of the non-uniform edge load (NEL) is very important.

1.1.1 Types of Edge Loads

The cylindrical panel structures, are typically exposed to different types of edge loadings such as : uniform, trapezoidal, triangular, partial tension, parabolic, reverse sinusoidal, increasing parabolic, partial edge loadings as shown in Figure 1.1. In actual operating conditions, highly localised stresses are developed in structures due to high speed and high temperature which will lead to different non uniform edge loads (Adhikari *et al.* 2020).

For a cylindrical panel structure in service, the loads leading to buckling are applied by adjoining free-body. The uniform edge loading is an exception to different type of loads since relative stiffness determines the elastic forces between free-bodies (Jana

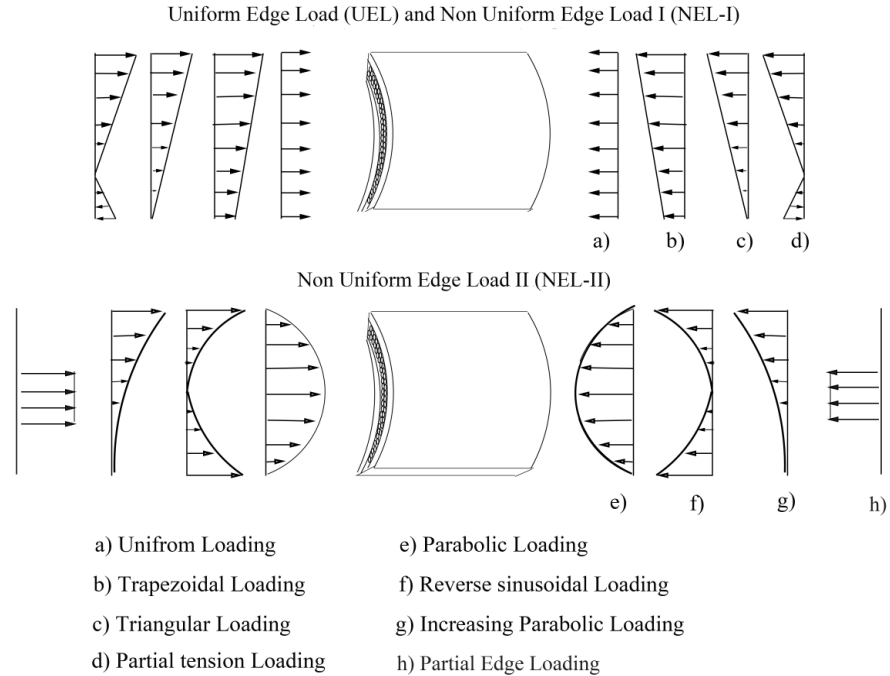


Figure 1.1: Different types of edge loads

and Bhaskar 2006). Shariyat and Asemi (2014), reported that generally the edge loads applied by surrounding elements on plate or cylindrical panel regions are non-linear in nature. Thus, consideration of different non-uniform edge loadings is important for complete understanding of the buckling and free vibration behaviour.

1.1.2 Light Weight Cylindrical Panels

Cylindrical panel members used in various engineering applications can be made light in weight to facilitate the energy savings (less fuel consumption) and ultimately less environmental impacts (less emissions). The question of light weight cylindrical panel structures being asked by researchers over the years is answered by using thin walled structures with preferably stiffer materials. By using stiffer materials, the light weight structural members are made possible without compromising the stiffness. The nano

composites and porous nano composites are emerged as solutions to this problem by making use of the material property at the nano levels to achieve better strengths to the bulk composite.

1.1.3 Nanocomposites

Nanocomposites can be defined as multiphase materials made up of a matrix phase and at least one nano-filler phase to achieve a combination of properties of its individual phases (Safdari and Al-Haik 2018). Several nano-scale reinforcements such as carbon nano tubes (CNT), graphene nano platelets (GPL) and graphene oxide powder (GOP) can be used together with metal matrix or polymeric matrix to obtain exceptional mechanical properties. Nano composites have additional benefits such as controlled anisotropy and tailorability of mechanical properties (Dzenis 2008). The nano composites can be prepared with the development of advanced manufacturing methods to incorporate nano scale reinforcements in the matrix and used with proper structural design in several applications. Thus low cost lightweight alternative structures with exceptional properties can be obtained with nano reinforcements.

There are possible issues associated with nano composites such as problems in dispersion, alignment, achievable volume fraction of reinforcement, bonding and interfaces of composites. These issues will lead to degradation of mechanical properties of the composite. The nano composites are widely used in fuel efficient cars, aerospace, auto-mobile and sporting goods. Thus the consideration of agglomeration associated with the dispersion of nano composites is necessary.

Some confined and small sized structures would actually benefit from the performance enhancement and tailorability provided by nano composites because of the small size. These include structural elements in NEMS/MEMS (nano- and microelectro mechanical systems) and thin walls present in foams (Safdari and Al-Haik 2018).

1.1.4 Graphene Nano Platelets (GNP) Reinforced Composites

The graphitic materials extracted from a single layer of graphene to platelets of 100nm thickness are included in the definition of graphite nano platelets (Young *et al.* 2012). Figure 4.1 shows the molecular model of a single graphene layer. The graphite nano platelets are produced by different methods including ball milling, ultrasonication and by microwave radiation exposure to graphite intercalated with acid. The availability of GNP as a single layer graphene nano platelets (GPL) has gained much interest in the scientific community. The single layer of graphene has exceptional mechanical properties as reported by indentation experiment: Young's modulus = 1000 ± 100 GPa by Lee *et al.* (2008) and estimated using theoretical approach as 1050 GPa by Liu *et al.* (2007).

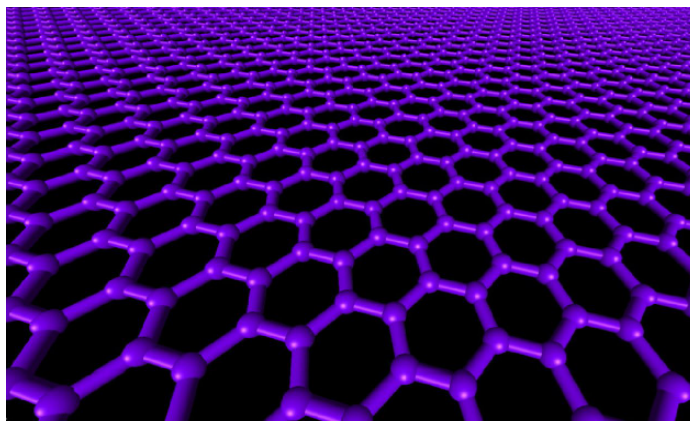


Figure 1.2: Graphene-1 layer molecular model (Young *et al.* 2012)

The interest in the development of GPL reinforced composites is due to several reasons. The prime reason being its ability to impart better load carrying capacity even with very low concentrations (Rafiee *et al.* 2009; Liu *et al.* 2013). Additionally, improvement in other properties such as thermal conductivity, barrier nature and electrical conductivity is an advantage. The possible issues associated with the GPL composites are, non-uniform dispersion of GPL in the matrix are poor exfoliation, restacking occurrence and poor interface bonding. These issues can cause a significant reduction in

mechanical properties. Even though there are possible issues associated with GPL, it can be used with ease as reinforcements of thin walls of open cell foams so that higher strengths can be obtained with lower concentrations.

1.1.5 Graphene Oxide Powder (GOP) Reinforced Composites

Graphene oxide by definition is the oxidised form of graphene which is found as a combination of individual graphene oxide sheets. The preparation of graphene oxide is done by different methods but the method proposed by Hummers Jr and Offeman (1958) is the efficient one which uses a water free mix of potassium permanganate, concentrated sulphuric acid and sodium nitrate to treat the graphite. The mechanical properties of GOP are lower compared to GPL due to several reasons such as the replacing of sp^2 with sp^3 bonding and changes in the structure due to oxidation. The equivalent Young's modulus of graphene oxide is 480 GPa as predicted by Suk *et al.* (2010). However, there are several advantages associated with usage of GOP such as its availability in large quantities because of the scalability of manufacturing process, ability to form better interfaces with polymer matrix because of the presence of functional groups and ease of dispersion and exfoliation in the matrix (Young *et al.* 2012). The graphene oxide has major advantage in terms of preparation of composites that it can be exfoliated using water and the nano-composites can be prepared using water soluble polymers. Another method is by in-situ polymerisation of the polymer matrix. With epoxy resins, intercalative polymerisation can be achieved for producing nano composite with enhanced properties (Young *et al.* 2012). Thus graphene oxide can be used together with polymeric matrix to produce advanced lightweight composites.

1.1.6 Carbon Nano Tube (CNT) Reinforced Composites

The CNTs are found as cylindrical rolled up form of graphene sheets. The CNTs are generally classified as (1) single walled nano tubes where a single layer of graphene

is to form the cylindrical roll, (2) multi walled nano tubes where multiple concentric rolled cylinders with 0.34 nm interlayer spacing is found. The CNTs are widely manufactured by methods such as laser ablation, CVD (chemical vapour deposition) and arc evaporation methods (Mittal *et al.* 2015). The excellent mechanical properties of CNTs (Yakobson and Avouris 2001; Qian *et al.* 2002; Reich *et al.* 2008) such as high Young's modulus, high tensile strength, and low density and enhancement of mechanical properties of bulk composite on addition of CNT (Coleman *et al.* 2006; Qian *et al.* 2000; Haggemueller *et al.* 2000; Velasco-Santos *et al.* 2003) is already reported in the literature.

The problem of uniform dispersion is associated with CNTs due to Van-der-Waals forces, high aspect ratio, and low bending stiffness. The CNTs tend to bundle together and it is called as agglomeration. Thus CNT agglomeration tend to reduce overall mechanical properties considerably. CNTs can be utilised with ease in nano/micro electromechanical systems to enhance their mechanical performance. However, the consideration of size effects is important in the design of nano scaled structures. In general, when comparable characteristic lengths exist, the classical continuum theories (2D & 3D) becomes non applicable. Various non-classical continuum theories containing material length scale parameters have been proposed over the years. The non-local elasticity theory (Eringen 1972, 1983, 2002) is the widely used one, which specifies that the stress at the point of consideration accounts not only for strain at that point but also for strain at all points in the domain.

1.1.7 Porous Nano-Composites

The metal foams are identified as an advanced class of materials with high stiffness to weight ratio, high energy absorption capabilities and very low density. The closed cell foams and open cell foams are the two class of foams available. In open cell foams, the cells are only interconnected not closed but in closed cell foams, cells are enclosed by thin walls (Ashby *et al.* 2000).

Along with these advantages, however, there are some limitations associated with metal foams such as loss in stiffness due to the presence of porosity. The loss in stiffness can be regained by the addition of nano reinforcements which will maintain the inherent advantages such as light weight nature. Due to the specific advantages, the porous nano composites can be utilized in high speed rail applications (high damping and improved stiffness), aerospace applications (light weight and high stiffness), floor panels (high stiffness and light weight), and also as automobile energy absorbing panels (Smith *et al.* 2012; Li *et al.* 2018).

1.1.8 Porous Nano-Composite Sandwich Material

Porous nano composite sandwich is a material having metal face sheets and GPL reinforced porous core which has potential applications in marine, aerospace and automobile industries (Banhart 2005; Banhart *et al.* 2019). Compared to conventional sandwich panels where core and face sheets are glued together, the metallic nature of porous nano composite sandwich is an advantage.

1.2 Literature Review

1.2.1 Introduction

The focus of the thesis is the analysis of buckling and free vibration response of cylindrical panel reinforced with nano reinforcements under the influence of NELs. The review is organised with GPL reinforced structures first, followed by CNT reinforced structures then by GOP reinforced structures. The literature review is organised in such a way that buckling studies under uniform and non-uniform edge loading is discussed first. This is followed by free vibration characteristics with and without the influence of uniform and NELs.

1.2.2 Buckling Analysis Under Uniform and Non Uniform Edge Loads

1.2.2.1 Isotropic and Laminated Composites

Leissa and Kang (2002) studied free vibration and buckling characteristics of plates under different boundary conditions subjected to different linearly varying NELs using power series solution method. They established the usage of power series method for the buckling and free vibration analysis of plates under different boundary conditions.

Kang and Leissa (2005) presented an exact method for buckling analysis of rectangular plates subjected to linearly varying NELs using power series. Their solutions are non applicable for a non-general non-uniform edge loading conditions other than that of linearly varying edge loads.

Panda and Ramachandra (2010) investigated buckling characteristics of isotropic and laminated composite plates under different NELs using Galerkin's method. They proposed a more general method of solution for obtaining buckling characteristics of plate structures.

Hamedani and Ranji (2013) analysed buckling characteristics of stiffened plates subjected to NELs using finite element method. They found that critical buckling load is influenced by the type of edge loading.

Dey and Ramachandra (2014) studied the influence of partial edge loadings for post buckling and dynamic instability of composite cylindrical panels using Galerkin's method. It is observed that the partial edge loading applied in longitudinal direction leads to behaviour of cylindrical panel as an imperfect panel.

Abolghasemi *et al.* (2019) analysed buckling characteristics of an isotropic plate with a hole subjected to uniform and non-uniform (parabolic and sinusoidal) edge loadings using analytical method. They observed that buckling characteristics are influenced by the type of edge loading.

Adhikari and Singh (2020) investigated the dynamic instability of laminated composite plate subjected to NELs using finite element method. The instability behaviour of composite plate varies in such a way that highest impact is for parabolic loading followed by sinusoidal loading then by reverse sinusoidal loading.

Watts *et al.* (2021) studied buckling and dynamic instability characteristics of laminated composite and isotropic plates subjected to NELs using element free Galerkin method. They observed that the critical buckling load of trapezoidal plate depends on the type of edge loading.

1.2.2.2 Porous Cellular Materials

Pollien *et al.* (2005) demonstrated production of functionally graded porous structures with graded porosity. The study indicate that lightweight graded beams exhibit more promise in the stand point of load-limited design.

Magnucka-Blandzi (2008) investigated buckling characteristics of circular porous-cellular plate using Galerkin's method. They demonstrated decrease in critical buckling load with increase in porosity of the plate.

Thang *et al.* (2018) studied buckling characteristics of porous metal foam plates subjected to UEL using an analytical method. They observed that increase in porosity leads to reduction in critical buckling load due to loss in the structural stiffness.

Wang and Zhang (2019) analysed buckling characteristics of porous metal foam plates subjected UEL using Galerkin's method. The observed the variation in critical buckling load with respect to the changes in the porosity distribution through the thickness.

Li *et al.* (2019d) studied buckling characteristics of GPL reinforced porous arches using analytical methods. Their study reveals that the increase in porosity content reduces the critical buckling load. They also observed that the increase in GPL content

increases the critical buckling load significantly.

Toan Thang *et al.* (2020) investigated buckling and post buckling characteristics of metal foam cylindrical shells under uniform edge compression using Galerkin's method. They observed a reduction in critical buckling load with increase in porosity in the cylindrical panel.

1.2.2.3 Graphene Nano Platelet (GPL) Nano-Composites

Liu *et al.* (2018) studied buckling characteristics of GPL reinforced cylindrical shells using analytical methods. The results of the study indicate that the distribution of increasing concentration of GPL towards extreme surfaces improves the critical buckling load.

Ebrahimi and Barati (2018) analysed free vibration analysis of single layer graphene sheets subjected to NELs using Galerkin's method. They have considered the strain gradient elasticity theory to include the influence of non-local and strain-gradient effects. It is observed that the natural frequency reduces with increase in the edge load intensity.

Song *et al.* (2018) investigated bending and buckling analysis of GPL reinforced plates using analytical method. A notable influence of GPL reinforcement pattern, weight fraction on the bending and buckling response is established.

Gunasekaran *et al.* (2020a) studied buckling characteristics of GPL reinforced composite plates subjected to uniform and NELs using analytical method. They reported that the buckling characteristics is influenced by the type of edge loading.

Wang *et al.* (2022a) analysed buckling characteristics of shear deformable graphene reinforced plates subjected UELs using multi-term Kantorovich-Galerkin approach. They shown that the distribution in which graphene concentration is more at the extreme surfaces gives higher buckling strength. Further, the increase in concentration of graphene leads to an increase in the buckling load.

1.2.2.4 Porous Nano-Composites

Yang *et al.* (2018) studied buckling characteristics of GPL reinforced porous plates under UEL using Chebyshev-Ritz method. The study reveals that the distribution of porosity and GPL has remarkable influence on the buckling characteristics of the plate.

Zhou *et al.* (2019) analysed non linear buckling characteristics of GPL reinforced porous cylindrical shells subjected to uniformly distributed pressure using Galerkin's method. They observed that buckling characteristics is depend on the average size of pores, GPL weight fraction and thickness of GPLs.

Shahgholian *et al.* (2020) investigated buckling characteristics of GPL reinforced porous cylindrical shells using Rayleigh-Ritz method. It is observed that increase in density and size of pores leads to a reduction in critical buckling load. On the other hand, an increase in weight fraction of GPL leads to an improvement in overall buckling capacity.

Anamagh and Bediz (2020) studied buckling and free vibration characteristics of porous GPL reinforced plates subjected to UEL using spectral Chebyshev method. From the study, it is observed that the increase in amount of porosity reduces the stiffness and thus the buckling load, while increase in amount of GPL increases the critical buckling load.

Shakir and Talha (2022) investigated dynamic response of functionally graded GPL reinforced porous spherical panels under blast loading using finite element method. The influence of GPL and porosity on the dynamic response is established in detail.

1.2.2.5 Porous Nano Composite Sandwich Material

Li *et al.* (2018) studied dynamic buckling analysis of GPL reinforced porous core sandwich plate using Galerkin's method. Based on the study, the influence of porosity, GPL content on the dynamic stability of the sandwich plate is established.

Yaghoobi and Taheri (2020) analysed buckling characteristics of sandwich plate with GPL reinforced porous core subjected to UEL using an analytical method. Based on the study, it is shown that presence of GPL improves the buckling capacity for high core to total thickness ratio than compared to smaller core to total thickness ratio.

Adhikari *et al.* (2020) studied buckling characteristics of porous FGM plates subjected to UEL and NELs using finite element method. It is shown that the critical buckling load is significantly influenced by the type of edge loading. Further, changes in buckling mode shape also observed as a function of the type of the edge load.

Tao and Dai (2021) analysed post buckling characteristics of functionally graded GPL reinforced porous cylindrical shell panels using isogeometric analysis (IGA). The study reveals that increasing GPL in the core leads to increase in post buckling strength. On the other hand, increasing porosity in the core reduces the buckling strength. Further, the distribution in which the pores are not found on the extreme surfaces enhances the buckling strength.

1.2.2.6 Carbon Nano Tube (CNT) Nano-Composites

Kiani (2017) studied buckling analysis of CNT reinforced composite plates subjected to parabolic edge loading using Chebyshev-Ritz method. The distribution of stress resultants are calculated using minimisation of membrane strain energy. Then, Ritz method is employed by considering Chebyshev polynomials to obtain the buckling parameters.

Thang *et al.* (2017) investigated non-linear buckling characteristics of CNT reinforced plates subjected to UEL by using Galerkin's method. They observed a variation in buckling characteristics with increase in CNT reinforcement. They also observed significant changes in buckling behaviour according to the graded distribution of CNTs through the thickness.

Phung-Van *et al.* (2017) analysed free vibration characteristics of CNT reinforced nano plates by considering non-local elasticity theory using isogeometric analysis. They

observed a reduction in natural frequency of the plate with increase in non local parameter.

Jiao *et al.* (2019) analysed buckling characteristics of CNT reinforced plates using differential quadrature method (DQM) subjected to different partial edge loads. Their study reveals that the buckling characteristics are sensitive to partial edge load distribution.

Chakraborty *et al.* (2019) studied buckling and post buckling characteristics of CNT reinforced cylindrical panels subjected to UEL and NELs using Galerkin's method. They observed a non-linear equilibrium post buckling path when linearly varying non-uniform edge loading is applied. However, for the parabolic and partial edge loading conditions, continuous deformation path is observed.

Thang *et al.* (2019) analysed non-linear buckling characteristics of CNT reinforced cylindrical shells subjected to UEL using Galerkin's method. They observed a significant change in buckling characteristics according to the type of CNT distribution.

Daghigh *et al.* (2020) studied buckling characteristics of CNT reinforced composite plates considering non-local elasticity theory using analytical method. They observed a decrease in the critical buckling load with increase in non-local parameter.

Naghsh *et al.* (2021) investigated buckling characteristics of polymeric core sandwich plates with CNT reinforced face-sheets subjected to uniform and different linearly varying edge loads using spline finite strip method (SFSM). They observed the influence of edge load becomes significant when the ratio between width and length is small.

1.2.2.7 Graphene Oxide Powder (GOP) Nano-Composites

Zhang *et al.* (2020) analysed buckling characteristics of graphene oxide powder (GOP) reinforced polymer beams under edge compression. Their study indicate that increase in GOP weight fraction improves critical buckling load of composite beams.

Ebrahimi *et al.* (2021) studied buckling characteristics of GOP reinforced shells using Galerkin's method. They observed that the increase in GOP weight fraction significantly improves the buckling characteristics of the shell.

1.2.3 Free Vibration Analysis

1.2.3.1 Isotropic and Laminated Composites

Mantari *et al.* (2011) proposed a higher order shear deformation theory for the free vibration analysis of composite and sandwich shells. They demonstrated the accuracy of the proposed higher order theory for the free vibration analysis of composite and sandwich shells by comparing with results of different theories.

Hosseini-Hashemi *et al.* (2015) investigated free vibration response of nano plates considering non-local elasticity theory using an analytical method. They observed a decrease in natural frequency with increase in non-local parameter.

Sayyad and Ghugal (2019) analysed the free vibration response of laminated composite and sandwich spherical shells using an analytical method. They proposed a generalised higher order shell theory and compared it with available theories to ascertain its efficiency.

Gunasekaran *et al.* (2020b) studied free vibration and acoustic characteristics of an isotropic plate subjected to different edge loads using an analytical method. They observed a reduction in free vibration frequency with the increase in magnitude of the edge loading.

Arefi (2020) investigated vibration characteristics of piezoelectric nano shells considering nonlocal elasticity theory using Galerkin's method. He observed that increase in nonlocal parameter leads to a reduction in natural frequency of the nano shell.

Moayedi *et al.* (2021) analysed free vibration characteristics of laminated cylindrical shells by considering non-local stress and strain gradient theory using generalized differential quadrature method element method (GDQEM). The influence of non-local parameter and length scale parameter on the natural frequency is analysed in detail.

1.2.3.2 Porous Cellular Materials

Chen *et al.* (2016) analysed free and forced vibration characteristics of functionally graded beams using numerical method. They observed that variation of fundamental frequency with porosity occurs according to the porosity distribution.

Akbaş (2017) investigated the thermal effects on vibration characteristics of functionally graded beams with porosity using finite element method. They observed a variation in vibration characteristics with porosity parameter and temperature according to the type of porosity distribution.

Wu *et al.* (2018) investigated free vibration characteristics of functionally graded beam structures using finite element method. They established the influence of porosity on the free vibration frequency of the porous beam.

Zhao *et al.* (2019) studied the free vibration characteristics of porous metal foam plates using improved Fourier series method (IFSM). They observed that the frequency of the porous plate depends primarily on the type of porosity distribution and amount of porosity.

Xue *et al.* (2019) analysed free vibration characteristics of porous foam plates with variation of porosity along the thickness and in-plane directions using isogeometric analysis method. The influence of different distribution of porosity and amount of porosity on the free vibration characteristics is analysed in detail.

Ramteke (2019) studied free vibration characteristics of porous plates using finite element method. He established the influence of porosity coefficient and distribution of

porosity on the free vibration response of the plate.

Wang *et al.* (2019) investigated free vibration characteristics of porous shells using Rayleigh-Ritz method. The results of the study indicate that the influence of porosity on the natural frequency of the cylindrical shell is significant. It is also shown that the influence of porosity on the natural frequency depends on different distributions.

Wang and Zhao (2019) studied free vibration characteristics of metal foam core sandwich beams using Chebyshev collocation method (CCM). From the study, the influence of different porosity distributions on the free vibration characteristics of sandwich beam is established. The influences of core to total thickness ratio and amount of porosity on the natural frequency of the sandwich beam are analysed in detail.

Li *et al.* (2019a) analysed vibration characteristics of porous cylindrical shell using Rayleigh-Ritz method. The results indicate that porosity coefficient and distributions influence the vibration frequency of the cylindrical shell.

Li *et al.* (2019b) studied free vibration characteristics of porous spherical shells using Ritz method. The study reveals that the nature of grading and amount of porosity have a significant influence on the free vibration frequency.

Teng and Wang (2020) analysed non-linear free vibration characteristics of graphene reinforced porous plates using an analytical method. From the study, it is shown that hardening or weakening phenomenon according to the increase in porosity depends upon the porosity distribution. Further, increase in weight fraction of GPL leads to an increase in non-linear natural frequency.

1.2.3.3 Graphene Nano Platelet (GPL) Nano-Composites

Feng *et al.* (2017) analysed non-linear free vibration characteristics of GPL reinforced composite beams using Ritz method. They observed significant improvement in natural frequency by the addition of GPL. The distribution pattern of GPL in which high

amount of GPL at the extreme surfaces provides the better natural frequency values.

Song *et al.* (2017) investigated free and forced vibration characteristics of GPL reinforced plates using an analytical method. They established the influence of amount of GPL and distribution on the free vibration characteristics of the plate.

Wang *et al.* (2018) studied free vibration characteristics of GPL reinforced doubly curved shells using an analytical method. They observed that the increase in small amount of GPL result in significant improvement in natural frequency.

Van Do and Lee (2020) analysed free vibration characteristics of GPL reinforced curved panels using the isogeometric analysis. They observed notable influence of GPL weight fraction and its grading pattern of reinforcement on the free vibration characteristics.

1.2.3.4 Porous Nano-Composites

Pourjabari *et al.* (2019) studied free and forced vibration characteristics of GPL reinforced porous cylindrical nano shells using an analytical method. They have used a size dependent theory to model the nano shell. Based on the study, it is shown that increase in porosity, GPL and length scale parameter leads to an increase in natural frequency.

Barati and Zenkour (2019) analysed the free vibration characteristics of GPL reinforced porous nano composite shells using Galerkin's method. The results of the study indicate that GPL, porosity distribution and porosity coefficient has an evident influence on the natural frequencies.

Wang *et al.* (2019) studied free vibration characteristics of graphene foams using Chebyshev-Ritz method. Based on the study, it is shown that increase in foam coefficient leads to reduction in natural frequency. It is also shown that foam distributions have a significant influence on the free vibration characteristics.

Rahimi *et al.* (2020) investigated free vibration characteristics of porous GPL reinforced composite cylindrical shell using semi analytical method. From the study, it is shown that the distribution of porosity and GPL has an important influence on the natural frequency.

Amir *et al.* (2022) analysed non-linear free vibration characteristics of functionally graded porous cylindrical panels finite element methods. They investigated the influence of porosity distributions on the non-linear vibration characteristics of cylindrical panels.

1.2.3.5 Carbon Nano Tube (CNT) Nano-Composites

Hedayati and Aragh (2012) analysed free vibration characteristics of CNT reinforced sectorial plates considering agglomeration using generalised DQM. Based on the study it shown that agglomeration phenomenon influences the natural frequency of the plate. Further, it is observed that agglomeration parameter has less influence for symmetric distribution compared to uniform and asymmetric distributions of CNTs.

Yas *et al.* (2013) studied free vibration characteristics of CNT reinforced cylindrical panels using DQM. The influence of CNT volume fraction and its distribution pattern on the free vibration characteristics of cylindrical panel is analysed in detail.

Tornabene *et al.* (2016) investigated vibration characteristics of CNT reinforced composite laminated doubly curved shells using generalised DQM. They demonstrated that addition of CNTs improves the stiffness of structure and thus the natural frequency. They also shown that influence of CNT is remarkable when CNTs are uniformly distributed.

Kamarian *et al.* (2016) studied free vibration characteristics of conical shells reinforced with agglomerated CNTs using generalised DQM. The effect of the agglomeration parameters on the free vibration frequency is established by the study.

Nguyen *et al.* (2018) analysed free vibration characteristics of CNT reinforced shell panels using non-uniform rational B-Spline (NURBS) functions. They observed improvement in natural frequency of the shell panel with increase in volume fraction. It is also observed that the improvement in frequency with volume fraction is highly dependent on the distribution pattern of CNTs.

Ansari *et al.* (2019) investigated free vibration characteristics of CNT reinforced plates with arbitrary shapes using DQM. The results presented shows that the natural frequency increases with increase in volume fraction of CNT. The results also revealed that the nature of CNT distribution pattern has a significant influence on the natural frequency.

Dindarloo and Li (2019) studied free vibration characteristics of CNT reinforced cylindrical shell panels by considering non-local elasticity theory an using analytical method. They observed that the increase in non-local parameter decreases the natural frequency of the cylindrical panel.

Ghasemi *et al.* (2019) analysed vibration characteristics of CNT reinforced cylindrical shells considering the agglomeration effect using an analytical method. They demonstrated that an agglomeration parameter has significant influence on the free vibration frequency. Further, it is also shown that increase in mass fraction of CNTs leads to an increase in natural frequency of the shell.

Daghigh and Daghigh (2019) investigated free vibration behaviour of CNT reinforced plates considering non-local elasticity theory and analytical methods. The influences of non-local parameter, volume fraction of CNT on the free vibration characteristics are analysed in detail.

Bisheh and Civalek (2020) studied vibration characteristics of CNT reinforced cylindrical panels subjected to hygrothermal loading using an analytical method. They reported that increasing the amount of CNT as reinforcement improves the natural frequencies of the cylindrical panel. They also observed that an increase in temperature or

moisture reduces the natural frequency of the cylindrical panel.

Civalek *et al.* (2022) analysed buckling and free vibration characteristics of CNT reinforced laminated composite plates subjected to UEL using discrete singular convolution method. The study reveals that lower aspect ratio of the plate and increase in volume fraction of CNT leads to increase in buckling and free vibration characteristics.

Cheshmeh *et al.* (2022) studied buckling and free vibration characteristics of CNT reinforced plate using analytical method and the DQM. From the study, it is inferred that the increase in CNT volume fraction increases the natural frequency. Further, the influence of CNT distribution pattern on the buckling and free vibration characteristics is also presented.

1.2.3.6 Graphene Oxide Powder (GOP) Nano-Composites

Ebrahimi *et al.* (2019) studied free vibration characteristics of GOP reinforced composite beams using Galerkin's method. They observed that increase in GOP weight fraction increases the natural frequency of the composite beam. They also established the influence of GOP weight fraction on the free vibration characteristics.

Ebrahimi *et al.* (2020) analysed free vibration characteristics of GOP reinforced plates subjected to thermal loads using an analytical method. They observed that the variation in free vibration frequency with increase in GOP weight fraction is different for room temperature and elevated temperature cases. However, for some distributions the vibration frequency is observed to be increasing with the temperature.

Wang *et al.* (2020) investigated the free vibration characteristics of GOP reinforced beams using Ritz method. They observed that the addition of small amounts of GOP improves the natural frequency. They also suggested that by placing more amount of GOPs on top and bottom fibres, higher stiffness and thereby higher natural frequency is observed.

Wang *et al.* (2022b) studied vibration characteristics of GOP reinforced curved beams using an analytical method. The study reveals that a low level of reinforcement leads to much high improvement in vibration frequency of the curved beams. Further, GOP reinforcements and diameter to thickness ratio has a high influence on the vibration frequency.

1.2.4 Closure

Many researchers have studied buckling and free vibration characteristics of structures subjected to UEL over the years. However, very limited amount of studies are carried out by considering non-uniformly varying edge loads. From the literature survey, it is found that the type of edge loading, aspect ratio of the cylindrical panel, distribution of material properties through the thickness significantly influence the buckling and free vibration characteristics of the cylindrical panel.

Most of the studies of structures subjected to NELs are carried out using numerical methods such as finite element method, differential quadrature method and isogeometric method etc. The semi-analytical method is used in limited amount of studies and it has an ease of computation for finding the buckling and free vibration when subjected to non-uniform edge loads more accurately.

The development of nano composite structures which are light in weight helps in reduction of emissions and fuel savings. Introducing nano reinforcements enhances structural stiffness of the thin-walled structures significantly without much increase in overall weight. The weight of the component can be reduced by introducing the porosity. However, the porosity tends to reduce the stiffness of the structure. In that case further improvement in stiffness can be achieved by using nano reinforcements. For light weight cylindrical panel structures, the literature review reveals that the distribution and amount of porosity, distribution and amount of nano reinforcements, non-local effect and agglomeration phenomenon significantly influences the buckling and free

vibration characteristics.

1.3 Objectives and Scope of Study

Because of the rapid development of light weight nano-composite cylindrical panels, it is important to study the buckling and free vibration characteristics for better understanding and design of these structures. From the literature survey, it is evident that the nature of edge loading significantly influences the buckling and free vibration characteristics. The main objective is to investigate the influence of non-uniform edge loads (NELs) on the buckling and free vibration characteristics of cylindrical panels.

Similarly, the usage of nano composites with porosity and nano reinforcements requires careful analysis of weight fraction and distribution of nano reinforcements, amount and distribution of porosity in cylindrical panel and sandwich cylindrical panel. Furthermore, the influence of porosity pattern, amount of porosity on the core to total thickness ratio also need to be analysed. Further, the possible issues associated with the nano reinforcements such as agglomeration and consideration of size effects also need be analysed. The following objectives are formulated based on the above discussion:

- To implement a semi-analytical method for buckling and free vibration behaviour of cylindrical panels subjected to different types of NELs.
- To study the buckling and dynamic behaviour of GPL reinforced porous cylindrical nano-composite panels and sandwich panels subjected to different NELs.
- To investigate buckling and free vibration behaviour of CNT reinforced cylindrical panels under NELs considering the agglomeration of CNTs and based on the non-local elasticity theory.
- To analyze the buckling and free vibration response of graphene oxide powder (GOP) reinforced cylindrical panel under NELs.

1.4 Outline of the Thesis

The first chapter of the thesis includes the brief introduction and literature review. In the following chapters, the methodology, validation and followed by results and discussion are presented. In the final chapter, conclusions and outcomes of the present research work is presented. The remaining chapters details are explained in the sections following.

Chapter 2 details the methodology followed for buckling and free vibration of a cylindrical panel under NELs. The generalised formulation of governing differential equations is discussed first. Followed by that semi analytical solution procedure including pre-buckling analysis is discussed in detail. The solutions obtained are validated with different published results.

Chapter 3 details the buckling and free vibration characteristics of an GPL reinforced porous cylindrical panel under NELs. The semi analytical method is used to carry out the analysis of the influence of amount and distribution of porosity, amount and distribution of GPL, aspect ratio and type of edge loading on the buckling and free vibration characteristics.

Chapter 4 examines buckling and free vibration response of a sandwich cylindrical panel having GPL reinforced foam core and aluminium face sheets subjected to uniform and different NELs. The influence of amount and distribution of porosity, amount and distribution of GPL, core to total thickness ratio, aspect ratio and type of edge loading on the buckling and free vibration behaviour of sandwich cylindrical panel is presented in detail.

Chapter 5 details the non-local buckling and free vibration studies of agglomerated CNT reinforced cylindrical panel subjected to NELs. The CNT reinforced cylindrical panel is analysed for the influence of non local parameter, type of edge loading, degree of agglomeration on the buckling and free vibration response.

Chapter 6 presents the investigation of buckling and free vibration response of graphene oxide powder (GOP) reinforced cylindrical panel structures under the influence of NELs. The influence of amount and distribution of GOP, type of edge loading, aspect ratio on the buckling and free vibration characteristics is analysed in detail.

In chapter 7, important findings and conclusions are summarized.

CHAPTER 2

METHODOLOGY

2.1 Introduction

From the previous chapter, the literature review, motivation and scope for the study is established. In this chapter, methodology followed for buckling and free vibration analysis of cylindrical panels subjected to different types of non-uniform edge loads (NELs) is described. A semi analytical method based on Galerkin's technique is implemented which has the ability to predict the buckling and free vibration characteristics of the panel under the influence of NELs accurately with the help of a higher order shear deformation theory. Two sets of non-uniform edge loads namely, non-uniform load I (NEL-I) and non-uniform load II (NEL-II) are considered in the present work. In the case of non-uniform load I, the variation of edge load is linear while in non-uniform load II case the variation of edge load is not linear.

2.2 Analysis Approach

Semi-analytical method is used to find the buckling and free vibration characteristics of the cylindrical panel under the influence of NELs. Three different types of edge loadings namely, uniform, type I non-uniform edge loadings, type II non uniform edge loadings are considered. The analysis approach followed in the present work is given in Figure 2.1. The stress distribution developed due to UEL and NEL-I coincides with edge loading pattern so the panel does not experience any pre-stress in directions other than that of loading. Hence, the pre-buckling stress evaluation is not carried out when the panel is subjected to these loadings. On the other hand, the stress distribution developed

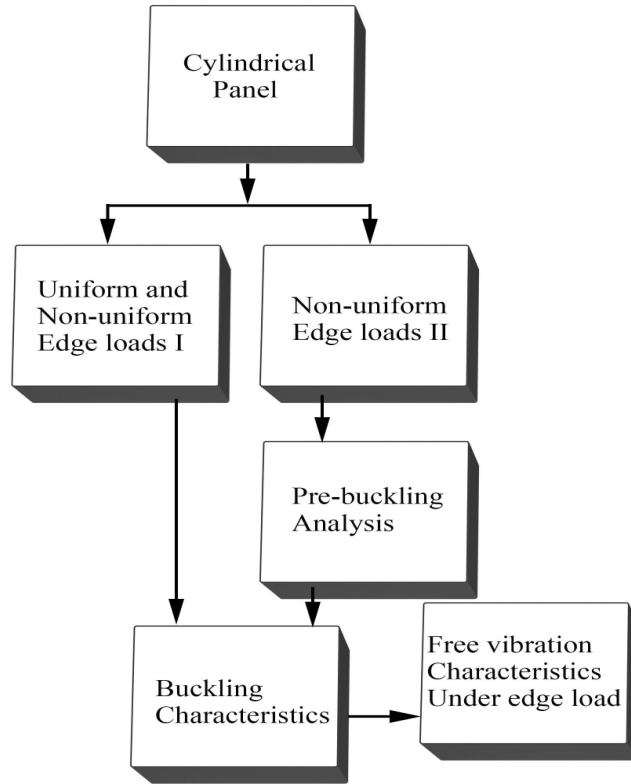


Figure 2.1: Flow chart of the present work

due to NEL-II is calculated using pre buckling analysis because of the presence of all in plane stress components. After the evaluation of stress distribution developed as a results of edge loads, buckling characteristics are obtained by solving the eigen value buckling problem. Similarly, free vibration characteristics are estimated by solving free vibration eigen value problem.

2.3 Formulation

The derivation of governing differential equations of the cylindrical panel under various NELs is described in this section. Schematic of the cylindrical panel considered, with details of geometric configuration and coordinate system used is shown in Figure 2.2.

The displacement field considering a higher order shear deformation theory is:

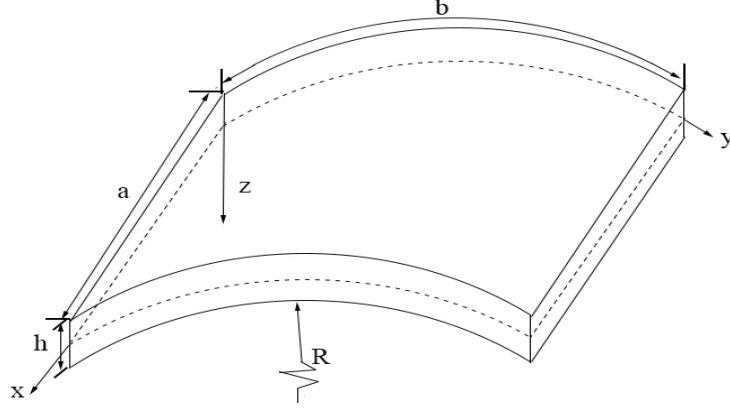


Figure 2.2: Geometry and coordinate system of the cylindrical panel studied.

$$\begin{Bmatrix} u(x, y, z, t) \\ v(x, y, z, t) \\ w(x, y, z, t) \end{Bmatrix} = \begin{Bmatrix} u_0(x, y, t) \\ (1 + \frac{z}{R})v_0(x, y, t) \\ w_0(x, y, t) \end{Bmatrix} - z \begin{Bmatrix} \frac{\partial w_0(x, y, t)}{\partial x} \\ \frac{\partial w_0(x, y, t)}{\partial y} \\ 0 \end{Bmatrix} + \Gamma(z) \begin{Bmatrix} \psi_x(x, y, t) \\ \psi_y(x, y, t) \\ 0 \end{Bmatrix} \quad (2.1)$$

where, $\Gamma(z) = z - \frac{4}{3} \frac{z^3}{h^2}$ is the Reddy's shear deformation theorem (Reddy 2000) and $\psi_x(x, y, t)$, $\psi_y(x, y, t)$ are rotations of the cross-section about y and x axis respectively. u_0, v_0 and w_0 denotes the displacement of the mid plane along x, y, z directions respectively, and u, v, w are the displacements of point of interest within the cylindrical panel. The relations connecting in plane, transverse strains and displacement is outlined as:

$$\begin{Bmatrix} \epsilon_{xx} \\ \epsilon_{yy} \\ \gamma_{xy} \end{Bmatrix} = \begin{Bmatrix} \frac{\partial u_0}{\partial x} \\ \frac{\partial v_0}{\partial y} + \frac{w_0}{R} \\ \frac{\partial u_0}{\partial y} + \frac{\partial v_0}{\partial x} \end{Bmatrix} - z \begin{Bmatrix} \frac{\partial^2 w_0}{\partial x^2} \\ \frac{\partial^2 w_0}{\partial y^2} + \frac{1}{R} \frac{\partial v_0}{\partial y} \\ \frac{1}{R} \frac{\partial v_0}{\partial x} - 2 \frac{\partial^2 w_0}{\partial x \partial y} \end{Bmatrix} + \Gamma(z) \begin{Bmatrix} \frac{\partial \psi_x}{\partial x} \\ \frac{\partial \psi_y}{\partial y} \\ \frac{\partial \psi_x}{\partial y} + \frac{\partial \psi_y}{\partial x} \end{Bmatrix} + \epsilon^{nl} \quad (2.2a)$$

$$\begin{Bmatrix} \gamma_{xz} \\ \gamma_{yz} \end{Bmatrix} = \frac{\partial \Gamma(z)}{\partial z} \begin{Bmatrix} \psi_x \\ \psi_y \end{Bmatrix} \quad (2.2b)$$

where, ϵ^{nl} denotes the non-linear strain components given as

$$\epsilon^{nl} = \left\{ \frac{1}{2} \left(\frac{\partial w_0}{\partial x} \right)^2 \quad \frac{1}{2} \left(\frac{\partial w_0}{\partial y} \right)^2 \quad \left(\frac{\partial w_0}{\partial x} \frac{\partial w_0}{\partial y} \right) \right\}^T \quad (2.3)$$

The stress-strain relation of the cylindrical panel is established considering a layered structure as follows:

$$\begin{Bmatrix} \sigma_{xx} \\ \sigma_{yy} \\ \tau_{yz} \\ \tau_{xz} \\ \tau_{xy} \end{Bmatrix}^{(k)} = \begin{bmatrix} Q_{11} & Q_{12} & 0 & 0 & 0 \\ Q_{12} & Q_{22} & 0 & 0 & 0 \\ 0 & 0 & Q_{44} & 0 & 0 \\ 0 & 0 & 0 & Q_{55} & 0 \\ 0 & 0 & 0 & 0 & Q_{66} \end{bmatrix}^{(k)} \begin{Bmatrix} \epsilon_{xx} \\ \epsilon_{yy} \\ \gamma_{yz} \\ \gamma_{xz} \\ \gamma_{xy} \end{Bmatrix}^{(k)} \quad (2.4)$$

Q_{ij} are stiffness matrix coefficients and defined as follows:

$$\begin{aligned} Q_{11} &= Q_{22} = \frac{E(z)}{1-\nu^2} \\ Q_{66} &= Q_{55} = Q_{44} = G(z) \\ Q_{12} &= Q_{21} = \nu' \frac{E(z)}{1-\nu^2} \end{aligned} \quad (2.5)$$

Hamilton's principle is applied to obtain the governing differential equations of the cylindrical panel

$$\int_{t_1}^{t_2} (\delta K + \delta U - \delta V) dt = 0 \quad (2.6)$$

where, δ - variational operator, δV - work done by the external forces, δU - strain energy, and δK - kinetic energy.

$$\begin{aligned} & \int_{t_1}^{t_2} \left\{ \rho \int_{-h/2}^{h/2} \int_0^b \int_0^a \left(\frac{\partial^2 u}{\partial t^2} \delta u + \frac{\partial^2 v}{\partial t^2} \delta v + \frac{\partial^2 w}{\partial t^2} \delta w \right) dx dy dz \right. \\ & \left. + \int_{-h/2}^{h/2} \int_0^b \int_0^a (\sigma_{xx} \delta \epsilon_{xx} + \sigma_{yy} \delta \epsilon_{yy} + \tau_{xy} \delta \gamma_{xy} + \tau_{xz} \delta \gamma_{xz} + \tau_{yz} \delta \gamma_{yz}) dx dy dz \right\} = 0 \end{aligned} \quad (2.7)$$

The in-plane force and moment resultants of the cylindrical panel are defined as:

$$\left\{ \left\{ \begin{matrix} N_{xx} \\ N_{yy} \\ N_{xy} \end{matrix} \right\}, \left\{ \begin{matrix} M_{xx}^b \\ M_{yy}^b \\ M_{xy}^b \end{matrix} \right\}, \left\{ \begin{matrix} M_{xx}^s \\ M_{yy}^s \\ M_{xy}^s \end{matrix} \right\} \right\} = \int_{-\frac{h}{2}}^{\frac{h}{2}} \left(1, z, z - \frac{4}{3} \frac{z^3}{h^2} \right) \left\{ \begin{matrix} \sigma_{xx} \\ \sigma_{yy} \\ \tau_{xy} \end{matrix} \right\} dz \quad (2.8)$$

$$\left\{ \begin{matrix} Q_{xz} \\ Q_{yz} \end{matrix} \right\} = \int_{-\frac{h}{2}}^{\frac{h}{2}} \left(1 - 4 \frac{z^2}{h^2} \right) \left\{ \begin{matrix} \tau_{xz} \\ \tau_{yz} \end{matrix} \right\} dz \quad (2.9)$$

Inertia coefficients of the cylindrical panel are defined as:

$$\begin{aligned} (I_1, I_2, I_3) &= \int_{-\frac{h}{2}}^{\frac{h}{2}} \rho (1, z, z^2) dz \\ (I_4, I_5, I_6) &= \int_{-\frac{h}{2}}^{\frac{h}{2}} \rho \left(z - \frac{4}{3} \frac{z^3}{h^2}, z \left(z - \frac{4}{3} \frac{z^3}{h^2} \right), \left(z - \frac{4}{3} \frac{z^3}{h^2} \right)^2 \right) dz \end{aligned} \quad (2.10)$$

Introducing stress resultants and inertia coefficients in Equation 2.7, takes the following form:

$$\begin{aligned} 0 &= \int_{t_1}^{t_2} \left\{ \int_0^b \int_0^a \left[\tilde{N}_{xx} \frac{\partial \delta u_0}{\partial x} - M_{xx}^b \frac{\partial^2 \delta w_0}{\partial x^2} + M_{xx}^s \frac{\partial \delta \psi_x}{\partial x} + \tilde{N}_{xx} \frac{\partial w_0}{\partial x} \frac{\partial \delta w_0}{\partial x} + \tilde{N}_{yy} \frac{\partial \delta v_0}{\partial y} + \frac{\tilde{N}_{xx}}{R} \delta w_0 \right. \right. \\ &\quad - M_{yy}^b \frac{\partial^2 \delta w_0}{\partial y^2} + \frac{M_{yy}^b}{R} \frac{\partial \delta v_0}{\partial y} + M_{yy}^s \frac{\partial \delta \psi_y}{\partial y} + \tilde{N}_{yy} \frac{\partial w_0}{\partial y} \frac{\partial \delta w_0}{\partial y} + \tilde{N}_{xy} \frac{\partial \delta u_0}{\partial y} + \tilde{N}_{xy} \frac{\partial \delta v_0}{\partial x} - 2M_{xy}^b \frac{\partial^2 \delta w_0}{\partial x \partial y} \\ &\quad + \frac{M_{xy}^b}{R} \frac{\partial \delta v_0}{\partial x} + M_{xy}^s \frac{\partial \delta \psi_x}{\partial y} + M_{xy}^s \frac{\partial \delta \psi_y}{\partial x} + \tilde{N}_{xy} \frac{\partial w_0}{\partial y} \frac{\partial \delta w_0}{\partial x} + \tilde{N}_{xy} \frac{\partial w_0}{\partial x} \frac{\partial \delta w_0}{\partial y} + Q_{xz} \delta \psi_x + Q_{yz} \delta \psi_y \\ &\quad - \left((I_1 \frac{\partial^2 u_0}{\partial t^2} - I_2 \frac{\partial^3 w_0}{\partial x \partial t^2} + I_4 \frac{\partial^2 \psi_x}{\partial t^2}) \delta u_0 + (I_2 \frac{\partial^3 u_0}{\partial x \partial t^2} - I_3 \frac{\partial^4 w_0}{\partial x^4 \partial t^2} + I_5 \frac{\partial^3 \psi_x}{\partial x \partial t^2} + I_2 \frac{\partial^3 v_0}{\partial y \partial t^2} - I_3 \frac{\partial^4 w_0}{\partial y^2 \partial t^2} \right. \\ &\quad + \frac{I_3}{R} \frac{\partial^3 v_0}{\partial y \partial t^2} + I_5 \frac{\partial^3 \psi_y}{\partial y \partial t^2} + I_1 \frac{\partial^2 w_0}{\partial t^2}) \delta w_0 + ((I_1 + \frac{I_2}{R} + \frac{I_3}{R^2}) \frac{\partial^2 v_0}{\partial t^2} - (I_2 + \frac{I_3}{R}) \frac{\partial^3 w_0}{\partial y \partial t^2} + (I_4 + \frac{I_5}{R}) \frac{\partial^2 \psi_y}{\partial t^2}) \delta v_0 \\ &\quad \left. + (I_4 \frac{\partial^2 u_0}{\partial t^2} - I_5 \frac{\partial^3 w_0}{\partial x \partial t^2}) + I_6 \frac{\partial^2 \psi_x}{\partial t^2} \right) \delta \psi_x + ((I_4 + \frac{I_5}{R}) \frac{\partial^2 v_0}{\partial t^2} - I_5 \frac{\partial^3 w_0}{\partial y \partial t^2} + I_6 \frac{\partial^2 \psi_y}{\partial t^2}) \delta \psi_y \Big] dx dy \Big\} dt \end{aligned} \quad (2.11)$$

The governing partial differential equations can be written by equating δu_0 , δv_0 , δw_0 , $\delta\phi$, $\delta\psi$ coefficients to zero given as:

$$\begin{aligned}
\frac{\partial \tilde{N}_{xy}}{\partial y} + \frac{\partial \tilde{N}_{xx}}{\partial x} &= I_1 \frac{\partial^2 u_0}{\partial t^2} - I_2 \frac{\partial^3 w_0}{\partial x \partial t^2} + I_4 \frac{\partial^2 \psi_x}{\partial t^2} & : & \delta u_0 \\
\frac{\partial \tilde{N}_{xy}}{\partial x} + \frac{\partial \tilde{N}_{yy}}{\partial y} + \frac{1}{R} \left(\frac{\partial M_{yy}^b}{\partial y} + \frac{\partial M_{xy}^b}{\partial x} \right) &= \left(I_1 + 2\frac{I_2}{R} + \frac{I_3}{R^2} \right) \frac{\partial^2 v_0}{\partial t^2} - \left(I_2 + \frac{I_3}{R} \right) \frac{\partial^3 w_0}{\partial y \partial t^2} \\
+ \left(I_4 + \frac{I_5}{R} \right) \frac{\partial^2 \psi_y}{\partial t^2} & & : & \delta v_0 \\
\frac{\partial^2 M_{xx}^b}{\partial x^2} + 2 \frac{\partial^2 M_{xy}^b}{\partial x \partial y} + \frac{\partial^2 M_{yy}^b}{\partial y^2} - \frac{\tilde{N}_{yy}}{R} + \frac{\partial}{\partial x} \left(\frac{\partial w}{\partial x} \tilde{N}_{xx} + \frac{\partial w}{\partial y} \tilde{N}_{xy} \right) \\
+ \frac{\partial}{\partial y} \left(\frac{\partial w}{\partial y} \tilde{N}_{yy} + \frac{\partial w}{\partial x} \tilde{N}_{xy} \right) + q &= I_2 \frac{\partial^3 u_0}{\partial x \partial t^2} - I_3 \frac{\partial^4 w_0}{\partial x^2 \partial t^2} + I_5 \frac{\partial^3 \psi_x}{\partial x \partial t^2} + \left(I_2 + \frac{I_3}{R} \right) \frac{\partial^3 v_0}{\partial y \partial t^2} \\
- I_3 \frac{\partial^4 w_0}{\partial y^2 \partial t^2} + I_5 \frac{\partial^3 \psi_y}{\partial y \partial t^2} + I_1 \frac{\partial^2 w_0}{\partial t^2} & & : & \delta w_0 \\
\frac{\partial M_{xx}^s}{\partial x} + \frac{\partial M_{xy}^s}{\partial y} - Q_{xx} &= I_4 \frac{\partial^2 u_0}{\partial t^2} - I_5 \frac{\partial^3 w_0}{\partial x \partial t^2} + I_6 \frac{\partial^2 \psi_x}{\partial t^2} & : & \delta \psi_x \\
\frac{\partial M_{yy}^s}{\partial y} + \frac{\partial M_{xy}^s}{\partial x} - Q_{yy} &= \left(I_4 + \frac{I_5}{R} \right) \frac{\partial^2 v_0}{\partial t^2} - I_5 \frac{\partial^3 w_0}{\partial y \partial t^2} + I_6 \frac{\partial^2 \psi_y}{\partial t^2} & : & \delta \psi_y
\end{aligned} \tag{2.12}$$

and,

$$\begin{Bmatrix} \tilde{N}_{xx} \\ \tilde{N}_{xy} \\ \tilde{N}_{yy} \end{Bmatrix} = \begin{Bmatrix} N_{xx} - n_{xx} \\ N_{xy} - n_{xy} \\ N_{yy} - n_{yy} \end{Bmatrix} \tag{2.13}$$

Using Equations 2.4, 2.8 and 2.12 and neglecting non-linear terms the governing differential equations can be re-written as:

$$\begin{aligned}
A_{11} \frac{\partial^2 u_0}{\partial x^2} - B_{11} \frac{\partial^3 w_0}{\partial x^3} + E_{11} \frac{\partial^2 \psi_x}{\partial x^2} + A_{12} \frac{\partial^2 v_0}{\partial xy} + \frac{A_{12}}{R} \frac{\partial w_0}{\partial x} - B_{12} \frac{\partial^3 w_0}{\partial xy^2} + E_{12} \frac{\partial^2 \psi_y}{\partial xy} + A_{66} \frac{\partial^2 u_0}{\partial y^2} \\
+ A_{66} \frac{\partial^2 v_0}{\partial xy} - 2B_{66} \frac{\partial^3 w_0}{\partial xy^2} + E_{66} \frac{\partial^2 \psi_x}{\partial x^2} + E_{66} \frac{\partial^2 \psi_y}{\partial xy} = I_1 \frac{\partial^2 u_0}{\partial t^2} - I_2 \frac{\partial^3 w_0}{\partial xt^2} + I_4 \frac{\partial^2 \psi_x}{\partial t^2}
\end{aligned} \tag{2.14a}$$

$$\begin{aligned}
& A_{12} \frac{\partial^2 u_0}{\partial xy} - B_{12} \frac{\partial^2 w_0}{\partial yx^2} + E_{12} \frac{\partial^2 \psi_x}{\partial xy} + A_{22} \frac{\partial^2 v_0}{\partial y^2} + \frac{A_{22}}{R} \frac{\partial w_0}{\partial y} - B_{22} \frac{\partial^2 w_0}{\partial y^3} + E_{22} \frac{\partial^2 \psi_y}{\partial y^2} + A_{66} \frac{\partial^2 u_0}{\partial xy} \\
& + A_{66} \frac{\partial^2 v_0}{\partial x^2} - 2B_{66} \frac{\partial^2 w_0}{\partial yx^2} + E_{66} \frac{\partial^2 \psi_x}{\partial xy} + E_{66} \frac{\partial^2 \psi_y}{\partial x^2} = \left(I_1 + 2\frac{I_2}{R} + \frac{I_3}{R^2} \right) \frac{\partial^2 v_0}{\partial t^2} - \left(I_2 + \frac{I_3}{R} \right) \frac{\partial^2 w_0}{\partial yt^2} \\
& + \left(I_4 + \frac{I_5}{R} \right) \frac{\partial^2 \psi_y}{\partial t^2}
\end{aligned} \tag{2.14b}$$

$$\begin{aligned}
& B_{11} \frac{\partial^3 u_0}{\partial x^3} - D_{11} \frac{\partial^4 w_0}{\partial x^4} + 2B_{66} \frac{\partial^3 u_0}{\partial xy^2} + B_{12} \frac{\partial^3 u_0}{\partial xy^2} - \frac{A_{12}}{R} \frac{\partial u_0}{\partial x} + B_{12} \frac{\partial^3 v_0}{\partial yx^2} - 2D_{12} \frac{\partial^4 w_0}{\partial x^2 y^2} + 2B_{66} \frac{\partial^3 v_0}{\partial yx^2} \\
& + B_{22} \frac{\partial^3 v_0}{\partial y^3} - \frac{A_{22}}{R} \frac{\partial v_0}{\partial y} + \frac{2B_{12}}{R} \frac{\partial^2 w_0}{\partial x^2} - 4D_{66} \frac{\partial^4 w_0}{\partial x^2 y^2} + \frac{2B_{22}}{R} \frac{\partial^2 w_0}{\partial y^2} - \frac{A_{22}}{R^2} w_0 - D_{22} \frac{\partial^4 w_0}{\partial y^4} + F_{11} \frac{\partial^3 \psi_x}{\partial x^3} \\
& + 2F_{66} \frac{\partial^3 \psi_x}{\partial xy^2} + F_{12} \frac{\partial^3 \psi_x}{\partial xy^2} - \frac{E_{12}}{R} \frac{\partial \psi_x}{\partial x} + F_{12} \frac{\partial^3 \psi_y}{\partial yx^2} + 2F_{66} \frac{\partial^3 \psi_y}{\partial yx^2} + F_{22} \frac{\partial^3 \psi_x}{\partial y^3} - \frac{E_{22}}{R} \frac{\partial \psi_y}{\partial y} + \aleph(w_0) \\
& = I_2 \frac{\partial^3 u_0}{\partial xt^2} + I_3 \frac{\partial^4 w_0}{\partial x^2 t^2} + I_5 \frac{\partial^3 \psi_x}{\partial xt^2} + \left(I_2 + \frac{I_3}{R} \right) \frac{\partial^3 v_0}{\partial yt^2} - I_3 \frac{\partial^4 w_0}{\partial y^2 t^2} + I_5 \frac{\partial^3 \psi_y}{\partial yt^2} + I_1 \frac{\partial^2 w_0}{\partial t^2}
\end{aligned} \tag{2.14c}$$

$$\begin{aligned}
& E_{11} \frac{\partial^2 u_0}{\partial x^2} + E_{66} \frac{\partial^2 u_0}{\partial y^2} + E_{12} \frac{\partial^2 v_0}{\partial xy} + E_{66} \frac{\partial^2 v_0}{\partial xy} - F_{11} \frac{\partial^3 w_0}{\partial x^3} + \frac{E_{12}}{R} \frac{\partial w_0}{\partial x} - F_{12} \frac{\partial^3 w_0}{\partial xy^2} - 2F_{66} \frac{\partial^3 w_0}{\partial xy^2} \\
& + H_{11} \frac{\partial^2 \psi_x}{\partial x^2} + H_{66} \frac{\partial^2 \psi_x}{\partial x^2} + H_{12} \frac{\partial^2 \psi_y}{\partial xy} + H_{66} \frac{\partial^2 \psi_y}{\partial xy} - L_{55} \psi_x = I_4 \frac{\partial^2 u_0}{\partial t^2} - I_5 \frac{\partial^3 w_0}{\partial xt^2} + I_6 \frac{\partial^2 \psi_x}{\partial t^2}
\end{aligned} \tag{2.14d}$$

$$\begin{aligned}
& E_{12} \frac{\partial^2 u_0}{\partial xy} + E_{66} \frac{\partial^2 u_0}{\partial xy} + E_{22} \frac{\partial^2 v_0}{\partial y^2} + E_{66} \frac{\partial^2 v_0}{\partial x^2} - F_{22} \frac{\partial^3 w_0}{\partial y^3} + \frac{E_{22}}{R} \frac{\partial w_0}{\partial y} - F_{12} \frac{\partial^3 w_0}{\partial yx^2} - 2F_{66} \frac{\partial^3 w_0}{\partial yx^2} \\
& + H_{12} \frac{\partial^2 \psi_x}{\partial xy} + H_{66} \frac{\partial^2 \psi_x}{\partial xy} + H_{22} \psi_{,yy} \frac{\partial^2 \psi_y}{\partial y^2} + H_{66} \frac{\partial^2 \psi_y}{\partial x^2} - L_{44} \psi_{,y} \frac{\partial \psi_y}{\partial y} = \left(I_4 + \frac{I_5}{R} \right) \frac{\partial^2 v_0}{\partial t^2} \\
& - I_5 \frac{\partial^3 w_0}{\partial yt^2} + I_6 \frac{\partial^2 \psi_y}{\partial t^2}
\end{aligned} \tag{2.14e}$$

The different coefficients are defined as follows:

$$\begin{aligned}
& (A_{ij}, B_{ij}, D_{ij}, E_{ij}) = \int_{-\frac{h}{2}}^{\frac{h}{2}} Q_{ij}(1, z, z^2, z - \frac{4}{3} \frac{z^3}{h^2}) dz \\
& (F_{ij}, H_{ij}, L_{ij}) = \int_{-\frac{h}{2}}^{\frac{h}{2}} Q_{ij} \left(z(z - \frac{4}{3} \frac{z^3}{h^2}), \left(z - \frac{4}{3} \frac{z^3}{h^2} \right)^2, \left(1 - 4 \frac{z^2}{h^2} \right)^2 \right) dz
\end{aligned} \tag{2.15}$$

The governing differential equations and different coefficients presented in this section provides a general frame work of the buckling and free vibration studies conducted throughout the study. However, in subsequent chapters changes relevant to the particular study are presented. The properties of materials used in the thesis is summarised in

Table 2.1: Different materials and properties used in the present study

SI No	Matrix	Reinforcement
1	Copper $E_m = 130\text{GPa}, \nu_m = 0.34$ $\rho_m = 8960\text{kg/m}^3$	GPL $E_{GPL} = 1.01\text{TPa}, \nu_{GPL} = 0.186$ $\rho_{GPL} = 1062.5 \frac{\text{kg}}{\text{m}^3}$
2	Aluminium Alloy $E_m = 68.3\text{GPa}, \nu_m = 0.34$ $\rho_m = 2689.8 \frac{\text{kg}}{\text{m}^3}$	GPL $E_{GPL} = 1.01\text{TPa}, \nu_{GPL} = 0.186$ $\rho_{GPL} = 1062.5 \frac{\text{kg}}{\text{m}^3}$
3	PmPV $E_m = 2.1\text{GPa}, \nu_m = 0.34$ $\rho_m = 1150 \frac{\text{kg}}{\text{m}^3}$	SWCNT Hills moduli(GPa): $p_r=1, l_r=10, k_r=30, m_r=1, n_r=450$ $\rho_{GPL} = 1400 \frac{\text{kg}}{\text{m}^3}, \nu_{GPL} = 0.186$
4	Epoxy $E_m = 3.0\text{GPa}, \nu_m = 0.34$ $\rho_m = 1200 \frac{\text{kg}}{\text{m}^3}$	GOP $E_{GOP} = 444.8\text{GPa}, \nu_{GOP} = 0.165$ $\rho_{GOP} = 1090 \frac{\text{kg}}{\text{m}^3}$

Table 2.1.

2.4 Solution Procedure

In the present work, buckling and free vibration studies are carried out in different steps. Firstly, pre-buckling analysis is performed to obtain the stress distribution due to applied non-uniform edge load (NEL). After evaluating all the in-plane stress resultants, the buckling parameters (critical buckling load and its mode shape) are obtained by solving the linear eigen value problem. Later, free vibration parameters (natural frequencies and the corresponding mode shapes) under the influence of NELs are obtained by solving the associated eigen value problem. The free vibration of the panel is performed as a function of the buckling load, i.e., by varying the magnitude of the edge load from zero to the buckling load. The semi-analytical method used in the present work is adopted from the literature because of its simplicity and ease of application with sufficient accuracy. However, there is no solution available in the open literature for the analysis of different nano filler reinforced and sandwich cylindrical panels subjected to different types of non-uniform and partial edge loads using the semi-analytical method. The computational challenge is that when analysing loads such as partial edge

loads, which is a discontinuous edge load the load need to be converted to continuous form using Fourier series approximation. Detailed procedure of all the steps are given in sections follows. Various types of edge loads considered in the present work are presented in Figure 2.3. They are defined as follows:

1. Uniform edge load (UEL)

$$N_x = N_0 \quad (2.16)$$

2. Non-uniform edge Load-I (NEL-I)

$$N_x = N_0 \left[1 - \eta \left(\frac{y}{b} \right) \right] \quad (2.17)$$

- (a) $\eta = 0.5$; Trapezoidal loading
- (b) $\eta = 1$; Triangular loading
- (c) $\eta = 1.5$; Partial tension loading

3. Non-uniform edge Load-II (NEL-II)

- (a) Parabolic loading

$$N_x = 4N_0 \frac{y}{b} \left[1 - \left(\frac{y}{b} \right) \right] \quad (2.18)$$

- (b) Reverse sinusoidal loading

$$N_x = N_0 \left(\frac{2}{3} \right) \left(\frac{\pi}{\pi-2} \right) \left(1 - \sin \frac{\pi y}{b} \right) \quad (2.19)$$

- (c) Increasing parabolic loading

$$N_x = N_0 \frac{2y^2}{b^2} \quad (2.20)$$

- (d) Partial edge loading

$$N_x = N_0 \left(\frac{2(d_2-d_1)}{b} + \sum_{n=1}^{\infty} \frac{2}{n\pi} \left(\sin \frac{2\pi n d_2}{b} - \sin \frac{2\pi n d_1}{b} \right) \cos \frac{2\pi n y}{b} \right) \quad (2.21)$$

Where d_1 and d_2 are distances from the origin for partial edge loading as presented in 2.3.

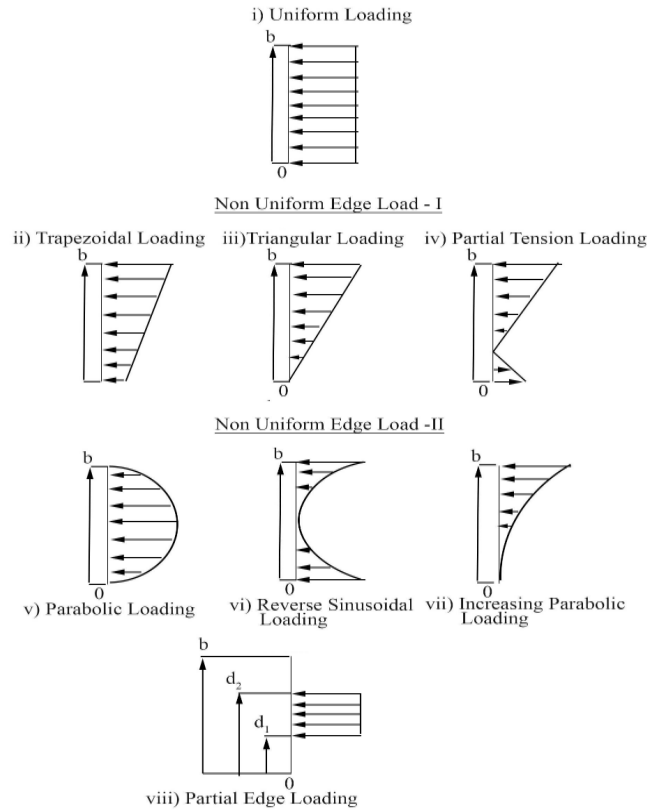


Figure 2.3: Different types of loadings considered

2.4.1 Pre-Buckling Analysis

The in-plane stress resultants (n_{xx}, n_{yy}, n_{xy}) varies according to the nature of variation of the given NEL. For the uniform and NEL-I, the resulting membrane stress distribution coincides with the nature of edge load pattern (Panda and Ramachandra 2010). On the other hand, the stress distribution does not coincide with the load pattern for the NEL-II as already discussed. Hence it is important to calculate the pre-buckling stress state to obtain the critical buckling load (Panda and Ramachandra 2010) for the panels

exposed to NEL-II. Hence a pre buckling analysis is carried out before buckling and free vibration analysis for such load cases. Only the in-plane stress components are considered for this purpose as the transverse shear strains are equal to zero before the buckling. Strain energy associated with the pre-buckling state is given by:

$$\delta u = \int_0^b \int_0^a \left\{ n_{xx} \quad n_{yy} \quad n_{xy} \right\} \begin{Bmatrix} \delta \epsilon_{xx} \\ \delta \epsilon_{yy} \\ \delta \gamma_{xy} \end{Bmatrix} dx dy \quad (2.22)$$

In terms of Airy's stress function, the resultants are given as:

$$n_{yy} = \frac{\partial^2 \aleph}{\partial x^2}, n_{xx} = \frac{\partial^2 \aleph}{\partial y^2}, n_{xy} = -\frac{\partial^2 \aleph}{\partial x \partial y} \quad (2.23)$$

The components of strain are expressed in terms of stresses by the following expression:

$$\begin{Bmatrix} \epsilon_{xx} \\ \epsilon_{yy} \\ \gamma_{xy} \end{Bmatrix} = \begin{bmatrix} a_{11} & a_{12} & 0 \\ a_{12} & a_{22} & 0 \\ 0 & 0 & a_{66} \end{bmatrix} \begin{Bmatrix} n_{xx} \\ n_{yy} \\ n_{xy} \end{Bmatrix} \quad (2.24)$$

where,

$$\begin{aligned} a_{11} &= \frac{A_{22}}{A_{11}A_{22}-A_{12}^2} ; & a_{22} &= \frac{A_{11}}{A_{11}A_{22}-A_{12}^2} \\ a_{12} &= -\frac{A_{12}}{A_{11}A_{22}-A_{12}^2} ; & a_{66} &= \frac{1}{A_{66}} \end{aligned} \quad (2.25)$$

Substituting Equations 2.24 and 2.23 into 2.22 the strain energy equation can be re written as:

$$\begin{aligned} \delta u = \int_0^b \int_0^a & (a_{11} \aleph_{,yy} \delta \aleph_{,yy} + a_{22} \aleph_{,xx} \delta \aleph_{,xx} + a_{12} \aleph_{,xx} \delta \aleph_{,yy} + a_{12} \aleph_{,yy} \delta \aleph_{,xx} \\ & + a_{66} \aleph_{,xy} \delta \aleph_{,xy}) dx dy \end{aligned} \quad (2.26)$$

Approximate values of stress resultants are obtained by assuming the stress function ($\aleph(x, y)$) in a series form given as:

$$\aleph(x, y) = \aleph_0(y) + (x^2 - ax)^2(y^2 - by)^2(c_0 + c_1x + c_2y + c_3x^2 + c_4xy + c_5y^2) \quad (2.27)$$

The function $\aleph_0(y)$ of the stress function for NEL-II can be written as:

1. Parabolic loading

$$\aleph_0 = N_0 \frac{y^3}{3b^2} (2b - y) \quad (2.28)$$

2. Reverse sinusoidal loading

$$\aleph_0 = N_0 \left(\frac{2}{3} \right) \left(\frac{\pi}{\pi - 2} \right) \left(\frac{y^2}{2} + \left(\frac{b^2}{\pi^2} \sin \frac{\pi y}{b} \right) \right) \quad (2.29)$$

3. Increasing parabolic loading

$$\aleph_0 = N_0 \frac{y^4}{6b^2} \quad (2.30)$$

4. Partial edge loading

$$\aleph_0 = N_0 \left(\frac{y^2(d_2 - d_1)}{b} + \sum_{n=1}^{\infty} \frac{b^2}{2n^3\pi^3} \left(\sin \frac{2\pi nd_2}{b} - \sin \frac{2\pi nd_1}{b} \right) \sin^2 \frac{\pi ny}{b} \right) \quad (2.31)$$

Substituting the corresponding value of \aleph_0 in Equation 2.27 the stress function is obtained. Then, the stress function is substituted in Equation 2.26 and minimized with respect to the constants ($c_0, c_1, c_2, c_3, c_4, c_5$) given as:

$$\frac{\partial u}{\partial c_0} = 0 \quad ; \quad \frac{\partial u}{\partial c_1} = 0 \quad ; \quad \frac{\partial u}{\partial c_2} = 0 \quad ; \quad \frac{\partial u}{\partial c_3} = 0 \quad ; \quad \frac{\partial u}{\partial c_4} = 0 \quad ; \quad \frac{\partial u}{\partial c_5} = 0 \quad (2.32)$$

The constants ($c_0, c_1, c_2, c_3, c_4, c_5$) are evaluated from the resulting algebraic equations and stress resultants are obtained using Equation 2.26.

2.4.2 Semi-Analytical Procedure

The displacement and rotations of the cylindrical panel is approximated by various approximate displacement functions satisfying the corresponding boundary conditions. The approximated displacement functions are then substituted into the differential equations and reduced with the help of Galerkin's method to an eigen-value problem. The boundary conditions and corresponding displacement functions are given as: For the simply supported boundary condition:

$$\left. \begin{array}{l} w_0 = v_0 = 0 \\ M_{xx}^b = M_{xx}^s = \psi_y = 0 \end{array} \right\} x = a, 0 \quad ; \quad \left. \begin{array}{l} w_0 = u_0 = 0 \\ M_{yy}^b = M_{yy}^s = \psi_x = 0 \end{array} \right\} y = b, 0 \quad (2.33)$$

Displacement fields are given as:

$$u_0(x, y) = \sum_{r=1}^l \sum_{s=1}^m U_{rs} e^{i\omega t} \cos\left(\frac{r\pi}{a}x\right) \sin\left(\frac{s\pi}{b}y\right) \quad (2.34)$$

$$v_0(x, y) = \sum_{r=1}^l \sum_{s=1}^m V_{rs} e^{i\omega t} \sin\left(\frac{r\pi}{a}x\right) \cos\left(\frac{s\pi}{b}y\right) \quad (2.35)$$

$$\psi_x(x, y) = \sum_{r=1}^l \sum_{s=1}^m \psi_{xrs} e^{i\omega t} \cos\left(\frac{r\pi}{a}x\right) \sin\left(\frac{s\pi}{b}y\right) \quad (2.36)$$

$$\psi_y(x, y) = \sum_{r=1}^l \sum_{s=1}^m \psi_{yrs} e^{i\omega t} \sin\left(\frac{r\pi}{a}x\right) \cos\left(\frac{s\pi}{b}y\right) \quad (2.37)$$

$$w_0(x, y) = \sum_{r=1}^l \sum_{s=1}^m W_{rs} e^{i\omega t} \sin\left(\frac{r\pi}{a}x\right) \sin\left(\frac{s\pi}{b}y\right) \quad (2.38)$$

Similarly, fully clamped(CCCC) boundary condition is specified as:

$$\left. \begin{array}{l} w_0 = u_0 = v_0 = 0 \\ \psi_x = \psi_y = 0 \end{array} \right\} x = a, 0 \quad ; \quad \left. \begin{array}{l} w_0 = u_0 = v_0 = 0 \\ \psi_x = \psi_y = 0 \end{array} \right\} y = b, 0 \quad (2.39)$$

The following displacement fields are assumed for satisfying the above boundary condition:

$$u_0(x, y) = \sum_{r=1}^l \sum_{s=1}^m U_{rs} e^{i\omega t} \cos\left(\frac{r\pi}{a}x\right) \sin\left(\frac{s\pi}{b}y\right) \quad (2.40)$$

$$v_0(x, y) = \sum_{r=1}^l \sum_{s=1}^m V_{rs} e^{i\omega t} \sin\left(\frac{r\pi}{a}x\right) \cos\left(\frac{s\pi}{b}y\right) \quad (2.41)$$

$$\psi_x(x, y) = \sum_{r=1}^l \sum_{s=1}^m \psi_{xrs} e^{i\omega t} \cos\left(\frac{r\pi}{a}x\right) \sin\left(\frac{s\pi}{b}y\right) \quad (2.42)$$

$$\psi_y(x, y) = \sum_{r=1}^l \sum_{s=1}^m \psi_{yrs} e^{i\omega t} \sin\left(\frac{r\pi}{a}x\right) \cos\left(\frac{s\pi}{b}y\right) \quad (2.43)$$

$$w_0(x, y) = \left\{ \begin{array}{l} \sum_{r=1}^l \sum_{s=1}^m W_{rs} e^{i\omega t} \cos \xi_r \left(\frac{x}{a} - \frac{1}{2} \right) + \frac{\sin(\xi_r/2)}{\sinh(\xi_r/2)} \cosh \xi_r \left(\frac{x}{a} - \frac{1}{2} \right) \\ \cos \xi_s \left(\frac{y}{b} - \frac{1}{2} \right) + \frac{\sin(\xi_s/2)}{\sinh(\xi_s/2)} \cosh \xi_s \left(\frac{y}{b} - \frac{1}{2} \right) \quad (r, s = 2, 4, 6) \\ \text{where, } \xi_r \text{ are the roots obtained from } \tan\left(\frac{\xi_r}{2}\right) + \tanh\left(\frac{\xi_r}{2}\right) = 0 \\ \text{and, } \xi_s \text{ are the roots obtained from } \tan\left(\frac{\xi_s}{2}\right) + \tanh\left(\frac{\xi_s}{2}\right) = 0 \end{array} \right. \quad (2.44)$$

$$w_0(x, y) = \left\{ \begin{array}{l} \sum_{r=1}^l \sum_{s=1}^m W_{rs} e^{i\omega t} \sin \xi_r \left(\frac{x}{a} - \frac{1}{2} \right) + \frac{\sin(\xi_r/2)}{\sinh(\xi_r/2)} \cosh \xi_r \left(\frac{x}{a} - \frac{1}{2} \right) \\ \sin \xi_s \left(\frac{y}{b} - \frac{1}{2} \right) + \frac{\sin(\xi_s/2)}{\sinh(\xi_s/2)} \cosh \xi_s \left(\frac{y}{b} - \frac{1}{2} \right) \quad (r, s = 1, 3, 5) \\ \text{where, } \xi_r \text{ are the roots obtained from } \tan\left(\frac{\xi_r}{2}\right) - \tanh\left(\frac{\xi_r}{2}\right) = 0 \\ \text{and, } \xi_s \text{ are the roots obtained from } \tan\left(\frac{\xi_s}{2}\right) - \tanh\left(\frac{\xi_s}{2}\right) = 0 \end{array} \right. \quad (2.45)$$

The substitution of displacement approximations in Equations 2.14a-2.14e and applying Galerkin's method, the following eigen value problems are obtained as:

$$\begin{aligned}
 & \left[[K] - N_{cr}[K_G] \right] \{d_t\} = 0 \quad ; \quad \text{Buckling} & \text{(a)} \\
 & \left[[K] - \omega_n^2[M] \right] \{d_t\} = 0 \quad ; \quad \text{Free vibration without pre-stress} & \text{(b)} \\
 & \left[\left([K] - \delta N_{cr}[K_G] \right) - \omega_n^2[M] \right] \{d_t\} = 0 \quad ; \quad \text{Free vibration with pre-stress} & \text{(c)}
 \end{aligned}
 \tag{2.46}$$

Here $[K]$ denotes stiffness matrix, $[K_G]$ denotes geometric stiffness matrix and N_{cr} specifies the critical buckling load. Also, $[M]$ denotes the mass matrix and ω_n^2 is the eigen value, its square root is the circular natural frequency. For the pre-stressed vibration problem, the value of natural frequencies at various fractions ($\delta = 0.1, 0.2, 0.3, \dots, 1$) of critical buckling load (N_{cr}) are obtained by solving the eigen value problem given by Equation 2.46 (c).

2.5 Validation

In this section, the accuracy of the present approach in predicting buckling and free vibration characteristics of cylindrical panels subjected to NELs is demonstrated by the comparison of the present results with results available in the literature. Thus, this section establishes the accuracy of the generalised frame work followed in present work in predicting the buckling and free vibration characteristics. The validation studies presented in this section are corresponding to an isotropic material. However, the comparison of the results is also presented in the subsequent chapters with respect to the material analyzed in that chapter.

Table 2.2: Comparison of critical buckling load $\left(\bar{N}_0 = N_{cr}\left(\frac{b^2}{\pi^2 D}\right); D = \frac{Eh^3}{12(1-\nu^2)}\right)$ of a SSSS square isotropic plate under different NELs.

Method	Loading type						
	Uniform	Trapezoidal	Triangular	Partial tension	Parabolic	Reverse sinusoidal	Increasing parabolic
Present	3.9980	5.3307	7.9960	13.2087	5.2564	8.2610	6.4515
Adhikari <i>et al.</i> (2020)	3.9978	5.3158	7.8075	13.5046	5.2395	8.1514	6.0713
Difference [%]	0.005	0.27	2.35	2.2	0.32	1.32	5.89

2.5.1 Buckling Load Calculation

Buckling results of a cylindrical panel under different edge loadings is not available in open literature for the comparison of solutions of present approach. So, a simply supported isotropic plate under different NELs analyzed by Adhikari *et al.* (2020) is considered for the validation. The solutions for the plate is obtained using the current solutions derived for the cylindrical panel, by setting $R \rightarrow \infty$. Table 2.2 depicts the comparison of critical buckling load $\left(\bar{N}_0 = N_{cr}\left(\frac{b^2}{\pi^2 D}\right)\right)$ of a simply supported isotropic plate obtained using present formulation with Adhikari *et al.* (2020). Buckling analysis under different NELs of a simply supported isotropic plate has been investigated by Adhikari *et al.* (2020) using the FEM. The material properties used in this analysis are $E=1 \text{ GPa}$, $\nu=0.3$. The difference between results (Table 2.2) of present semi-analytical and FEM is due to the difference in methodology followed for the estimation of pre-buckling stresses due to the NELs.

Table 2.3: Buckling load $\left(\bar{N}_0 = N_{cr}\left(\frac{b}{D}\right); D = \frac{Eh^3}{12(1-\nu^2)}\right)$ validation for an isotropic plate simply supported (SSSS) at its ends under partial edge loading.

$\frac{a}{b}$	Present	Kumar <i>et al.</i> (2016)	Singh <i>et al.</i> (2022)
1	29.99	29.97	30.15

Similarly, Kumar *et al.* (2016) and Singh *et al.* (2022) investigated buckling behaviour of a square isotropic plate ($\nu=0.3$ and $E=200 \text{ GPa}$; $\frac{a}{b}=1$ and $\frac{b}{h}=100$) having simply supported boundary condition using analytical methods subjected to partial edge loading. The critical buckling load values are compared in Table 2.3 for partial edge

load case.

2.5.2 Free Vibration Frequency Calculation

To validate the free vibration results obtained using the present approach, the non-dimensional natural frequency $\left(\Omega = \omega_n \left(\frac{a^2}{h} \sqrt{\frac{\rho_m}{E_m}}\right)\right)$ of an isotropic cylindrical panel ($\nu=0.34$ and $E=3$ GPa, $\rho = 1200 \frac{kg}{m^3}$) subjected to different boundary conditions obtained using the present formulation is verified with the results reported by Van Do and Lee (2020). The free vibration response of an isotropic cylindrical panel is analyzed by Van Do and Lee (2020) using isogeometric method formulated based on Reddy's HSDT. Excellent agreement between present results and Van Do and Lee (2020) results are observed.

Table 2.4: Comparison of non-dimensional fundamental frequency $\left(\Omega = \omega_n \left(\frac{a^2}{h} \sqrt{\frac{\rho_m}{E_m}}\right)\right)$ of an isotropic cylindrical panel ($\frac{a}{b} = 1$, $\frac{a}{h} = 20$ and $R = 10m$) with Van Do and Lee (2020)

$\frac{R}{a}$	Boundary Condition			
	SSSS		CCCC	
	Van Do and Lee (2020)	Present	Van Do and Lee (2020)	Present
5	6.3163	6.3162	11.3115	11.1835
10	6.0826	6.0825	10.8810	11.0357
20	6.0226	6.0225	10.7705	10.9984
50	6.0057	6.0055	10.7393	10.9879
100	6.0032	6.0031	10.7348	10.9864

2.6 Closure

A detailed discussion about the methodology adopted to carry out the buckling and free vibration analysis of cylindrical panels subjected to different NELs is presented. The detailed steps involved in the buckling and free vibration analysis is given as a flow chart. For certain type of NELs (NEL-II), the determination of stress distribution is car-

ried out first. By using a higher order shear deformation theory and considering non-linear strains, the governing differential equations are derived using Hamilton's principle. The governing differential equations are solved by considering semi-analytical method based on Galerkin's method. The methodology developed is used for obtaining buckling and free vibration characteristics of cylindrical panels discussed in the chapters following.

CHAPTER 3

FREE VIBRATION-BUCKLING ANALYSIS ON GPL-POROUS CYLINDRICAL PANEL

3.1 Introduction

A detailed study carried out on the buckling and free vibration characteristics of GPL reinforced porous cylindrical panel under different NELs is presented in this chapter. When thin curved panels made of GPL reinforced porous advanced composite materials are subjected to compressive loads, failure may occur due to buckling. These compressive loads may not be always uniform and are at times turned to NELs in actual practical circumstances. In the presence of NELs the pre-buckling analysis is carried out to calculate the in-plane stress resultants. Thereafter, a semi analytical approach is adopted using Galerkins method to study the buckling and dynamic behaviour of GPL reinforced porous cylindrical panels under different type of NELs.

3.2 Modelling of GPL-Porous Cylindrical Panel

The cylindrical panel considered has graded distribution of both GPL and pores through the thickness. Three different GPL graded patterns namely, GPL 1, GPL 2, and GPL 3 and three different types of functionally graded porosities namely, porosity distribution (PD) A, B and, C are considered in this research. Alternate naming for different distributions for better understanding is given in Table 3.1. Schematic diagram of different GPL patterns examined in the current study is shown in Figure 3.1. In Figure 3.1, dark colour represents a layer with high amount of GPL and white colour represents pure

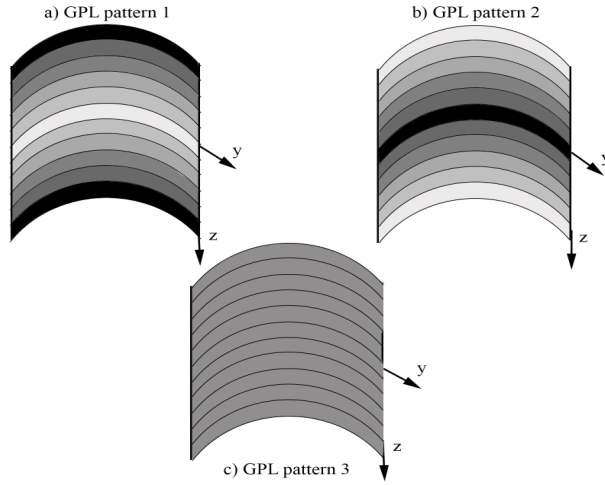


Figure 3.1: Different GPL patterns

Table 3.1: Alternate naming for different distributions

Sl No.	Pattern/Distribution	Alternate Name
1	GPL-1	Symmetric Increasing GPL Pattern
2	GPL-2	Symmetric Decreasing GPL Pattern
3	GPL-3	Uniform GPL Pattern
4	PD-A	Symmetric Decreasing Porosity Distribution
5	PD-B	Symmetric Increasing Porosity Distribution
6	PD-C	Uniform Porosity Distribution

matrix while other colours shows layers with in between amount of GPL. From Figure 3.1, it is noted that the GPL pattern 3 has same amount of GPL, i.e., constant volume fraction of GPL (V_{GPL}) through out the thickness. For GPL pattern 1, V_{GPL} is high at top and bottom layers and reduces to zero at the middle layer while, GPL pattern 2 has V_{GPL} zero at top and bottom layers and increases to maximum at the middle layer.

The schematic representation of the different porosity patterns are shown in Figure 3.2. In porosity distribution A (PD-A): the amount of pores at the centre of the panel is more and at the surfaces it is less, in porosity distribution B (PD-B): the amount of pores at the centre is less and at the surfaces it is more and porosity distribution C (PD-C): the amount of pores is same across the thickness of the panel. The effective material properties associated with the different porosity distribution patterns given by Yang

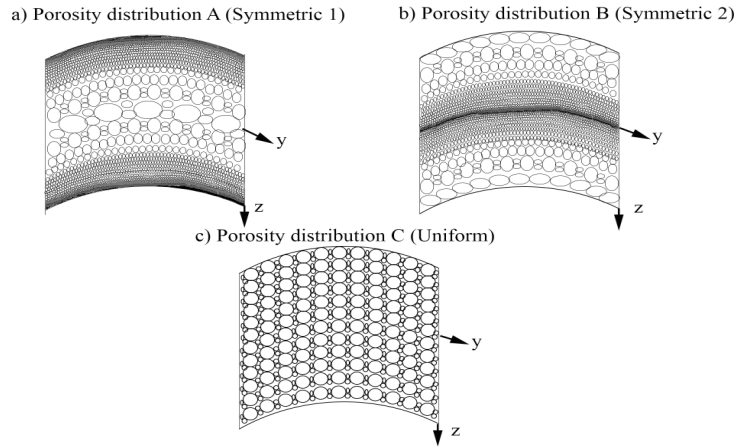


Figure 3.2: Different porosity distributions

et al. (2018) are shown in Table 3.2. Variation of material properties including Young's modulus (E), shear modulus (G) and density (ρ) according to the nature of various porosity distributions are given in Figure 3.3. In Table 3.2, ρ' , E' , G' represents the

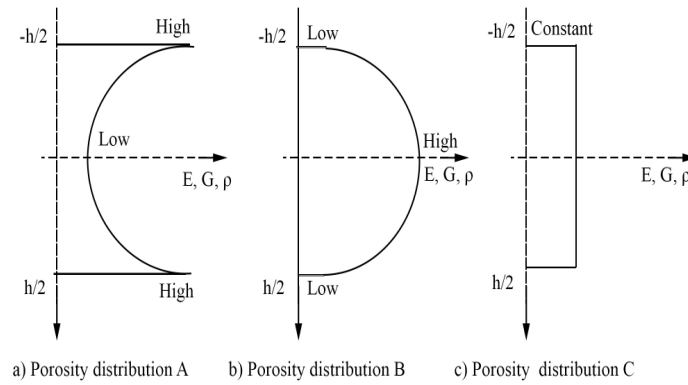


Figure 3.3: Variation of material properties for different porosity distributions

effective density, Young's modulus, and shear modulus of GPL reinforced cylindrical shell panel without porosity respectively. Using extended rule of mixture and Halpin-Tsai micro mechanics model, the effective material properties of FG-GPL reinforced

Table 3.2: Variations of material properties for different types of porosity distributions

Porosity Distribution	$\rho(z)$	$E(z)$	$G(z)$
PD-A	$\rho'[1 - e_m \cos(\frac{\pi z}{h})]$	$E'[1 - e_0 \cos(\frac{\pi z}{h})]$	$G'[1 - e_0 \cos(\frac{\pi z}{h})]$
PD-B	$\rho'[1 - e'_m(1 - \cos(\frac{\pi z}{h}))]$	$E'[1 - e'_0(1 - \cos(\frac{\pi z}{h}))]$	$G'[1 - e'_0(1 - \cos(\frac{\pi z}{h}))]$
PD-C	$\rho'\alpha^*$	$E'\alpha$	$G'\alpha$

shell are defined as given in Equation 3.1.

$$\begin{aligned}
 \rho' &= V_{GPL}\rho_{GPL} + (1 - V_{GPL})\rho_m \\
 E' &= \frac{3}{8} \left(\frac{1 + \xi_L^{GPL} \eta_L^{GPL} V_{GPL}}{1 - \eta_L^{GPL} V_{GPL}} \right) E_m + \frac{5}{8} \left(\frac{1 + \xi_W^{GPL} \eta_W^{GPL} V_{GPL}}{1 - \eta_W^{GPL} V_{GPL}} \right) E_m \\
 \nu' &= V_{GPL}\nu_{GPL} + (1 - V_{GPL})\nu_m \\
 G' &= \frac{E'}{2(1 + \nu')}
 \end{aligned} \tag{3.1}$$

In which, E_m is the Young's modulus of the composite matrix material. While, V_{GPL} , ρ_{GPL} , ν_{GPL} represents volume fraction, density and Poisson's ratio of the reinforcement(GPL) and ρ_m , ν_m are density and Poisson's ratio of the composite matrix material. η_L^{GPL} , η_W^{GPL} are parameters represented by:

$$\begin{aligned}
 \eta_L^{GPL} &= \frac{E_{GPL} - E_m}{E_{GPL} + \xi_L^{GPL} E_m} \\
 \eta_W^{GPL} &= \frac{E_{GPL} - E_m}{E_{GPL} + \xi_W^{GPL} E_m}
 \end{aligned} \tag{3.2}$$

where, E_{GPL} represents Young's modulus of reinforcement(GPL) layer and parameters ξ_L^{GPL} , ξ_W^{GPL} are related to dimensions of GPLs defined as:

$$\begin{aligned}
 \xi_L^{GPL} &= \frac{2l_{GPL}}{t_{GPL}} \\
 \xi_W^{GPL} &= \frac{2w_{GPL}}{t_{GPL}}
 \end{aligned} \tag{3.3}$$

where, t_{GPL} , l_{GPL} , w_{GPL} are the average thickness, length, width of GPL platelets.

The volume fraction of reinforcement(GPL) V_{GPL} for the different graded patterns

of GPL is expressed as follows:

$$V_{GPL}(z) = \begin{cases} V_{ia}[1 - \cos(\frac{\pi z}{h})] & \text{GPL Pattern 1} \\ V_{ib} \cos(\frac{\pi z}{h}) & \text{GPL Pattern 2} \\ V_{ic} & \text{GPL Pattern 3} \end{cases} \quad (3.4)$$

where, V_{ia} , V_{ib} and V_{ic} ($i = a, b, c$) are high values of volume content as given below. The value $i = a, b, c$ corresponds to porosity distribution A, B, C.

$$\begin{cases} V_{ia} = \frac{V_{GPL}^F \sum_{k=1}^n \frac{\rho(z_k)}{\rho'}}{\sum_{k=1}^n \frac{\rho(z_k)}{\rho'} [1 - \cos(\frac{\pi z_k}{h})]} & : & V_{ic} = \frac{V_{GPL}^F \sum_{k=1}^n \frac{\rho(z_k)}{\rho'}}{\sum_{k=1}^n \frac{\rho(z_k)}{\rho'}} \\ V_{ib} = \frac{V_{GPL}^F \sum_{k=1}^n \frac{\rho(z_k)}{\rho'}}{\sum_{k=1}^n \frac{\rho(z_k)}{\rho'} \cos(\frac{\pi z_k}{h})} \end{cases} \quad (3.5)$$

in which,

$$z_k = \left(\frac{1}{2} + \frac{1}{2n} - \frac{k}{n} \right), k = 1, 2, 3, \dots, n \quad (3.6)$$

Here, V_{GPL}^F denote total volume fraction of GPLs and it is given by

$$V_{GPL}^F = \frac{\Lambda_{GPL} \rho_m}{\Lambda_{GPL} \rho_m + \rho_{GPL} - \Lambda_{GPL} \rho_{GPL}} \quad (3.7)$$

In Table 3.2, e_0 , e'_0 , and α are porosity coefficients which are used to specify the changes in Young's modulus and shear modulus with porosity while density coefficients e_m , e'_m , and α^* are used to specify the effect of porosity on density of the composite. For open cell foams, Young's modulus, E , is related to density (Gibson and Ashby 1982, 1999) as:

$$\left(\frac{\rho(z)}{\rho'} \right)^2 = \frac{E(z)}{E'} \quad (3.8)$$

It is assumed that mass of the panels having different porosity pattern is equal as (Yang

Table 3.3: Porosity coefficients for different distributions

PD-A	PD-B	PD-C
e_0	e'_0	α
0.1	0.1738	0.9361
0.2	0.3442	0.8716
0.3	0.5103	0.8064
0.4	0.6708	0.7404
0.5	0.8231	0.6733
0.6	0.9612	0.6047

et al. 2018; Wang and Zhang 2019). This assumption leads to the following equations:

$$\int_0^{h/2} \sqrt{1 - e_0 \cos\left(\frac{\pi z}{h}\right)} dz = \begin{cases} \int_0^{h/2} \sqrt{1 - e'_0(1 - \cos\left(\frac{\pi z}{h}\right))} dz \\ \int_0^{h/2} \sqrt{\alpha} dz \end{cases} \quad (3.9)$$

Based on Equation 3.9, the values of e'_0 and α for the given value of e_0 are calculated and given in Table 3.3. The relation between density co-efficients (e_m, e'_m, α^*) and porosity co-efficients (e_0, e'_0, α) using Equation 3.8 are given as:

$$\begin{cases} e_m = \frac{1 - \sqrt{1 - e_0 \cos\left(\frac{\pi z}{h}\right)}}{\cos\left(\frac{\pi z}{h}\right)} \\ e'_m = \frac{1 - \sqrt{1 - e'_0(1 - \cos\left(\frac{\pi z}{h}\right))}}{(1 - \cos\left(\frac{\pi z}{h}\right))} \\ \alpha^* = \sqrt{\alpha} \end{cases} \quad (3.10)$$

3.3 Validation of the Material Modelling

To validate the material modelling of GPL reinforced porous cylindrical panel, the dimensionless fundamental frequency ($\Omega = \omega_n a(\sqrt{\frac{I^*}{A^*}})$) of GPL reinforced porous nano composite plate having $\frac{a}{b}=1$, $\frac{a}{h}=20$, $\Lambda_{GPL} = 1.0wt\%$, $e_0 = 0.5$, analyzed by Yang *et al.* (2018) is compared with the results obtained using the present approach. Here, I^* and A^* are values of I_1 and A_{11} corresponding to pure matrix material. The solutions for the plate is obtained using the current solutions derived for the cylindrical panel, by setting

$R \rightarrow \infty$. The results are presented in Table 3.4 and the present results match well with Yang *et al.* (2018).

3.4 Free Vibration and Buckling Characteristics for GPL-Porous Cylindrical Panel

The free vibration and buckling behaviour of porous cylindrical panel reinforced with functionally graded-GPL (FG-GPL) is presented in this section. Influences of different combinations of porosity distributions and GPL patterns as given in Table 3.5 on buckling and vibration properties are analysed. CCCC-all edges clamped, SSSS-all edges simply supported and CSCS - two opposite edges clamped and other two edges simply supported starting from left edge are the three different boundary conditions considered for the free vibration analysis. The effect of three different radius ratio ($\frac{R}{a} = 5, 10, 20$) on buckling and vibration behaviours is also presented. The functionally graded-porous-GPL (FG-P-GP)L reinforced cylindrical shell consists of copper ($E_m = 130\text{GPa}$, $\rho_m = 8960\text{kg/m}^3$, $\nu_m = 0.34$) as matrix and GPL ($E_{GPL} = 1.01\text{TPa}$, $\rho_{GPL} = 1062.5 \frac{\text{kg}}{\text{m}^3}$, $w_{GPL} = 1.5\mu\text{m}$, $l_{GPL} = 2.5\mu\text{m}$, $t_{GPL} = 1.5\text{nm}$, $\nu_{GPL} = 0.186$) as reinforcement.

3.4.1 Buckling Studies

The buckling analysis is conducted on a square ($\frac{a}{b} = 1$) cylindrical panel with a thickness ratio of $\frac{a}{h} = 20$ under different NELs. The cylindrical panel is simply supported at its edges. Initially, the panel is assumed to have a fixed porosity and weight fraction of GPLs ($e_0 = 0.4$, $\Lambda_{GPL} = 1.0\text{wt}\%$). The results are tabulated for different NEL conditions. Buckling analysis is also carried out for different values of porosity coefficients and GPL weight fractions. The buckling coefficient defined as $\bar{N}_0 = N_{cr} \left(\frac{b^2}{100E_m h^3} \right)$ is used to represent the buckling results.

Table 3.4: Comparison of dimensionless fundamental frequency $\left(\Omega = \omega_n a \left(\sqrt{\frac{I^*}{A^*}}\right)\right)$ for GPL reinforced porous nano composite plate under different boundary conditions ($a/b=1$, $a/h=20$, $\Lambda_{GPL} = 1.0wt\%$, $\epsilon_0 = 0.5$)

	$\frac{a}{h} = 20$			$\frac{a}{h} = 30$			$\frac{a}{h} = 40$			$\frac{a}{h} = 50$		
	Yang <i>et al.</i> (2018)	Present	Yang <i>et al.</i> (2018)	Present	Yang <i>et al.</i> (2018)	Present	Yang <i>et al.</i> (2018)	Present	Yang <i>et al.</i> (2018)	Present	Yang <i>et al.</i> (2018)	Present
SSSS Plate												
GPL-1	0.3958	0.3958	0.2657	0.2659	0.1997	0.1548	0.1160	0.1605	0.1600	0.1332	0.1447	0.1240
PD-A	0.3293	0.3302	0.2207	0.2214	0.1658	0.1306	0.1046	0.1050	0.1328	0.1442	0.1447	0.1240
GPL-2	0.3574	0.3582	0.2397	0.2404	0.1801	0.1384	0.1108	0.1111	0.1807	0.1442	0.1447	0.1240
PD-B	0.3072	0.3078	0.2057	0.2061	0.1545	0.1146	0.1046	0.1050	0.1548	0.1237	0.1240	0.1240
GPL-3	0.2754	0.2764	0.1843	0.1849	0.1384	0.1108	0.1108	0.1111	0.1388	0.1108	0.1111	0.1111
PD-C	0.3627	0.3633	0.2433	0.2439	0.1828	0.1464	0.1464	0.1469	0.1834	0.1464	0.1469	0.1469
GPL-1	0.3014	0.3025	0.2018	0.2025	0.1516	0.1214	0.1214	0.1218	0.1521	0.1214	0.1218	0.1218
GPL-2	0.3252	0.3263	0.2179	0.2187	0.1637	0.1311	0.1311	0.1316	0.1643	0.1311	0.1316	0.1316
GPL-3												
CCCC Plate												
GPL-1	0.7022	0.7250	0.4783	0.4873	0.3616	0.2904	0.2936	0.2936	0.3665	0.2904	0.2936	0.2936
PD-A	0.5883	0.6044	0.3987	0.4050	0.3008	0.2413	0.2437	0.2437	0.3043	0.2413	0.2437	0.2437
GPL-2	0.6366	0.6559	0.4324	0.4399	0.3265	0.2620	0.2648	0.2648	0.3307	0.2620	0.2648	0.2648
PD-B	0.5502	0.5634	0.3720	0.3772	0.2805	0.2249	0.2268	0.2268	0.2833	0.2249	0.2268	0.2268
GPL-3	0.4686	0.4778	0.3155	0.3195	0.2375	0.1903	0.1920	0.1920	0.2399	0.1903	0.1920	0.1920
PD-C	0.4953	0.5057	0.3339	0.3382	0.2515	0.2016	0.2033	0.2033	0.2540	0.2016	0.2033	0.2033
GPL-1	0.6456	0.6653	0.4387	0.4464	0.3313	0.2659	0.2687	0.2687	0.3356	0.2659	0.2687	0.2687
PD-A	0.5402	0.5535	0.3652	0.3705	0.2753	0.2207	0.2228	0.2228	0.2783	0.2207	0.2228	0.2228
GPL-2	0.5814	0.5973	0.3938	0.4001	0.2971	0.2383	0.2407	0.2407	0.3006	0.2383	0.2407	0.2407
PD-B												
GPL-3												

Table 3.5: Different combinations in distributions of porosity and GPL

Porosity Distribution	GPL pattern	Combination Notation
PD-A	GPLP-1	GPLP-1-PD-A
	GPLP-2	GPLP-2-PD-A
	GPLP-3	GPLP-3-PD-A
PD-B	GPLP-1	GPLP-1-PD-B
	GPLP-2	GPLP-2-PD-B
	GPLP-3	GPLP-3-PD-B
PD-C	GPLP-1	GPLP-1-PD-C
	GPLP-2	GPLP-2-PD-C
	GPLP-3	GPLP-3-PD-C

Influences of porosity pattern, grading of GPL and radius ratio of simply supported cylindrical panel ($e_0 = 0.4$; $\Lambda_{GPL} = 1.0wt\%$) on buckling coefficient under different NELs are presented in Table 3.6. It is observed that there is a reduction in buckling coefficients with increase in radius ratio due to the reduction in structural stiffness with increase in radius ratio as anticipated. It is notable that the buckling coefficients varies for different combinations of porosity distributions and GPL patterns. This happens due to the alteration in structural stiffness because of combined effects of grading of GPL and porosity. It can be observed that the highest buckling coefficient is obtained for GPLP-1-PD-A case for all the type of loading conditions. Thus, higher volume content of GPL and less amount of pores at the extreme surfaces enhances structural stiffness of the cylindrical panel. On the other hand, lowest buckling coefficient is obtained for GPLP-2-PD-B case. So, less volume content of GPL and more amount of pores at the extreme surfaces reduces structural stiffness of the cylindrical panel. The most important result deduced from Table 3.6 is that the buckling load varies with the type of loading and highest buckling load is obtained for partial tension loading. The presence of small amount of tensile load in the case of partial tension loading is the reason for the increased buckling coefficient value. Further, lowest buckling coefficient value is observed for uniform loading followed by parabolic loading then trapezoidal and then triangular loading. The reason for this is explained as follows: for uniform loading, the entire edge is subjected to maximum load whereas in the case of all other type of

loadings, some part of the geometry is only subjected to a maximum load. Similarly, in the parabolic loading case the variation of load is parabolic and the middle portion of the edge is subjected to maximum load hence, the buckling load is less compared to trapezoidal and triangular loads.

Figure 3.4 depicts the variation in buckling coefficients with the porosity coefficient for different types of NELs. In Figure 3.4, the solid, dotted and dash dot lines represents buckling coefficients for porosity distribution cases PD-A, B, C respectively. It is noteworthy that there is a reduction in buckling coefficient with increase in porosity coefficient for all the loading conditions. This is anticipated as the increase in porosity coefficient (increase in amount of pores in the panel) leads to a reduction in both shear modulus and Young's modulus of the porous FG-GPL cylindrical panel as observed from Table 3.2. It is noteworthy that for a given GPL distribution, the reduction in buckling coefficient with increase in porosity coefficient is high for PD-B and least for PD-A. This can be attributed to reduction rate in structural stiffness of the panel with increase in porosity coefficient for PD-B and PD-A porosity patterns. Thus, grading pattern of pores is an important factor which influences the buckling strength of a porous cylindrical panel. For the maximum amount of porosity ($e_o = 0.6$) considered, highest buckling coefficient is observed for GPLP-1-PD-A. It should be noted that with the presence of more amount of pores ($e_o = 0.6$), the reduction in buckling coefficient is very less for PD-A than the other distributions. This is due to the presence of large size pores at the middle for PD-A distribution with increase in porosity coefficient which leads to enhancement of bending stiffness of the cylindrical panel compared to other porosity patterns. Further more, higher buckling strength is observed for GPLP-3-PD-A than GPLP-1-PD-B and GPLP-1-PD-C even though GPLP-1 has better strength than GPLP-3.

In Figure 3.5, the change in buckling coefficients of the porous FG-GPL cylindrical panel is presented for various values of weight fraction of GPL. The solid, dotted and dash dot lines represents buckling coefficients for GPL distribution patterns GPLP-1,

Table 3.6: Buckling coefficients $\left(\frac{\Lambda_{cr} b^2}{100 E_m h^3}\right)$ for GPL reinforced porous nano composite cylindrical panel under SSSS boundary condition $\left(\frac{a}{b} = 1, \frac{a}{h} = 20, \Lambda_{GPL} = 1.0wt\%, \epsilon_0 = 0.4\right)$ subject to different inplane loadings

R/a	PD-A			PD-B			PD-C		
	GPLP-1	GPLP-2	GPLP-3	GPLP-1	GPLP-2	GPLP-3	GPLP-1	GPLP-2	GPLP-3
	Uniform Loading								
5	0.0627	0.0447	0.0518	0.0446	0.0331	0.0369	0.0556	0.0399	0.0457
10	0.0592	0.0414	0.0484	0.0413	0.0296	0.0334	0.0523	0.0365	0.0423
20	0.0584	0.0406	0.0476	0.0404	0.0287	0.0325	0.0514	0.0357	0.0415
	Trapezoidal Loading								
5	0.0836	0.0597	0.0691	0.0594	0.0442	0.0491	0.0741	0.0532	0.0610
10	0.0790	0.0552	0.0646	0.0550	0.0395	0.0445	0.0697	0.0487	0.0565
20	0.0778	0.0541	0.0635	0.0539	0.0383	0.0434	0.0685	0.0476	0.0553
	Triangular Loading								
5	0.1253	0.0895	0.1036	0.0892	0.0663	0.0737	0.1112	0.0798	0.0914
10	0.1184	0.0828	0.0969	0.0826	0.0592	0.0668	0.1045	0.0731	0.0847
20	0.1167	0.0811	0.0952	0.0809	0.0574	0.0651	0.1028	0.0714	0.0830
	Partial tension Loading								
5	0.2507	0.1790	0.2073	0.1783	0.1326	0.1474	0.2224	0.1597	0.1829
10	0.2369	0.1656	0.1937	0.1651	0.1184	0.1336	0.2090	0.1461	0.1694
20	0.2334	0.1622	0.1904	0.1618	0.1149	0.1301	0.2056	0.1428	0.1660
	Parabolic Loading								
5	0.0722	0.0515	0.0597	0.0513	0.0382	0.0424	0.0640	0.0460	0.0526
10	0.0682	0.0477	0.0558	0.0475	0.0341	0.0385	0.0602	0.0421	0.0488
20	0.0672	0.0467	0.0548	0.0466	0.0331	0.0375	0.0592	0.0411	0.0478

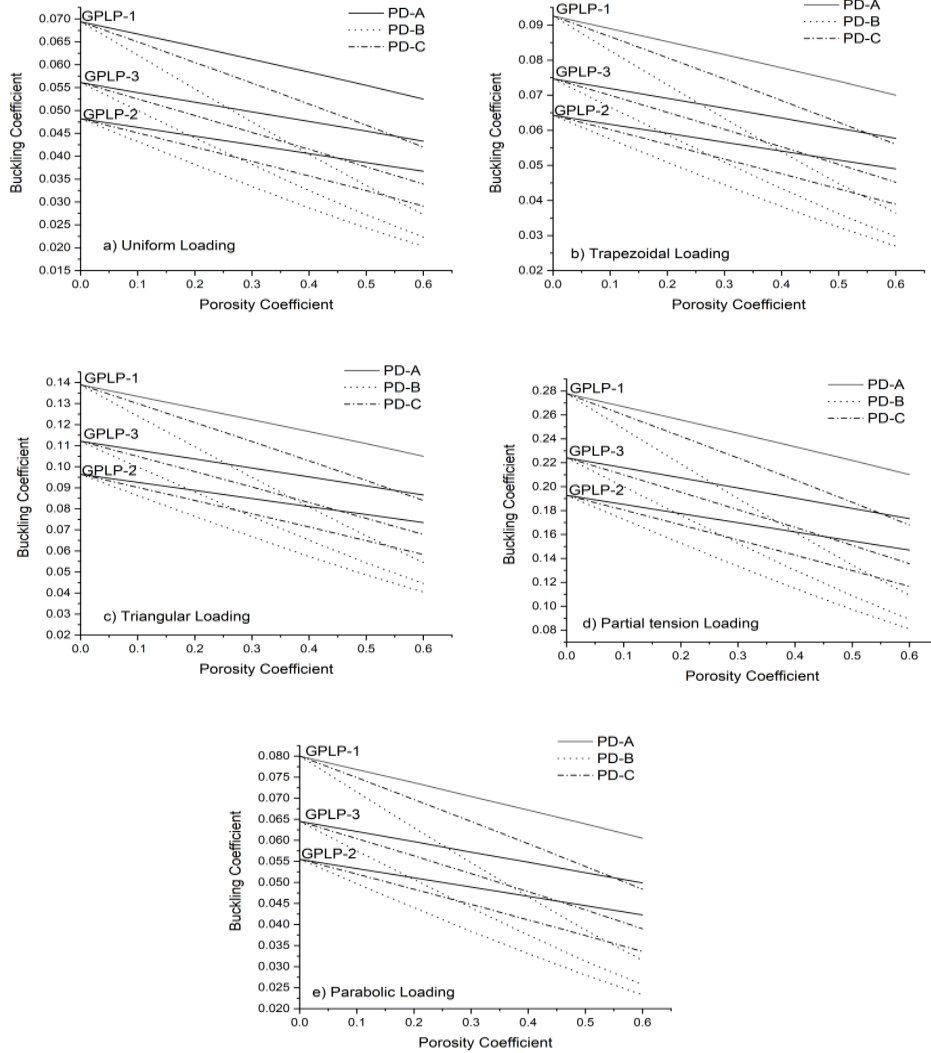


Figure 3.4: Buckling coefficients $\left(\frac{N_{cr}b^2}{100E^m h^3}\right)$ for GPL reinforced porous nano composite cylindrical panel under SSSS boundary condition ($a/b=1$, $a/h=20$, $\Lambda_{GPL} = 1.0wt\%$, $R=20$): effect of porosity coefficient

2, 3 respectively. According to Figure 3.5, it is identified that there is a considerable increase in buckling coefficient with the increase in GPL weight fraction for the all the loading conditions. This is due to excellent reinforcement capability of graphene nano platelets. It is also observed that for a given porosity distribution, the variation

in buckling coefficient is high for GPLP-1 and least for GPLP-2. Thus, reinforcement patterns significantly affects the buckling strength of porous FG-GPL cylindrical panels. The most important result deduced from Figure 3.5 is that at high GPL weight fraction content, the highest buckling strength is observed for GPLP-1-PD-A panel. This is due to the presence of less amount of pores and high content of GPL at the extreme surfaces for GPLP-1-PD-A. It is also observed that at high GPL weight fraction, GPLP-1-PD-C provides a buckling strength higher than GPLP-2-PD-A and GPLP-3-PD-A. This is because GPLP-1 imparts a high amount of strength with increase in weight fraction of GPL.

Figure 3.6 shows the buckling coefficient variation for FG GPL reinforced porous panel with changes in aspect ratio ($\frac{a}{b}$) corresponding to all the loading conditions. From Figure 3.6, it is recognized that with the increase in aspect ratio, the transition of buckling mode from (1,1) to (2,1) happens. This transition in buckling mode is observed for the same aspect ratio irrespective of type of loading and grading of GPL and porosity. It is also observed that, the highest buckling coefficient for the given aspect ratio is observed for GPLP-1-PD-A. Furthermore, the variation of buckling load with aspect ratio ($\frac{a}{b}$) becomes insignificant for aspect ratios higher than 2.5 ($\frac{a}{b} > 2.5$).

3.4.2 Free Vibration Studies

The effect of NEL on the fundamental vibration frequency of functionally graded GPL reinforced porous cylindrical panel is presented. The cylindrical panel with same geometrical parameters of the GPL reinforced porous panel considered for buckling analysis is used for free-vibration studies also. The cylindrical panel analysed has $\frac{a}{b} = 1$ and a thickness ratio of $\frac{a}{h} = 20$. The natural frequency is presented after being non-dimensionalized as $\Omega = \omega_n \left(\frac{a^2}{h} \sqrt{\frac{\rho_m}{E_m}} \right)$.

Table 3.7 consists of dimensionless natural frequency values of functionally graded GPL reinforced porous cylindrical panel without NEL for different values of radius ra-

Table 3.7: Non-dimensional frequency ($\Omega = \omega_n \left(\frac{a^2}{h} \sqrt{\frac{\rho_m}{E_m}} \right)$) for GPL reinforced porous nano composite cylindrical panel under different boundary condition ($a/h=1, a/h=20, \Lambda_{GPL} = 1.0wt\%, e_0 = 0.4$)

R/a	PD-A			PD-B			PD-C		
	GPLP-1	GPLP-2	GPLP-3	GPLP-1	GPLP-2	GPLP-3	GPLP-1	GPLP-2	GPLP-3
				SSSS					
5	8.7543	7.4008	7.9639	7.3873	6.3707	6.7181	8.2492	6.9918	7.4819
10	8.5124	7.1207	7.7016	7.1101	6.0228	6.3964	7.9984	6.6910	7.2026
20	8.4506	7.0487	7.6344	7.0390	5.9324	6.3133	7.9343	6.6135	7.1309
				CCCC					
5	15.6405	13.0925	14.1539	13.0747	11.1001	11.7774	14.6978	12.3107	13.2430
10	15.4918	12.9154	13.9899	12.8997	10.8743	11.5705	14.5422	12.1187	13.0667
20	15.4543	12.8707	13.9485	12.8554	10.8169	11.5181	14.5029	12.0701	13.0221
				CSCS					
5	12.6300	10.5995	11.4452	10.5834	9.0212	9.5566	11.8771	9.9785	10.7198
10	12.4541	10.3927	11.2528	10.3789	8.7601	9.3166	11.6939	9.7551	10.5137
20	12.4097	10.3402	11.2040	10.3270	8.6934	9.2555	11.6475	9.6983	10.4614

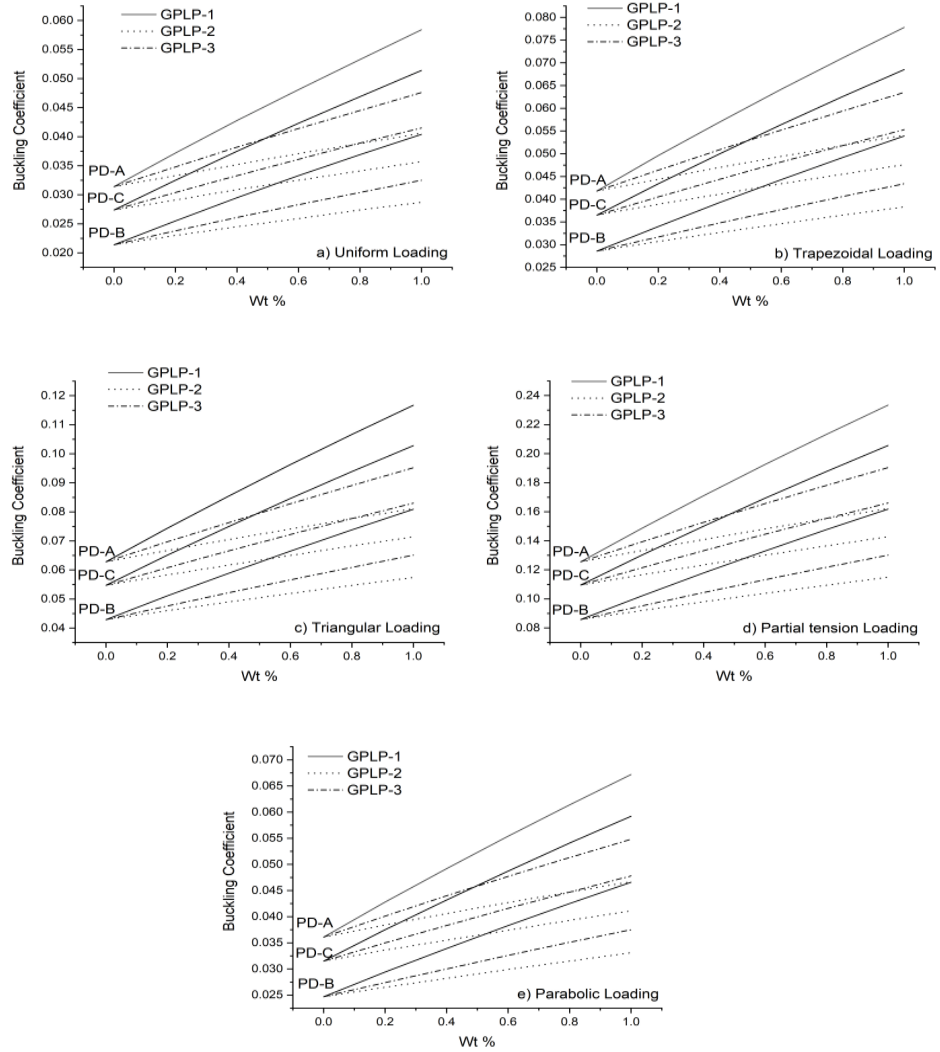


Figure 3.5: Buckling coefficients $\left(\frac{N_{cr} b^2}{100 E^m h^3}\right)$ for GPL reinforced porous nano composite cylindrical panel under SSSS boundary condition ($a/b=1$, $a/h=20$, $e_0 = 0.4$, $R=20$): effect of graphene grading

tio ($\frac{R}{a} = 5, 10, 20$). It is noteworthy that the dimensionless natural frequency reduces as the radius ratio $\frac{R}{a}$ increases. It is also noted that the natural frequency values changes with different combinations of porosity and GPL pattern. This happens due to the differences in bending stiffness of panels with different combinations of porosity and GPL

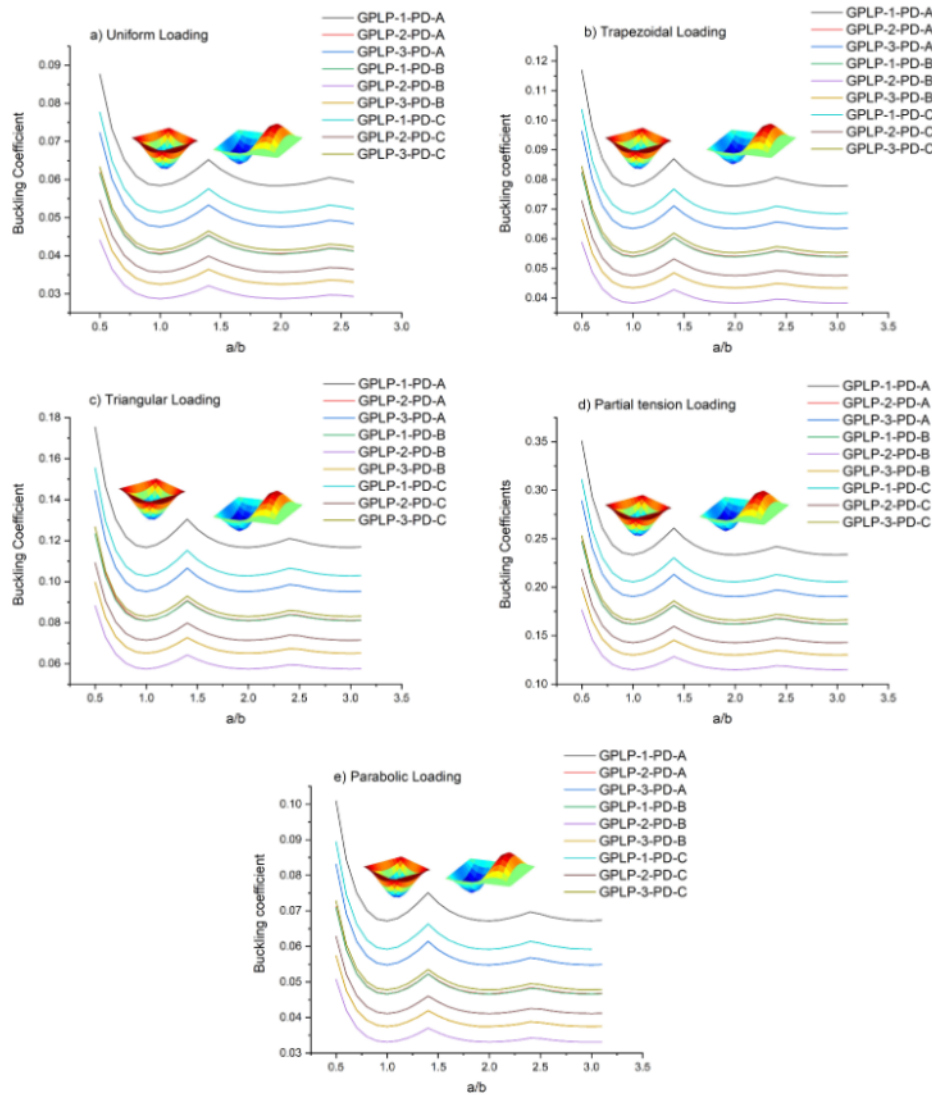


Figure 3.6: Buckling coefficients $\left(\frac{N_{cr}b^2}{100E^m h^3}\right)$ for GPL reinforced porous nano composite cylindrical panel under SSSS boundary condition ($a/b=1$, $a/h=20$, $e_0 = 0.4$, $R=20$): effect of aspect ratio

pattern. It is also recognized that the natural frequency of FG-P-GPL reinforced cylindrical panel changes with the type of boundary conditions. The CCCC (clamped at all edges) boundary condition notes the maximum value of natural frequency and minimum corresponds to SSSS (all edges simply supported).

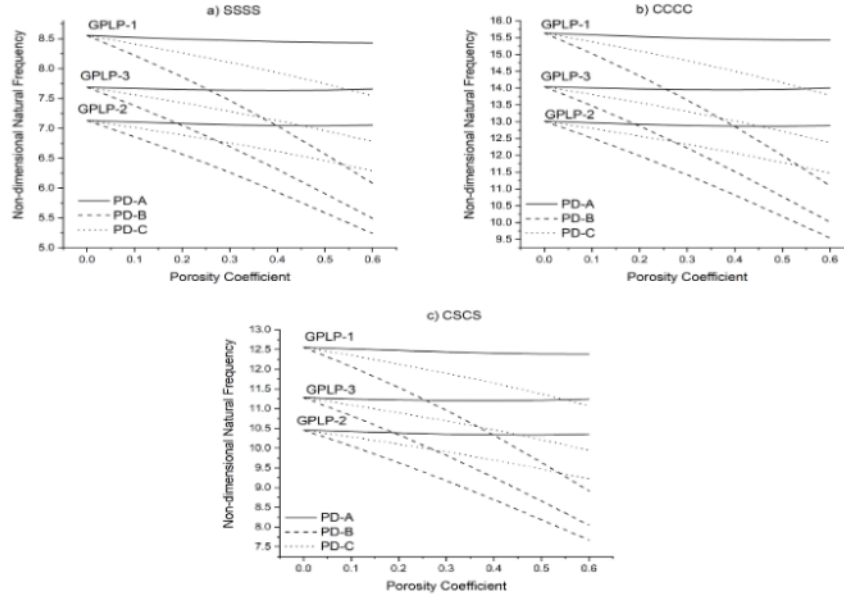


Figure 3.7: Non-dimensional frequency ($\Omega = \omega_n \left(\frac{a^2}{h} \sqrt{\frac{\rho_m}{E_m}} \right)$) for GPL reinforced porous nano composite cylindrical panel under different boundary condition ($\frac{a}{b} = 1$, $\frac{a}{h} = 20$, $\Lambda_{GPL} = 1.0wt\%$, $e_0 = 0.4$, $\frac{R}{a} = 20$): effect of porosity coefficient

Figure 3.7 shows the effect of porosity coefficient on non-dimensional natural frequency for different boundary conditions. In Figure 3.7, PD-A, B, and C are represented by the solid, dash and dotted lines respectively. It is important to note that the increase in porosity coefficient causes only a slight decrease in natural frequency for PD-A. However, notable decrease in natural frequency is observed in the case of PD-B and PD-C cases. This is because of the identical reduction of both bending stiffness and density in the case of PD-A. On the other hand, reduction of stiffness is more in the case of PD-B and PD-C. Furthermore, higher natural frequency value is observed for GPLP-1-PD-A case compared to the other cases. This can be attributed to synergistic effect of grading pattern of GPL and porosity on stiffness of the panel. Since the variation in natural frequency is same for all the boundary conditions, for the sake of brevity, results are presented only for SSSS boundary condition after this point.

Influences of combination of grading pattern of GPL and porosities and nature

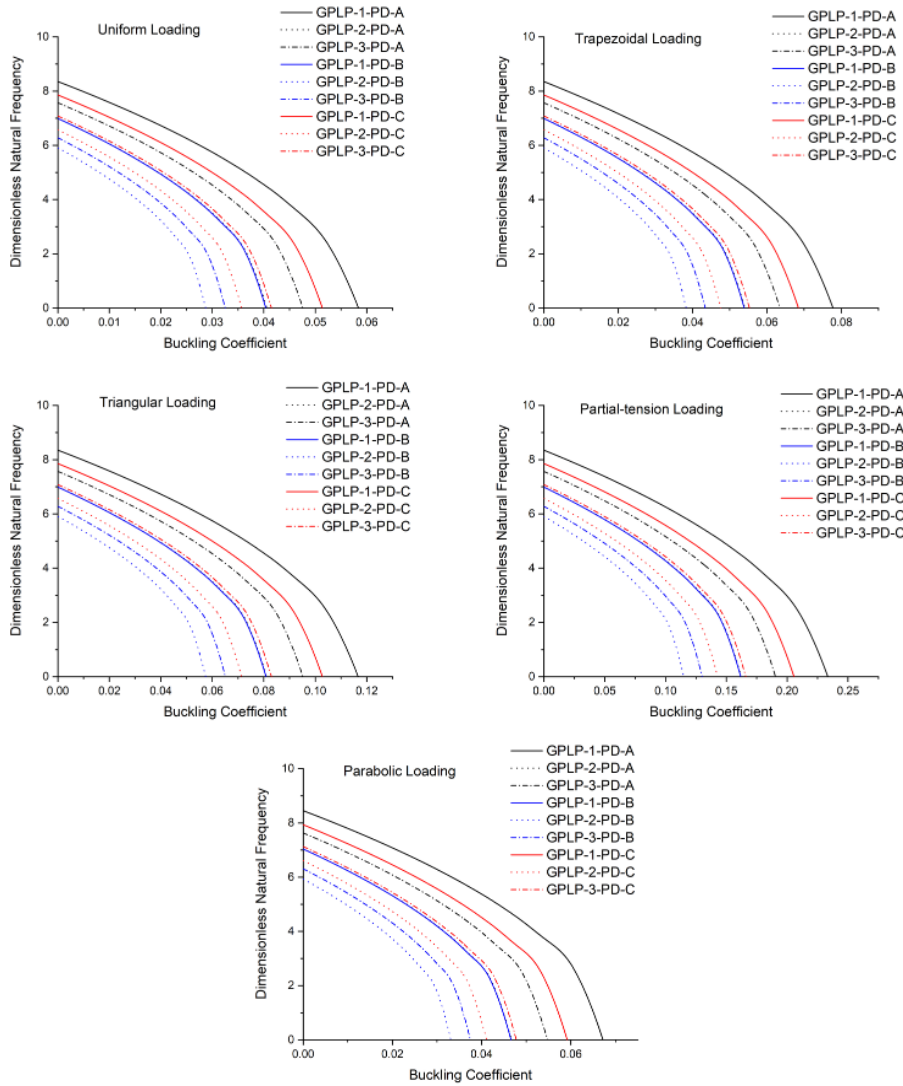


Figure 3.8: Effect of compressive load on the non-dimensional frequency ($\Omega = \omega_n \left(\frac{a^2}{h} \sqrt{\frac{\rho_m}{E_m}} \right)$) for GPL reinforced porous SSSS nano composite cylindrical panel for all the type of loadings.

of NEL on fundamental natural frequency of FG-P-GPL reinforced cylindrical panel with increase in the load intensity are given in Figure 3.8 and Figure 3.9 respectively. The nano composite cylindrical panel ($a/b=1$, $a/h=20$, $\Lambda_{GPL} = 1.0wt\%$, $e_0 = 0.4$, $\frac{R}{a} = 20$) with simply supported boundary condition is considered for this study. Results are presented for all the type of non-uniform edge loading conditions. It can be

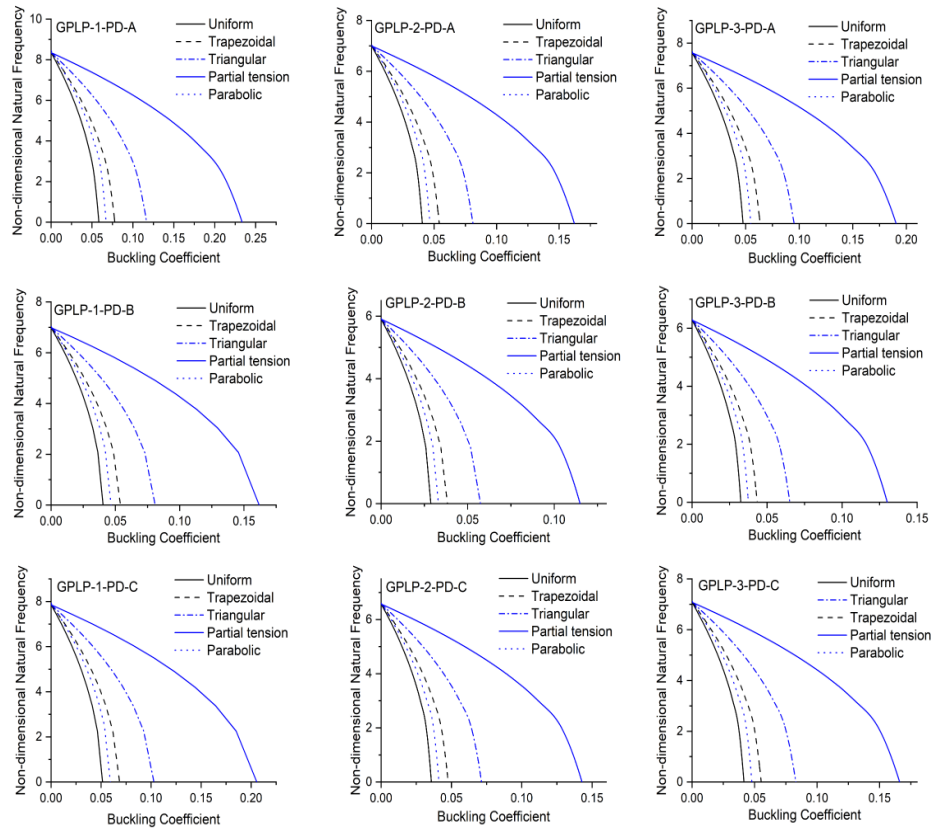


Figure 3.9: Effect of type of edge load on the on-dimensional frequency ($\Omega = \omega_n \left(\frac{a^2}{h} \sqrt{\frac{\rho_m}{E_m}} \right)$) for GPL reinforced porous SSSS nano composite cylindrical panel

observed that with increase in intensity of the NEL, the fundamental frequency of functionally graded GPL reinforced porous panel decreases. In Figure 3.8, the changes in natural frequency are presented for different combinations of GPL patterns and porosity distributions. It is noted that the reduction of natural natural frequency to zero happens at very low load for GPLP-2-PD-B combination. This is expected as the structural stiffness is very low for the same. Figure 3.9 presents the variation in non-dimensional fundamental frequency for different type of edge loading conditions. It may be noted that with increase in amplitude of applied load, the rate of reduction of fundamental frequency is more for uniform loading. The most important result from the Figure 3.9 is that the natural frequency reduction is highest for parabolic loading in the case of

non-uniform edge loadings. It is been observed that free vibration mode shape remains same as (1,1) for all the loading conditions with increase in edge load.

3.5 Closure

Buckling and free vibration characteristics of FG-P-GPL reinforced cylindrical shell panel subjected to uniform and different NELs are investigated. To obtain the solutions, semi analytical method based on higher order shear deformation theory is used. Extended rule of mixture together with modified Halpin-Tsai micromechanics model is used to obtain the material properties of FG-P-GPL reinforced cylindrical panel. The influence of different NELs, radius of curvature, and porosity coefficient on buckling and free vibration behaviour of panels is presented. From the results, it is observed that the type of NEL greatly influences the critical buckling load of the panel. The partial tension loading yields the highest critical buckling load while the uniform edge loading leads to lowest critical buckling load. The non-dimensional buckling loads and natural frequencies varies as per the combination of porosity and GPL distributions. The maximum buckling strength and free vibration resistance is observed for GPLP-1-PD-A panel. The buckling and free vibration responses are influenced by changes in the porosity coefficient and porosity grading pattern. The maximum reduction in stiffness is observed for porosity distribution B while porosity distribution A has minimum reduction in stiffness. The critical buckling mode of functionally graded GPL reinforced porous panel is influenced by the change in aspect ratio.

CHAPTER 4

FREE VIBRATION-BUCKLING ANALYSIS ON GPL-POROUS SANDWICH CYLINDRICAL PANEL

4.1 Introduction

From the previous chapter, it is seen that buckling and free vibration behaviour of cylindrical panel is influenced by the type of edge loading. The influence of distribution of porosity and GPL, amount of porosity and GPL on the buckling and free vibration characteristics are established. The usage of porous-GPL core sandwich cylindrical panel under NELs is analysed next. Buckling analysis of the FG-Porous-GPL core sandwich panel under different important parameters (radius ratio, core to total thickness ratio, porosity coefficients and GPL weight fraction) is presented first followed by the free vibration analysis.

4.2 Modelling of Sandwich Cylindrical Panel with GPL-Porous Core

4.2.1 Mathematical Material Modelling

The porous functionally graded-GPL (FG-GPL) core sandwich cylindrical panel considered for the analysis is shown in Figure 4.1. The geometry of the cylindrical sandwich panel is defined by R-radius, h-thickness, a-length along x direction, b-length along y direction. The thickness of the FG-GPL reinforced porous core is denoted as h_c , while the thickness of the top and bottom face sheets are given as h_{ft} and h_{fb} re-

Table 4.1: Naming for different distributions

SI No.	Pattern/Distribution	Alternate Name
1	U-PD	Uniform Porosity Distribution
2	D-PD	Symmetric Decreasing Porosity Distribution
3	I-PD	Symmetric Increasing Porosity Distribution
4	U-GPL-P	Uniform GPL Pattern
5	I-GPL-P	Symmetric Increasing GPL Pattern
6	D-GPL-P	Symmetric Decreasing GPL Pattern

spectively.

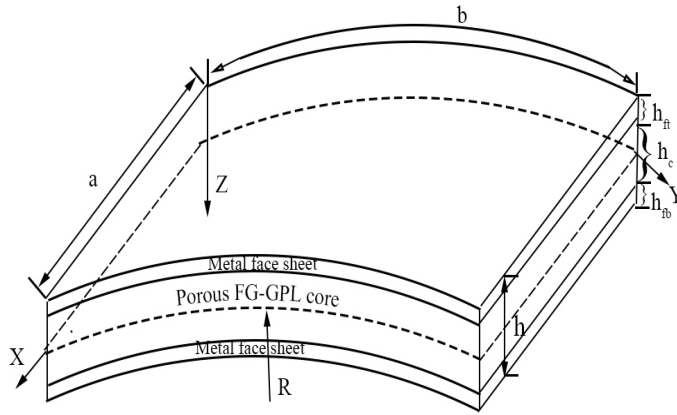


Figure 4.1: Cylindrical sandwich panel with porous FG-GPL core

The core of the sandwich panel is assumed to have both varying porosity and GPL distribution through the thickness. Three types of porosity distributions U-PD, D-PD and I-PD are considered in the present study are shown in Figure 4.2. U-PD denotes uniform porosity, D-PD denotes decreasing porosity distribution where porosity decreases from centre to the surfaces and I-PD denotes increasing porosity distribution where porosity increases from centre to the surfaces. Three GPL distributions such as U-GPL-P, I-GPL-P, D-GPL-P considered are shown in Figure 4.3. For U-GPL-P the amount of GPL is constant through out the thickness, for I-GPL-P the amount of GPL increases from centre to the surfaces while it reduces from centre to surface for D-GPL-P. The naming for easy reference is provided in Table 4.1.

The effective material properties such as density $\rho_c(z)$, Young's modulus $E_c(z)$,

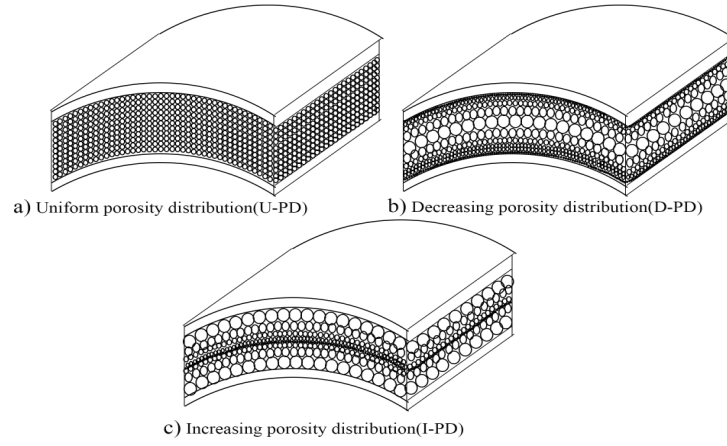


Figure 4.2: Metal foam core with different types of graded porosity

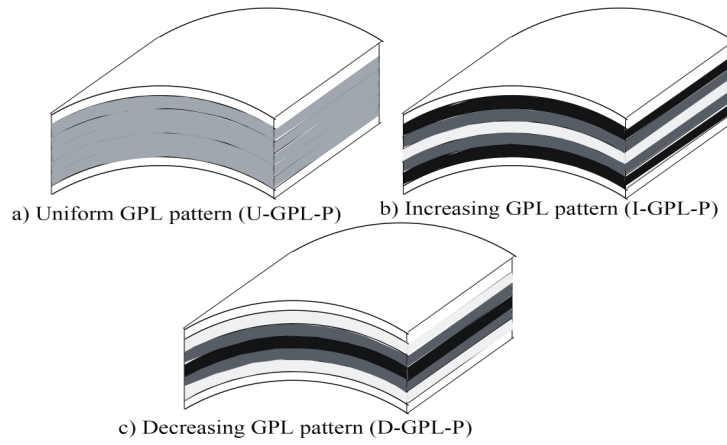


Figure 4.3: Core with different types of GPL patterns

Poisson's ratio $\nu_c(z)$ and shear modulus $G_c(z)$ of the sandwich core are given as (Yang *et al.* 2018)

$$\begin{aligned}
 \rho_c(z) &= \rho_e \Xi_d(z) \\
 E_c(z) &= E_e \Xi_e(z) \\
 \nu_c(z) &= \nu_e \\
 G_c(z) &= G_e \Xi_e(z)
 \end{aligned} \tag{4.1}$$

Where, $\Xi_d(z)$ and $\Xi_e(z)$ are functions representing variation of density and elastic prop-

erties with respect to porosity gradation given as (Yang *et al.* 2018; Wang and Zhang 2019):

$$\Xi_d(z) = \begin{cases} \alpha^* & \text{U-PD} \\ 1 - e_m \cos(\frac{\pi z}{h}) & \text{D-PD} \\ 1 - e'_m(1 - \cos(\frac{\pi z}{h})) & \text{I-PD} \end{cases} \quad (4.2)$$

$$\Xi_e(z) = \begin{cases} \alpha & \text{U-PD} \\ 1 - e_0 \cos(\frac{\pi z}{h}) & \text{D-PD} \\ 1 - e'_0(1 - \cos(\frac{\pi z}{h})) & \text{I-PD} \end{cases} \quad (4.3)$$

Here, α^* , e_m and e'_m are mass density coefficients and α , e_0 , e'_0 are porosity coefficients. The relation between mass density and porosity coefficients for open cell foams (Gibson and Ashby 1982, 1999) is given as:

$$\left(\frac{\rho_c(z)}{\rho_e} \right)^2 = \frac{E_c(z)}{E_e} \quad (4.4)$$

using Equation 4.4, the relationship between mass density and porosity coefficients are given as:

$$\begin{aligned} (\alpha^*)^2 &= \alpha \\ \left(1 - e_m \cos(\frac{\pi z}{h}) \right)^2 &= 1 - e_0 \cos(\frac{\pi z}{h}) \\ \left(1 - e'_m(1 - \cos(\frac{\pi z}{h})) \right)^2 &= 1 - e'_0(1 - \cos(\frac{\pi z}{h})) \end{aligned} \quad (4.5)$$

The relationship between different porosity coefficients is obtained considering the equivalence of mass of panels with different porosity distribution as (Yang *et al.* 2018; Wang and Zhang 2019). The resulting equation is given as:

$$\begin{cases} \int_0^{h/2} \sqrt{1 - e_0 \cos(\frac{\pi z}{h})} dz = \int_0^{h/2} \sqrt{\alpha} dz \\ \int_0^{h/2} \sqrt{1 - e_0 \cos(\frac{\pi z}{h})} dz = \int_0^{h/2} \sqrt{1 - e'_0(1 - \cos(\frac{\pi z}{h}))} dz \end{cases} \quad (4.6)$$

Table 4.2: Porosity coefficients for different distributions

U-PD	D-PD	I-PD
α	e_0	e'_0
0.9361	0.1	0.1738
0.8716	0.2	0.3442
0.8064	0.3	0.5103
0.7404	0.4	0.6708
0.6733	0.5	0.8231
0.6047	0.6	0.9612

The values of α and e'_0 calculated from Equation 4.6, and are presented in Table 4.2. It is assumed that the GPLs are distributed in three different forms through the thickness namely, U-GPL-P, I-GPL-P and D-GPL-P. The volume content of GPL varies for different GPL distribution patterns as:

$$V_{GPL}(z) = s_{ij} \Upsilon(z) \quad (4.7)$$

Where, $\Upsilon(z)$ is a function denoting the variation of volume fraction with GPL pattern given as:

$$\Upsilon(z) = \begin{cases} 1 & \text{U-GPL-P} \\ [1 - \cos(\frac{\pi z}{h})] & \text{I-GPL-P} \\ \cos(\frac{\pi z}{h}) & \text{D-GPL-P} \end{cases} \quad (4.8)$$

and s_{ij} represents the high values of volume content of GPL. In s_{ij} , where j represents particular pattern of GPL while i represents particular pattern of porosity. The total volume fraction of GPL (V_{GPL}^T) is calculated by Equation 4.9 and by using that the relations of s_{iU} , s_{iI} and s_{iD} are given as:

$$V_{GPL}^T = \frac{\Lambda_{GPL} \rho_m}{\Lambda_{GPL} \rho_m + \rho_{GPL} - \Lambda_{GPL} \rho_{GPL}} \quad (4.9)$$

$$\left\{ \begin{array}{l} s_{iU} = \frac{V_{GPL}^T \sum_{l=1}^n \frac{\rho(z_l)}{\rho^l}}{\sum_{l=1}^n \frac{\rho(z_l)}{\rho^l}} \quad \text{U-GPL-P} \\ s_{iI} = \frac{V_{GPL}^T \sum_{l=1}^n \frac{\rho(z_l)}{\rho^l}}{\sum_{l=1}^n \frac{\rho(z_l)}{\rho^l} [1 - \cos(\frac{\pi z_l}{h})]} \quad \text{I-GPL-P} \\ s_{iD} = \frac{V_{GPL}^T \sum_{l=1}^n \frac{\rho(z_l)}{\rho^l}}{\sum_{l=1}^n \frac{\rho(z_l)}{\rho^l} \cos(\frac{\pi z_l}{h})} \quad \text{D-GPL-P} \end{array} \right. \quad (4.10)$$

in which,

$$z_l = \left(-\frac{l}{n} + \frac{1}{2n} + \frac{1}{2} \right), l = 1, 2, 3, \dots, n \quad (4.11)$$

In Equation 4.1, ρ_e , E_e , ν_e , G_e denotes the effective density, Young's modulus, Poisson's ratio, and shear modulus respectively of cylindrical shell panel reinforced with GPL. The effective properties utilizing Halpin-Tsai micro mechanics model and extended rule of mixture (Rafiee *et al.* 2009; Tjong 2013) are specified in Equation 4.12.

$$\begin{aligned} \rho_e &= (1 - V_{GPL})\rho_m + V_{GPL}\rho_{GPL} \\ E_e &= \frac{5}{8} \left(\frac{1 + \xi_W^{GPL} \eta_W^{GPL} V_{GPL}}{1 - \eta_W^{GPL} V_{GPL}} \right) E_m + \frac{3}{8} \left(\frac{1 + \xi_L^{GPL} \eta_L^{GPL} V_{GPL}}{1 - \eta_L^{GPL} V_{GPL}} \right) E_m \\ \nu_e &= (1 - V_{GPL})\nu_m + V_{GPL}\nu_{GPL} \\ G_e &= \frac{E_e}{2(1 + \nu_e)} \end{aligned} \quad (4.12)$$

Here, V_{GPL} , ρ_m and ρ_{GPL} denotes volume content of GPL, density of the metal matrix and density of the GPL respectively. E_m and E_{GPL} represents Young's modulus of the metal matrix and GPL. ξ_L^{GPL} , ξ_W^{GPL} and η_L^{GPL} , η_W^{GPL} are parameters given as:

$$\eta_L^{GPL} = \frac{E_{GPL} - E_m}{E_{GPL} + \xi_L^{GPL} E_m} \quad ; \quad \xi_L^{GPL} = \frac{2l_{GPL}}{t_{GPL}} \quad ; \quad \eta_W^{GPL} = \frac{E_{GPL} - E_m}{E_{GPL} + \xi_W^{GPL} E_m} \quad ; \quad \xi_W^{GPL} = \frac{2w_{GPL}}{t_{GPL}} \quad (4.13)$$

while, ν_{GPL} , ν_m represents Poisson's ratio of GPL and metal matrix and w_{GPL} , t_{GPL} , l_{GPL} are the average width, thickness, length of GPL.

4.2.2 Inertia and Stiffness Coefficients

The inertia and stiffness coefficients of sandwich cylindrical panels are calculated as the summation of coefficients for core and face sheets.

The stress strain relation of porous FG-GPL core layer of cylindrical panel is established considering a layered structure as follows:

$$\begin{Bmatrix} \sigma_{xx}^C \\ \sigma_{yy}^C \\ \tau_{xy}^C \end{Bmatrix}^{(k)} = \begin{bmatrix} Q_{11}^C & Q_{12}^C & 0 \\ Q_{12}^C & Q_{22}^C & 0 \\ 0 & 0 & Q_{66}^C \end{bmatrix}^{(k)} \begin{Bmatrix} \epsilon_{xx} \\ \epsilon_{yy} \\ \gamma_{xy} \end{Bmatrix}^{(k)} \quad (4.14a)$$

$$\begin{aligned} \tau_{yz}^C &= Q_{44}^C \gamma_{yz} \\ \tau_{xz}^C &= Q_{55}^C \gamma_{xz} \end{aligned} \quad (4.14b)$$

Q_{ij}^C are stiffness matrix coefficients of the core are defined and given as:

$$\begin{aligned} Q_{11}^C &= Q_{22}^C = \frac{E_c(z)}{1-(\nu_c)^2} \quad ; \quad Q_{12}^C = \nu_c \frac{E_c(z)}{1-(\nu_c)^2} \\ Q_{66}^C &= Q_{55}^C = Q_{44}^C = G_c(z) \end{aligned} \quad (4.15)$$

Also, for the top and bottom face sheet layers the stress-strain relations are given as:

$$\begin{Bmatrix} \sigma_{xx}^f \\ \sigma_{yy}^f \\ \tau_{xy}^f \end{Bmatrix} = \begin{bmatrix} Q_{11}^f & Q_{12}^f & 0 \\ Q_{12}^f & Q_{22}^f & 0 \\ 0 & 0 & Q_{66}^f \end{bmatrix} \begin{Bmatrix} \epsilon_{xx} \\ \epsilon_{yy} \\ \gamma_{xy} \end{Bmatrix} \quad (4.16a)$$

$$\begin{aligned} \tau_{yz}^f &= Q_{44}^f \gamma_{yz} \\ \tau_{xz}^f &= Q_{55}^f \gamma_{xz} \end{aligned} \quad (4.16b)$$

Q_{ij}^f are stiffness matrix coefficients of the core are defined and given as:

$$\begin{aligned} Q_{11}^f = Q_{22}^f &= \frac{E_m}{1-(\nu_m)^2} \quad ; \quad Q_{12} = \nu_m \frac{E_m}{1-(\nu_m)^2} \\ Q_{66}^f = Q_{55}^f = Q_{44}^f &= G_m(z) \end{aligned} \quad (4.17)$$

The in plane force resultants of the sandwich cylindrical panel are defined as:

$$\begin{aligned} \left\{ \begin{array}{l} N_{xx} \\ N_{yy} \\ N_{xy} \end{array} \right\}, \left\{ \begin{array}{l} M_{xx}^b \\ M_{yy}^b \\ M_{xy}^b \end{array} \right\}, \left\{ \begin{array}{l} M_{xx}^s \\ M_{yy}^s \\ M_{xy}^s \end{array} \right\} &= \int_{\frac{-h}{2}}^{\frac{-h}{2}+h_f} \left(1, z, z - \frac{4}{3} \frac{z^3}{h^2} \right) \left\{ \begin{array}{l} \sigma_{xx}^f \\ \sigma_{yy}^f \\ \tau_{xy}^f \end{array} \right\} dz \\ &+ \int_{\frac{h}{2}-h_f}^{\frac{h}{2}} \left(1, z, z - \frac{4}{3} \frac{z^3}{h^2} \right) \left\{ \begin{array}{l} \sigma_{xx}^C \\ \sigma_{yy}^C \\ \tau_{xy}^C \end{array} \right\} dz + \int_{\frac{h}{2}-h_f}^{\frac{h}{2}} \left(1, z, z - \frac{4}{3} \frac{z^3}{h^2} \right) \left\{ \begin{array}{l} \sigma_{xx}^f \\ \sigma_{yy}^f \\ \tau_{xy}^f \end{array} \right\} dz \end{aligned} \quad (4.18)$$

Similarly, the moment resultants of the sandwich cylindrical panel are defined as:

$$\begin{aligned} \left\{ \begin{array}{l} Q_{xz} \\ Q_{yz} \end{array} \right\} &= \int_{\frac{-h}{2}}^{\frac{-h}{2}+h_f} \left(1 - 4 \frac{z^2}{h^2} \right) \left\{ \begin{array}{l} \tau_{xz}^f \\ \tau_{yz}^f \end{array} \right\} dz \\ &+ \int_{\frac{h}{2}-h_f}^{\frac{h}{2}} \left(1 - 4 \frac{z^2}{h^2} \right) \left\{ \begin{array}{l} \tau_{xz}^C \\ \tau_{yz}^C \end{array} \right\} dz + \int_{\frac{h}{2}-h_f}^{\frac{h}{2}} \left(1 - 4 \frac{z^2}{h^2} \right) \left\{ \begin{array}{l} \tau_{xz}^f \\ \tau_{yz}^f \end{array} \right\} dz \end{aligned} \quad (4.19)$$

Thus, different coefficients for a sandwich cylindrical panel are defined as follows:

$$\begin{aligned} (A_{ij}, B_{ij}, D_{ij}, E_{ij}) &= \int_{\frac{-h}{2}}^{\frac{-h}{2}+h_f} Q_{ij}(1, z, z^2, z - \frac{4}{3} \frac{z^3}{h^2}) dz + \int_{\frac{h}{2}-h_f}^{\frac{h}{2}} Q_{ij}(1, z, z^2, z - \frac{4}{3} \frac{z^3}{h^2}) dz \\ &+ \int_{\frac{h}{2}-h_f}^{\frac{h}{2}} Q_{ij}(1, z, z^2, z - \frac{4}{3} \frac{z^3}{h^2}) dz \\ (F_{ij}, H_{ij}, L_{ij}) &= \int_{\frac{-h}{2}}^{\frac{-h}{2}+h_f} Q_{ij} \left(z(z - \frac{4}{3} \frac{z^3}{h^2}), \left(z - \frac{4}{3} \frac{z^3}{h^2} \right)^2, \left(1 - 4 \frac{z^2}{h^2} \right)^2 \right) dz \\ &+ \int_{\frac{h}{2}-h_f}^{\frac{h}{2}} Q_{ij} \left(z(z - \frac{4}{3} \frac{z^3}{h^2}), \left(z - \frac{4}{3} \frac{z^3}{h^2} \right)^2, \left(1 - 4 \frac{z^2}{h^2} \right)^2 \right) dz \\ &+ \int_{\frac{h}{2}-h_f}^{\frac{h}{2}} Q_{ij} \left(z(z - \frac{4}{3} \frac{z^3}{h^2}), \left(z - \frac{4}{3} \frac{z^3}{h^2} \right)^2, \left(1 - 4 \frac{z^2}{h^2} \right)^2 \right) dz \end{aligned} \quad (4.20)$$

$$\begin{aligned}
(I_1, I_2, I_3) &= \int_{\frac{-h}{2}}^{\frac{-h}{2}+h_f} \rho_m(1, z, z^2) dz \\
&\quad + \int_{\frac{-h}{2}+h_f}^{\frac{h}{2}-h_f} \rho_c(1, z, z^2) dz + \int_{\frac{h}{2}-h_f}^{\frac{h}{2}} \rho_m(1, z, z^2) dz \\
(I_4, I_5, I_6) &= \int_{\frac{-h}{2}}^{\frac{-h}{2}+h_f} \rho_m\left(z - \frac{4}{3} \frac{z^3}{h^2}, z\left(z - \frac{4}{3} \frac{z^3}{h^2}\right), \left(z - \frac{4}{3} \frac{z^3}{h^2}\right)^2\right) dz \\
&\quad + \int_{\frac{-h}{2}+h_f}^{\frac{h}{2}-h_f} \rho_c\left(z - \frac{4}{3} \frac{z^3}{h^2}, z\left(z - \frac{4}{3} \frac{z^3}{h^2}\right), \left(z - \frac{4}{3} \frac{z^3}{h^2}\right)^2\right) dz \\
&\quad + \int_{\frac{h}{2}-h_f}^{\frac{h}{2}} \rho_m\left(z - \frac{4}{3} \frac{z^3}{h^2}, z\left(z - \frac{4}{3} \frac{z^3}{h^2}\right), \left(z - \frac{4}{3} \frac{z^3}{h^2}\right)^2\right) dz
\end{aligned} \tag{4.21}$$

The sandwich cylindrical panel modelling requires the consideration of different coefficients in the governing differential equations as per the above discussion and using these coefficients, buckling and free vibration characteristics are analyzed as discussed in section 2.

4.3 Validation of Sandwich Material Modelling

Validation of material modelling of a sandwich plate is presented in this section. Since no results for a porous GPL core sandwich cylindrical panel is available, by keeping the radius of curvature as infinite ($R \rightarrow \infty$) in the present formulation, the sandwich plate results are compared. The critical buckling coefficient value $\left(N_{cr}\left(\frac{b^2}{100h^3 E_m}\right)\right)$ of a sandwich cylindrical panel subjected to UEL calculated using the present approach is compared with the results of Yaghoobi and Taheri (2020) as shown in Table 4.3. Yaghoobi and Taheri (2020) used Navier's method based analytical solutions to obtain the critical buckling load values of porous GPL core sandwich plate. It can be observed that critical buckling value obtained using present investigation are in good agreement with Yaghoobi and Taheri (2020).

Table 4.3: Comparison of critical buckling values $\bar{N}_0 = N_{cr} \left(\frac{b^2}{100h^3 E_m} \right)$ of open foam cell core sandwich flat panel under uni-axial compression with Yaghoobi and Taheri (2020)

SI No.	Parameters		U-PD		D-PD	
	e_0	$\Lambda_{GPL}(\%)$	Yaghoobi and Taheri (2020)	Present	Yaghoobi and Taheri (2020)	Present
1	0.8	1.25	231.90	231.7639	254.54	254.3446
2	0.8	0.25	224.18	224.0194	241.48	241.2726
3	0.5	0.75	244.72	244.6117	255.54	255.4012
4	0.5	0.25	249.49	249.3321	252.26	252.0996
5	0.2	0.75	255.56	255.4291	256.73	256.5989
6	0.5	1.25	246.15	246.1510	275.16	275.1116
7	0.8	0.75	192.40	192.3944	239.69	239.6387
8	0.5	0.75	244.72	244.6117	255.54	255.4012
9	0.8	0.75	246.37	246.1929	252.30	252.1106
10	0.5	1.25	253.09	254.6213	256.73	256.5785
11	0.5	0.25	217.32	217.3190	239.48	239.4460
12	0.2	0.75	265.85	265.8462	275.22	275.2048
13	0.5	0.75	244.72	244.6117	255.54	255.4012
14	0.2	1.25	266.98	266.8945	271.46	271.3653

4.4 Free Vibration and Buckling Characteristics for GPL-Porous Sandwich Cylindrical Panel

The buckling and free vibration characteristics of porous FG-GPL sandwich cylindrical panel under the influence of various important parameters are presented in this section. In the present study, core and face sheets of the sandwich cylindrical panel are made of aluminium alloy with material properties given as (Yaghoobi and Taheri 2020):

$$\rho_m=2689.8 \frac{kg}{m^3}, \nu_m=0.34, E_m=68.3 \text{ GPa}$$

The material properties of the GPL reinforcement are given as (Yaghoobi and Taheri 2020):

$$\rho_{GPL}=1062.5 \frac{kg}{m^3}, w_{GPL} = 1.5\mu\text{m}, l_{GPL} = 2.5\mu\text{m}, t_{GPL} = 1.5\text{nm}, \nu_{GPL} = 0.186, E_{GPL} = 1.01\text{TPa}$$

In the present study, various boundary conditions are considered with 'S' denoting simply supported boundary and 'C' denoting clamped boundary. The total thickness of the sandwich cylindrical panel is maintained as 10 mm throughout the study. Throughout the study unless otherwise mentioned the following geometric properties are assumed: $\frac{a}{b} = 1$, $e_o = 0.4$, $\Lambda_{GPL} = 1wt\%$, $\frac{h_c}{h_t}=0.8$ and $\frac{R}{a} = 20$.

4.4.1 Buckling Studies

To start with, the buckling analysis is conducted on a square ($\frac{a}{b} = 1$) sandwich cylindrical panel under simply supported (SSSS) boundary condition with a fixed porosity ($e_o = 0.4$) and GPL weight fraction ($\Lambda_{GPL} = 1wt\%$) with core to total thickness ratio ($\frac{h_c}{h_t}=0.8$). For convenience purposes, the critical buckling load is expressed as buckling coefficient given as: $\bar{N}_0 = N_{cr}(\frac{b^2}{100E_m h^3})$

The buckling coefficient value of the sandwich cylindrical panel under different NELs and radius ratio is analyzed and presented in Table 4.4. From Table 4.4, it is

Table 4.4: Buckling coefficient value of GPL reinforced porous sandwich cylindrical panel subjected to different NELs under SSSS boundary condition ($\frac{c}{b} = 1, e_o = 0.4, \Lambda_{GPL} = 1wt\%, \frac{h_c}{h_t} = 0.8$): variation with radius ratio ($\frac{R}{a}$)

GPL Pattern	Porosity Distribution	$\frac{R}{a}$	Loading type						
			Uniform	Trapezoidal	Triangular	Parabolic tension	Reverse sinusoidal	Increasing parabolic	
U-GPL-P		5	0.1377	0.1836	0.2754	0.4550	0.1811	0.2845	0.2222
		10	0.0622	0.0829	0.1244	0.2054	0.0817	0.1285	0.1003
		20	0.0433	0.0577	0.0866	0.1430	0.0569	0.0895	0.0699
I-GPL-P	U-PD	5	0.1412	0.1883	0.2824	0.4666	0.1857	0.2918	0.2279
		10	0.0657	0.0876	0.1314	0.2170	0.0864	0.1357	0.1060
		20	0.0468	0.0624	0.0936	0.1546	0.0615	0.0967	0.0755
D-GPL-P		5	0.1357	0.1809	0.2714	0.4484	0.1784	0.2804	0.2190
		10	0.0602	0.0802	0.1203	0.1988	0.0791	0.1243	0.0971
		20	0.0413	0.0551	0.0826	0.1364	0.0543	0.0853	0.0666
U-GPL-P		5	0.1410	0.1880	0.2821	0.4659	0.1854	0.2914	0.2276
		10	0.0651	0.0869	0.1303	0.2152	0.0856	0.1346	0.1051
		20	0.0462	0.0616	0.0923	0.1525	0.0607	0.0954	0.0745
I-GPL-P	D-PD	5	0.1462	0.1950	0.2924	0.4831	0.1922	0.3021	0.2360
		10	0.0693	0.0924	0.1387	0.2290	0.0911	0.1433	0.1119
		20	0.0501	0.0668	0.1002	0.1655	0.0659	0.1035	0.0809
D-GPL-P		5	0.1377	0.1837	0.2755	0.4551	0.1811	0.2846	0.2223
		10	0.0625	0.0833	0.1250	0.2065	0.0822	0.1291	0.1008
		20	0.0437	0.0582	0.0874	0.1443	0.0574	0.0903	0.0705
U-GPL-P		5	0.1354	0.1805	0.2708	0.4473	0.1780	0.2797	0.2185
		10	0.0585	0.0780	0.1169	0.1932	0.0769	0.1208	0.0944
		20	0.0392	0.0523	0.0785	0.1297	0.0516	0.0811	0.0633
I-GPL-P	I-PD	5	0.1356	0.1808	0.2712	0.4480	0.1783	0.2802	0.2188
		10	0.0606	0.0808	0.1212	0.2003	0.0797	0.1252	0.0978
		20	0.0419	0.0558	0.0837	0.1383	0.0550	0.0865	0.0676
D-GPL-P		5	0.1353	0.1803	0.2705	0.4469	0.1778	0.2795	0.2183
		10	0.0575	0.0766	0.1149	0.1899	0.0756	0.1187	0.0927
		20	0.0380	0.0507	0.0760	0.1256	0.0500	0.0785	0.0613

seen that buckling load decrease substantially with increase in radius ratio as anticipated. This is due to reduction in structural stiffness with increase in radius ratio. It is also observed that the buckling coefficient changes with different types of porosity and GPL distribution patterns. For any given NEL case, highest buckling coefficient value is observed for the sandwich having the core with D-PD porosity and I-GPL-P pattern of GPL distribution. The increased amount of GPL and the least presence of pores towards top and bottom of the sandwich cylindrical panel enhances the buckling coefficient value. Similarly, for any given NEL case, lowest buckling coefficient value is observed for the sandwich having the core with I-PD porosity and D-GPL-P pattern of GPL distribution. The presence of large amount of pores and reduced amount of GPL towards top and bottom of the sandwich cylindrical panel is the reason for reduced buckling coefficient value. Furthermore, for any given type of core analyzed, highest buckling coefficient value is observed for the partial tension loading (Case d) while the lowest value is observed for uniform edge loading (Case a). This is due to the presence of a small amount of tensile load for partial tension loading. Apart from the uniform compressive loading, parabolic edge loading has the reduced buckling coefficient value. This can be explained by considering the fact that parabolic edge compression has the highest load at the center of the cylindrical panel. It is interesting to note that increasing parabolic loading has lower buckling coefficient value than triangular loading. This is due to the fact that for increasing parabolic loading, higher intensity of load is present towards one edge compared to triangular loading.

In order to analyse the effect of core to total thickness ratio on buckling capacity of sandwich cylindrical panel with different distribution of GPL and porosity pattern, three different core to total thickness ratio ($\frac{h_c}{h_t} = 0.4, 0.6, 0.8$) are considered. Fixed porosity ($e_o = 0.4$) and GPL weight fraction ($\Lambda_{GPL} = 1wt\%$) and radius ratio ($\frac{R}{a} = 20$) are considered for this study. Table 4.5 illustrates the buckling coefficient value of a sandwich cylindrical panel under different edge loading with respect to core to total thickness ratio. To have a better understanding, a graphical representation of variation of buckling coefficient with change in core to total thickness ratio ($\frac{h_c}{h_t}$) for uniform

Table 4.5: Buckling coefficient value of GPL reinforced porous sandwich cylindrical panel subjected to different NELs under SSSS boundary condition($\frac{a}{b} = 1, e_o = 0.4, \Lambda_{GPL} = 1wt\%, \frac{R}{a} = 20$) : variation with core to total thickness ratio($\frac{h_c}{h_t}$)

GPL Pattern	Porosity Distribution	$\frac{h_c}{h_t}$	Loading type					Reverse sinusoidal	Increasing parabolic
			Uniform	Trapezoidal	Triangular	Partial tension	Parabolic		
U-GPL-P		0.4	0.0435	0.0580	0.0869	0.1436	0.0571	0.0898	0.0701
		0.6	0.0434	0.0579	0.0868	0.1434	0.0570	0.0897	0.0700
		0.8	0.0433	0.0577	0.0866	0.1430	0.0569	0.0895	0.0699
I-GPL-P	U-PD	0.4	0.0439	0.0585	0.0878	0.1451	0.0577	0.0907	0.0709
		0.6	0.0449	0.0598	0.0898	0.1483	0.0590	0.0927	0.0724
		0.8	0.0468	0.0624	0.0936	0.1546	0.0615	0.0967	0.0755
D-GPL-P		0.4	0.0432	0.0576	0.0864	0.1428	0.0568	0.0893	0.0697
		0.6	0.0426	0.0567	0.0851	0.1406	0.0560	0.0879	0.0687
		0.8	0.0413	0.0551	0.0826	0.1364	0.0543	0.0853	0.0666
U-GPL-P		0.4	0.0438	0.0585	0.0877	0.1448	0.0576	0.0906	0.0707
		0.6	0.0446	0.0595	0.0893	0.1475	0.0587	0.0922	0.0720
		0.8	0.0462	0.0616	0.0923	0.1525	0.0607	0.0954	0.0745
I-GPL-P	D-PD	0.4	0.0444	0.0591	0.0887	0.1466	0.0583	0.0917	0.0716
		0.6	0.0463	0.0618	0.0926	0.1530	0.0609	0.0957	0.0747
		0.8	0.0501	0.0668	0.1002	0.1655	0.0659	0.1035	0.0809
D-GPL-P		0.4	0.0435	0.0580	0.0870	0.1437	0.0572	0.0899	0.0702
		0.6	0.0436	0.0581	0.0871	0.1439	0.0573	0.0900	0.0703
		0.8	0.0437	0.0582	0.0874	0.1443	0.0574	0.0903	0.0705
U-GPL-P		0.4	0.0430	0.0573	0.0860	0.1421	0.0565	0.0889	0.0694
		0.6	0.0417	0.0556	0.0835	0.1379	0.0549	0.0862	0.0673
		0.8	0.0392	0.0523	0.0785	0.1297	0.0516	0.0811	0.0633
I-GPL-P	I-PD	0.4	0.0433	0.0577	0.0865	0.1430	0.0569	0.0894	0.0698
		0.6	0.0428	0.0570	0.0856	0.1414	0.0563	0.0884	0.0690
		0.8	0.0419	0.0558	0.0837	0.1383	0.0550	0.0865	0.0676
D-GPL-P		0.4	0.0429	0.0572	0.0858	0.1417	0.0564	0.0886	0.0692
		0.6	0.0412	0.0550	0.0825	0.1363	0.0542	0.0852	0.0666
		0.8	0.0380	0.0507	0.0760	0.1256	0.0500	0.0785	0.0613

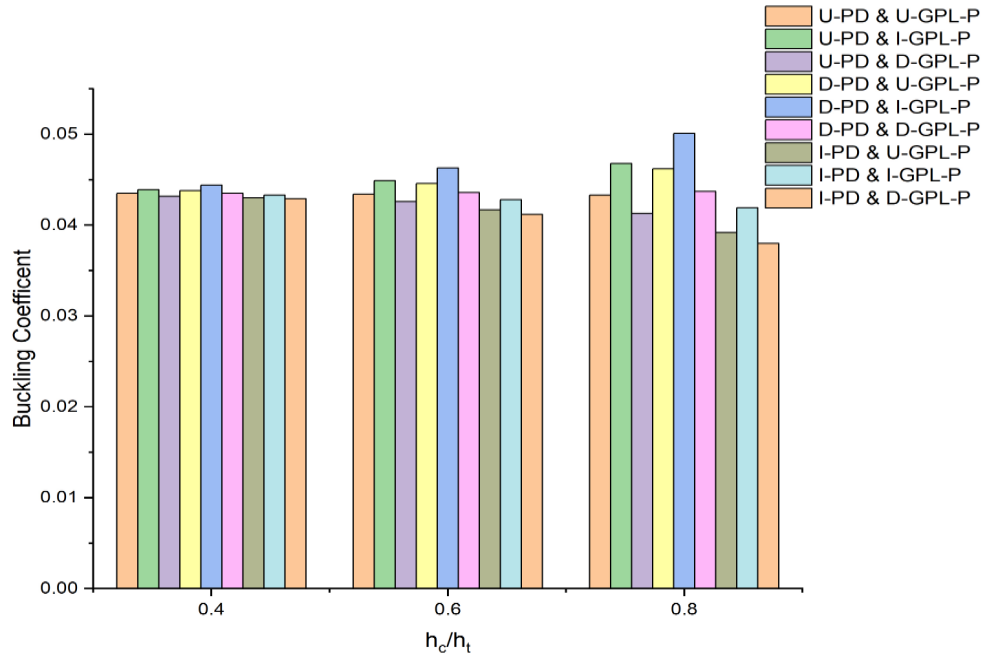


Figure 4.4: Variation in buckling coefficient value with core to total thickness ($\frac{h_c}{h_t}$) of GPL reinforced porous sandwich cylindrical panel subjected to uniform edge load under SSSS boundary condition ($\frac{a}{b} = 1$, $e_o = 0.4$, $\Lambda_{GPL} = 1wt\%$, $\frac{R}{a} = 20$)

loading condition is presented in Figure 4.4. It is observed that increase in core to total thickness ratio has a positive effect on certain combinations of GPL and porosity distribution. For instance, with increase in core to total thickness ratio the presence of decreasing porosity distribution (D-PD) in a sandwich cylindrical panel enhances the buckling coefficient value irrespective of GPL pattern. This is due to the high influence of D-PD porosity pattern in enhancing the stiffness with increase in core to total thickness ratio. Similarly, an enhancement in buckling coefficient value is observed for the core with U-PD porosity pattern and I-GPL-P pattern of GPL with increase in core to total thickness ratio. It can be attributed as the influence of increased distribution of GPL towards top and bottom side and high GPL content. Moreover, it is also observed that buckling coefficient value decreases for all other combinations of porosity pattern and GPL distribution. This is due to decrease in stiffness with increase in size of the core. Further, highest buckling coefficient value is observed for the core with D-PD porosity

pattern and I-GPL-P pattern of GPL for the core to total thickness ratio ($\frac{h_c}{h_t}$) of 0.8. This is expected as both D-PD and I-GPL-P patterns increases the structural stiffness of the cylindrical panel and so does the buckling coefficient value. Highest buckling coefficient value among different type of loading is observed for uniform loading and lowest value is observed for partial tension loading as expected.

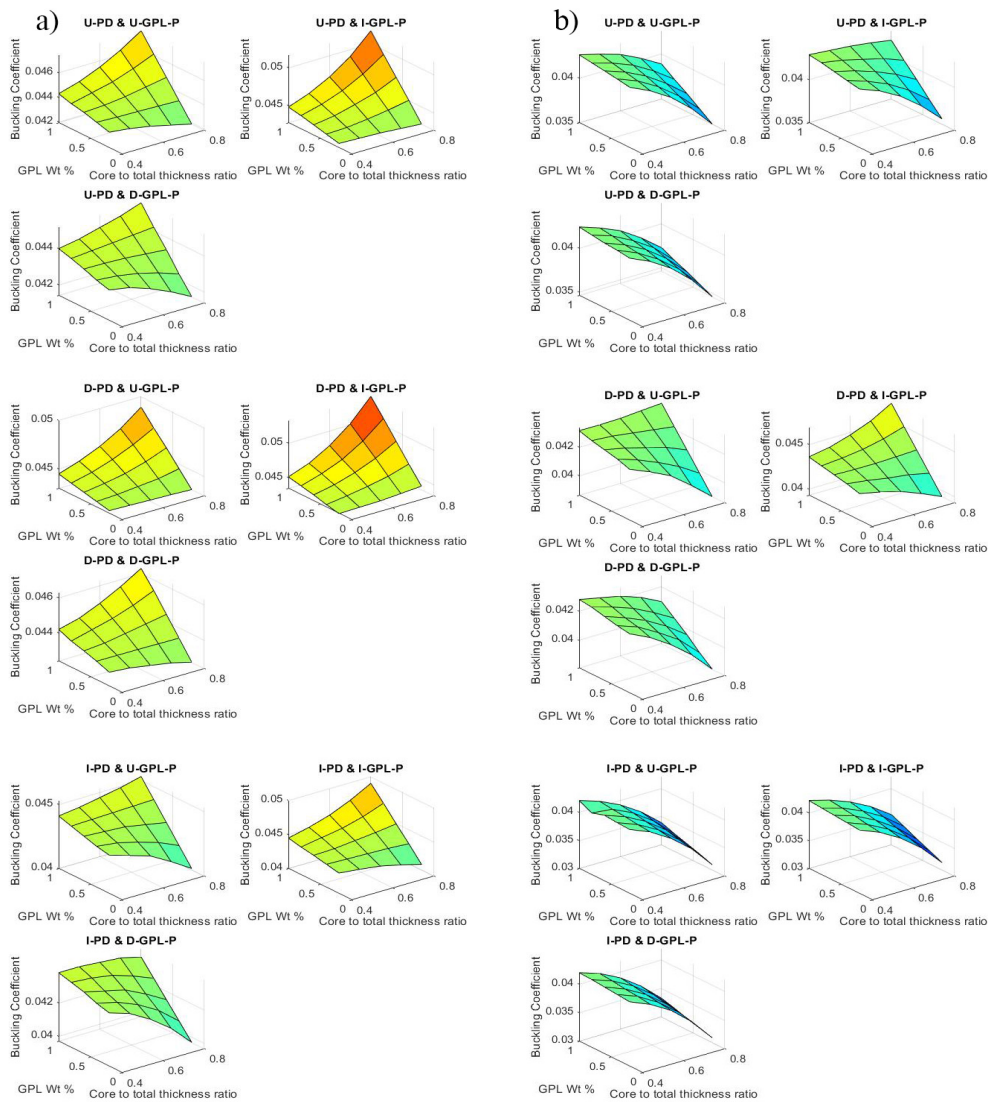


Figure 4.5: 3D surface plots of buckling coefficient of sandwich cylindrical panel indicating the effect of GPL weight fraction and core to total thickness ratio under uniform loading (Case-a) (a)porosity coefficient(e_0)=0.2 (b)porosity coefficient(e_0)=0.6

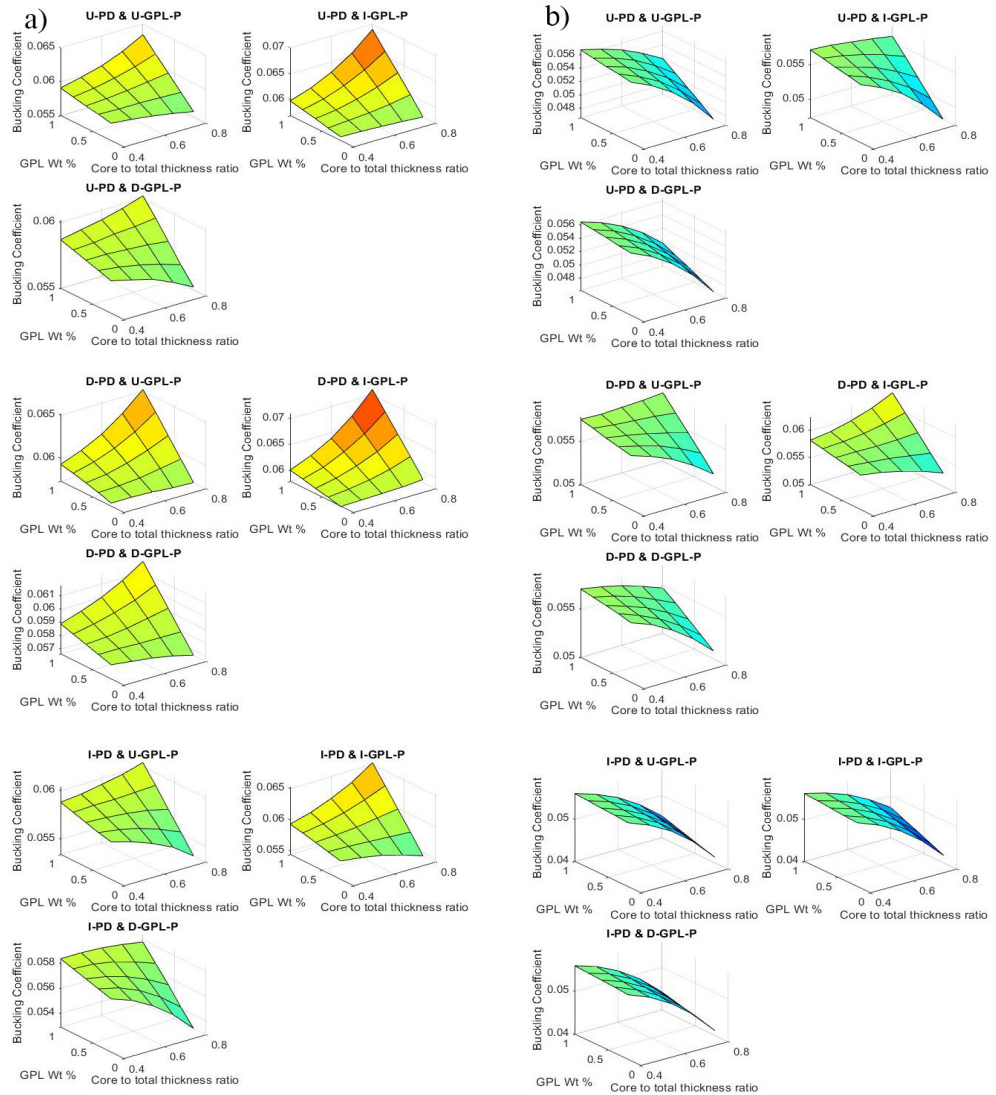


Figure 4.6: 3D surface plots of buckling coefficient of sandwich cylindrical panel indicating the effect of GPL weight fraction and core to total thickness ratio under trapezoidal loading (Case-b) (a)porosity coefficient(e_0)=0.2 (b)porosity coefficient(e_0)=0.6

To study the synergistic influence of GPL weight fraction and core to total thickness ratio ($\frac{h_c}{h_t}$) on the buckling response of porous GPL core sandwich cylindrical panel, 3D surface plots are presented in Figures 4.5, 4.6, 4.7. These figures show the transition of buckling coefficient value with GPL weight fraction and core to total thickness ratio for uniform, trapezoidal and parabolic respectively. In these figures, Sub-figure (a) and

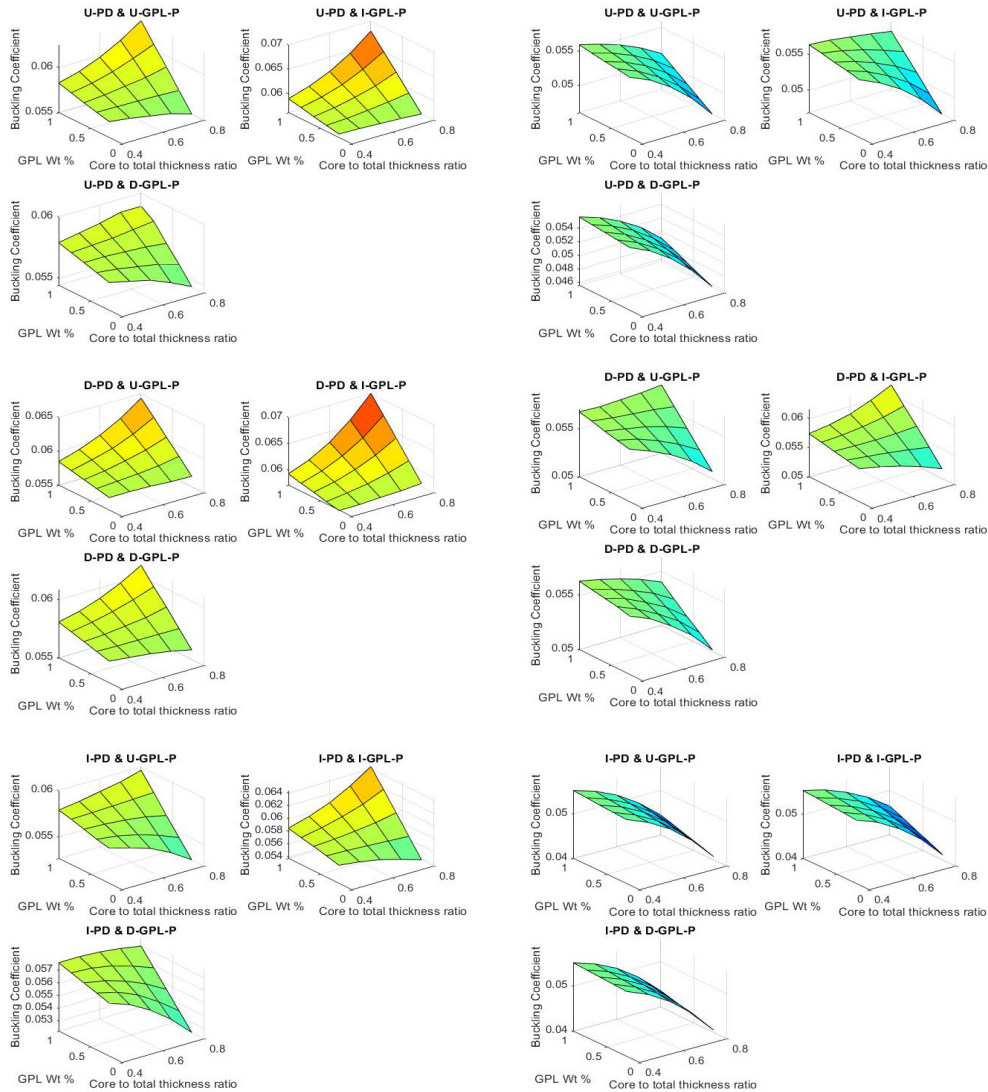


Figure 4.7: 3D surface plots of buckling coefficient of sandwich cylindrical panel indicating the effect of GPL weight fraction and core to total thickness ratio under parabolic loading (Case-e) (a) porosity coefficient(e_0)=0.2 (b) porosity coefficient(e_0)=0.6

(b) corresponds to two different porosity coefficient value given as (a) $e_0 = 0.2$, (b) $e_0 = 0.6$. By careful examination of Sub figures 4.5(a), 4.6(a), 4.7(a), it is inferred that at high values of GPL the increase in core to total thickness ratio have a positive impact on the buckling coefficient value. This is expected as the presence of high amount of GPL enhances the stiffness of the sandwich cylindrical panel. On the other hand, at

low GPL content the increase in core to total thickness ratio has a negative impact on the buckling coefficient value for most of the cases. This is due to reduction in stiffness with increase in core to total thickness ratio. Accordingly, one can observe by analyzing Sub-figures 4.5(b), 4.6(b), 4.7(b) (porosity coefficient $e_0 = 0.6$) that even when high GPL content is present, increase in core thickness reduces the buckling coefficient value for most of the cases. This can be explained as the stiffness of the sandwich is governed by porosity of the core over GPL content. The only exceptions are D-PD & U-GPL-P and D-PD & I-GPL-P for which at high GPL content, stiffness of porous sandwich cylindrical panel is governed by GPL content instead of porosity. This is due to the presence of efficient D-PD porosity distribution in common.

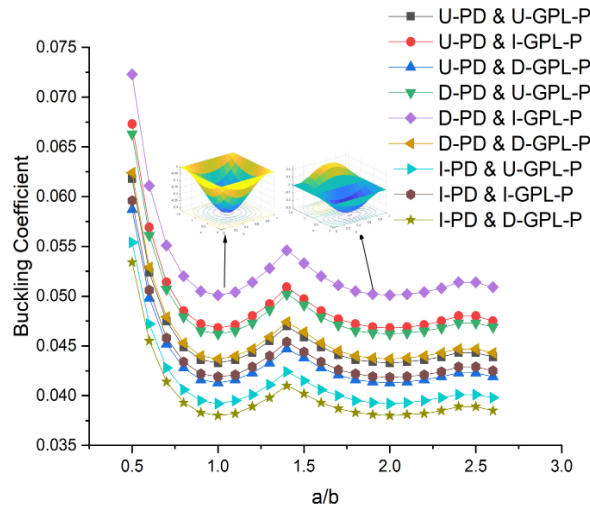


Figure 4.8: Variation of buckling coefficient of GPL reinforced sandwich panel under SSSS boundary condition subject to uniform edge loading ($e_0 = 0.4$, $\Lambda_{GPL} = 1wt\%$, $\frac{h_c}{h_t} = 0.8$ and $\frac{R}{a} = 20$): effect of aspect ratio

Next, the buckling coefficient of porous GPL core sandwich cylindrical panel under uniform load with respect to aspect ratio ($\frac{a}{b}$) is illustrated in Figure 4.8. It is observed that buckling coefficient value decreases considerably with increase in aspect ratio upto 1, afterwards an increase in value is observed till $\frac{a}{b} = 1.4$. Beyond $\frac{a}{b} = 1.4$, buckling coefficient value again decreases and so on. Accordingly, the buckling mode shape changes

from (1,1) to (2,1) as shown in Figure 4.8. This is due to variation in structural stiffness and pre-stress developed due to the applied load with increase in aspect ratio. Moreover, similar kind of variation in buckling coefficient is observed for the core with other types of distributions also. Since there is no change in buckling coefficient with variation in aspect ratio for different porosity pattern and GPL distribution combinations, the same analysis is not presented for other type of loadings. Figure 4.8, also reveals that sandwich having a core with D-PD porosity variation and I-GPL-P pattern of GPL distribution has the maximum buckling coefficient value while the sandwich having a core with I-PD porosity variation and D-GPL-P pattern of GPL distribution has the lowest buckling coefficient as already explained.

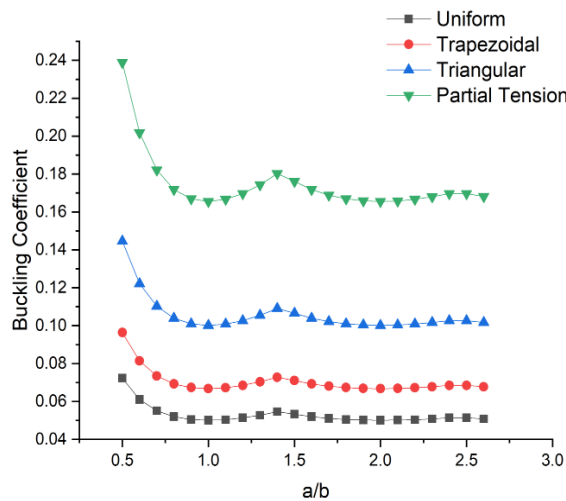


Figure 4.9: Variation of buckling coefficient of D-PD & I-GPL-P sandwich panel under SSSS boundary condition subject to uniform, NEL-I ($e_o = 0.4$, $\Lambda_{GPL} = 1wt\%$, $\frac{h_c}{h_t} = 0.8$ and $\frac{R}{a} = 20$): effect of aspect ratio

Variation of buckling coefficient value of D-PD & I-GPL-P sandwich cylindrical panel subjected to different type I non-uniform edge loading with respect to aspect ratio ($\frac{a}{b}$) is shown in Figure 4.9. Similar to the uniform loading, the shifting of buckling mode shape from (1,1) to (2,1) happens at $\frac{a}{b} = 1.4$. This can be explained as equal influence of the linear loads to change the buckling mode shape. Furthermore, Figure 4.9 shows

that the highest buckling coefficient value is for partial tension loading and lowest is for uniform loading as already established in earlier discussions.

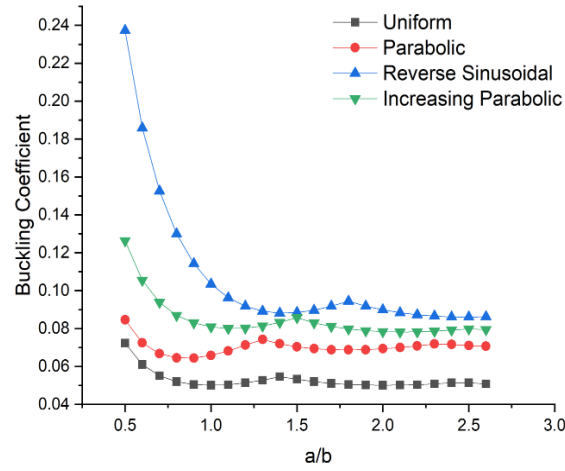


Figure 4.10: Variation of buckling coefficient of D-PD & I-GPL-P sandwich panel under SSSS boundary condition subject to uniform, NEL-II ($e_o = 0.4$, $\Lambda_{GPL} = 1wt\%$, $\frac{h_c}{h_t} = 0.8$ and $\frac{R}{a} = 20$): effect of aspect ratio

Figure 4.10 demonstrates the variation of buckling coefficient value of D-PD & I-GPL-P core sandwich cylindrical panel subjected to different type II non-uniform edge loadings with respect to aspect ratio ($\frac{a}{b}$). The displayed results reveal that mode shifting from (1,1) to (2,1) occurs at different $\frac{a}{b}$ ratio when the load variation is not linear. The buckling mode shifts from (1,1) to (2,1) at $\frac{a}{b} = 1.2$ for parabolic loading case, $\frac{a}{b} = 1.4$ for increasing parabolic loading and $\frac{a}{b} = 1.7$ for reverse sinusoidal loading. This is due to the influence of different in-plane stress distributions in the case of non linear edge loadings. However, the buckling mode shape under the different load cases in which the load variation is not linear is same for $\frac{a}{b} = 1.2$, it is (1,1) mode as shown in Figure 4.11. Accordingly, one can observe that at $\frac{a}{b} = 1.6$ the buckling mode shape for all cases except reverse sinusoidal loading is (2,1) (double half wave) and for reverse sinusoidal loading it is (1,1) (half wave) as depicted in Figure 4.12.

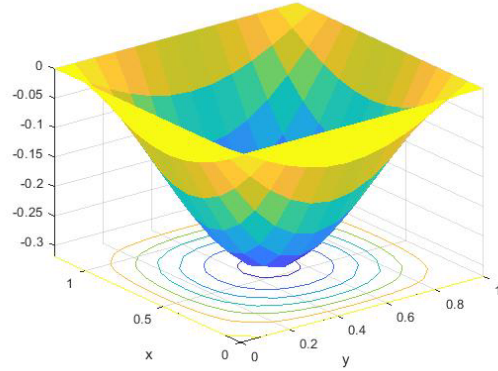


Figure 4.11: Buckling mode of D-PD & I-GPL-P sandwich panel for aspect ratio $a/b=1.2$ for uniform and different edge loads (Parabolic, Reverse Sinusoidal, Increasing Parabolic.)

Before closing this section, it has been demonstrated that increase in core to total thickness ratio has a positive impact on buckling response of sandwich cylindrical panel for some cases of porosity distribution and GPL patterns. The increase in core to total thickness ratio would actually lower the total weight of the sandwich panel with an added benefit of increased buckling capacity. Thus, D-PD & I-GPL-P core sandwich panel with a high core to total thickness ratio can improve the buckling performance of sandwich cylindrical panel. Moreover, it has been established that changes in buckling mode shape occurs at different $\frac{a}{b}$ ratio for different type of type II non-uniform edge loading conditions. The question that arise now is the free vibration response of GPL reinforced porous sandwich panel and will be discussed in the following section.

4.4.2 Free Vibration Studies

Free vibration results of porous FG-GPL core cylindrical panel under different non-uniform edge loadings is presented in this section. The geometric properties used are same as that considered in Section 4.4.1. Two different boundary conditions are used to study the influence of boundary conditions on the free vibration frequencies of sandwich cylindrical panel. Simply supported (SSSS) and fully clamped (CCCC) are the

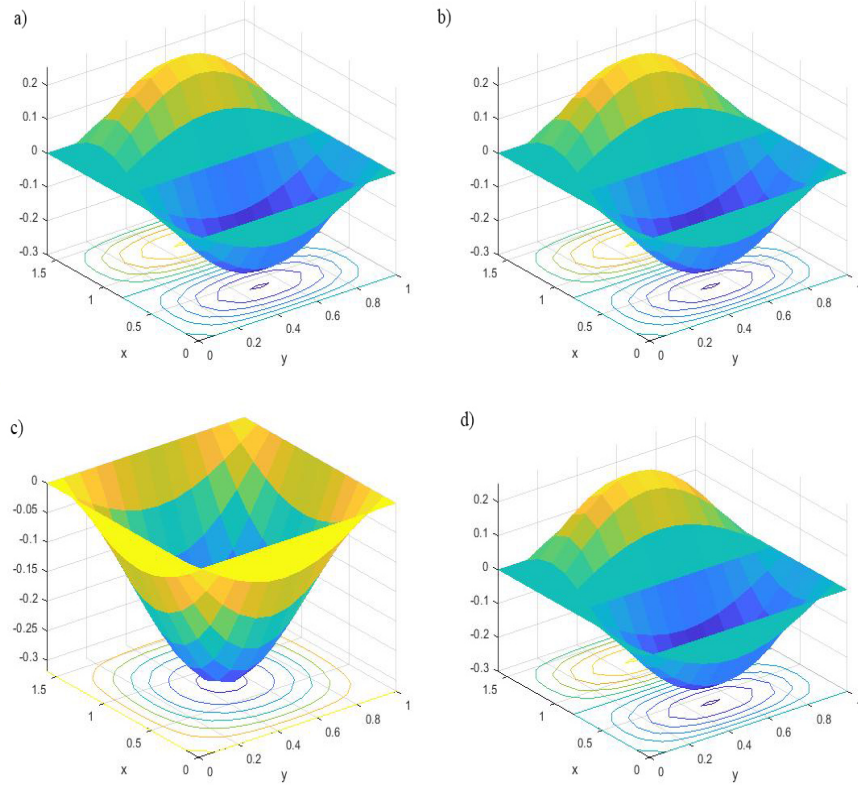


Figure 4.12: Buckling mode of D-PD & I-GPL-P sandwich panel for aspect ratio $a/b=1.6$ for (a) Uniform (b) Parabolic (c) Reverse Sinusoidal (d) Increasing Parabolic.

two different boundary conditions considered. For convenience purposes, the natural frequency is expressed as non-dimensional frequency given as: $\Omega = \omega_n \left(\frac{a^2}{h} \sqrt{\frac{\rho_m}{E_m}} \right)$

In Table 4.6, the non-dimensional fundamental frequency of GPL reinforced porous sandwich cylindrical panel with different boundary conditions with respect to radius ratio is presented. It is observed that the non-dimensional frequency reduces with increase in radius ratio. This is expected as increase in radius ratio decreases the structural stiffness and so does the natural frequency. The non-dimensional natural frequency tends to vary with different porosity and GPL distributions. The highest natural frequency value is observed for D-PD & I-GPL-P core sandwich cylindrical panel and lowest for I-PD & D-GPL-P core sandwich cylindrical panel. This can be explained by considering low

Table 4.6: Non-dimensional fundamental frequency of GPL reinforced porous sandwich cylindrical under different boundary condition($\frac{a}{b} = 1$, $e_o = 0.4$, $\Lambda_{GPL} = 1wt\%$, $\frac{h_c}{h_t}=0.8$) : variation with radius ratio ($\frac{R}{a}$)

GPL	Porosity	SSSS			CCCC		
		$\frac{R}{a}$			$\frac{R}{a}$		
		5	10	20	5	10	20
U-GPL-P		12.4263	8.3578	6.9752	16.5264	13.1421	12.1469
I-GPL-P	U-PD	12.5837	8.5904	7.2524	16.9198	13.6347	12.6786
D-GPL-P		12.3357	8.2220	6.8119	16.2973	12.8522	11.8325
U-GPL-P		12.5770	8.5558	7.2041	16.8675	13.5507	12.5831
I-GPL-P	D-PD	12.8064	8.8263	7.5046	17.3416	14.0903	13.1499
D-GPL-P		12.4295	8.3799	7.0069	16.5596	13.1970	12.2099
U-GPL-P		12.3160	8.1020	6.6387	16.1168	12.5524	11.4869
I-GPL-P	I-PD	12.3268	8.2490	6.8565	16.3332	12.9284	11.9236
D-GPL-P		12.3106	8.0319	6.5338	16.0136	12.3716	11.2759

porosity and increased GPL content towards top and bottom surfaces for D-GPL-P and high porosity and reduced GPL content towards top and bottom surfaces for I-PD & D-GPL-P sandwich cylindrical panel. Moreover, it is observed that there is an enhancement in non-dimensional frequency with respect to boundary conditions for all type of sandwich cylindrical panels.

Next, the influence of core to total thickness ratio ($\frac{h_c}{h_t}$) on the non-dimensional frequency of porous GPL core sandwich cylindrical panel is presented in Table 4.7. It is observed that the non-dimensional frequency increases with increase in $\frac{h_c}{h_t}$ ratio for most of the cases. This can be explained by the combined effect of increase in structural stiffness due to GPL addition and reduction in mass due to presence of porosity. The only two sandwich panels for which increase in $\frac{h_c}{h_t}$ ratio has a negative effect are I-PD & U-GPL-P core and I-PD & D-GPL-P core sandwich panels. This is because of the inability of GPL reinforcement in uniform and decreasing pattern to improve stiffness for these two cases. The highest natural frequency value is observed for D-PD & I-GPL-P core panel and lowest for I-PD & D-GPL-P core panel at $\frac{h_c}{h_t}=0.8$. This is expected as D-PD & I-GPL-P core sandwich cylindrical panel can impart higher stiffness with increase in core to total thickness ratio while the inverse is applicable for I-PD & D-GPL-P core sandwich panel.

Table 4.7: Non-dimensional frequency of GPL reinforced porous sandwich cylindrical under different boundary condition ($\frac{a}{b} = 1, e_o = 0.4, \Lambda_{GPL} = 1wt\%, \frac{R}{a} = 20$: variation with core to total thickness ratio ($\frac{h_c}{h_t}$)

GPL	Porosity	SSSS			CCCC		
		$\frac{h_c}{h_t}$			$\frac{h_c}{h_t}$		
		0.4	0.6	0.8	0.4	0.6	0.8
U-GPL-P	U-PD	6.7583	6.8660	6.9752	11.7700	11.9574	12.1469
I-GPL-P		6.7923	6.9821	7.2524	11.8354	12.1804	12.6786
D-GPL-P		6.7388	6.7988	6.8119	11.7326	11.8283	11.8325
U-GPL-P	D-PD	6.7874	6.9627	7.2041	11.8245	12.1409	12.5831
I-GPL-P		6.8278	7.0930	7.5046	11.8981	12.3848	13.1499
D-GPL-P		6.7617	6.8787	7.0069	11.7777	11.9836	12.2099
U-GPL-P	I-PD	6.7211	6.7309	6.6387	11.6932	11.6893	11.4869
I-GPL-P		6.7420	6.8151	6.8565	11.7410	11.8633	11.9236
D-GPL-P		6.7113	6.6909	6.5338	11.6707	11.6066	11.2759

Variation in the non-dimensional frequency with increase in both GPL weight fraction and core to total thickness ratio ($\frac{h_c}{h_t}$) is shown in Figure 4.13. 3D surface plots are presented for better understanding with sub figures (a) and (b) denoting $e_0 = 0.2$ and $e_0 = 0.6$ respectively. In Figure 4.13, sub figure (a) reveal that at high GPL content increase in $\frac{h_c}{h_t}$ ratio leads to elevated non-dimensional frequency value for all the different sandwich panels. This is explained as the influence of GPL to improve the sandwich panel stiffness at low porosity level. Moreover, for the lower GPL content, the nature of porosity distribution has the higher influence and sandwich panels with three porosity distributions show significantly different response. For instance, the sandwich cylindrical panel with decreasing porosity distribution (D-PD) shows an increasing frequency value whereas, I-PD sandwich panel shows a decreasing nature of frequency. However, not much change is observed for uniform porosity distribution. This is due to higher influence of porosity pattern in the presence of low GPL content. Further, consideration of sub figure (b) shows that at low GPL content, the non-dimensional frequency reduces with increase in core thickness for all the type of distributions. This is because of the reduction in the sandwich panel stiffness due to the presence of high amount of porosity. Accordingly, for high GPL content increase in frequency is observed for the core with some combinations of porosity and GPL distributions. Interestingly, it is also

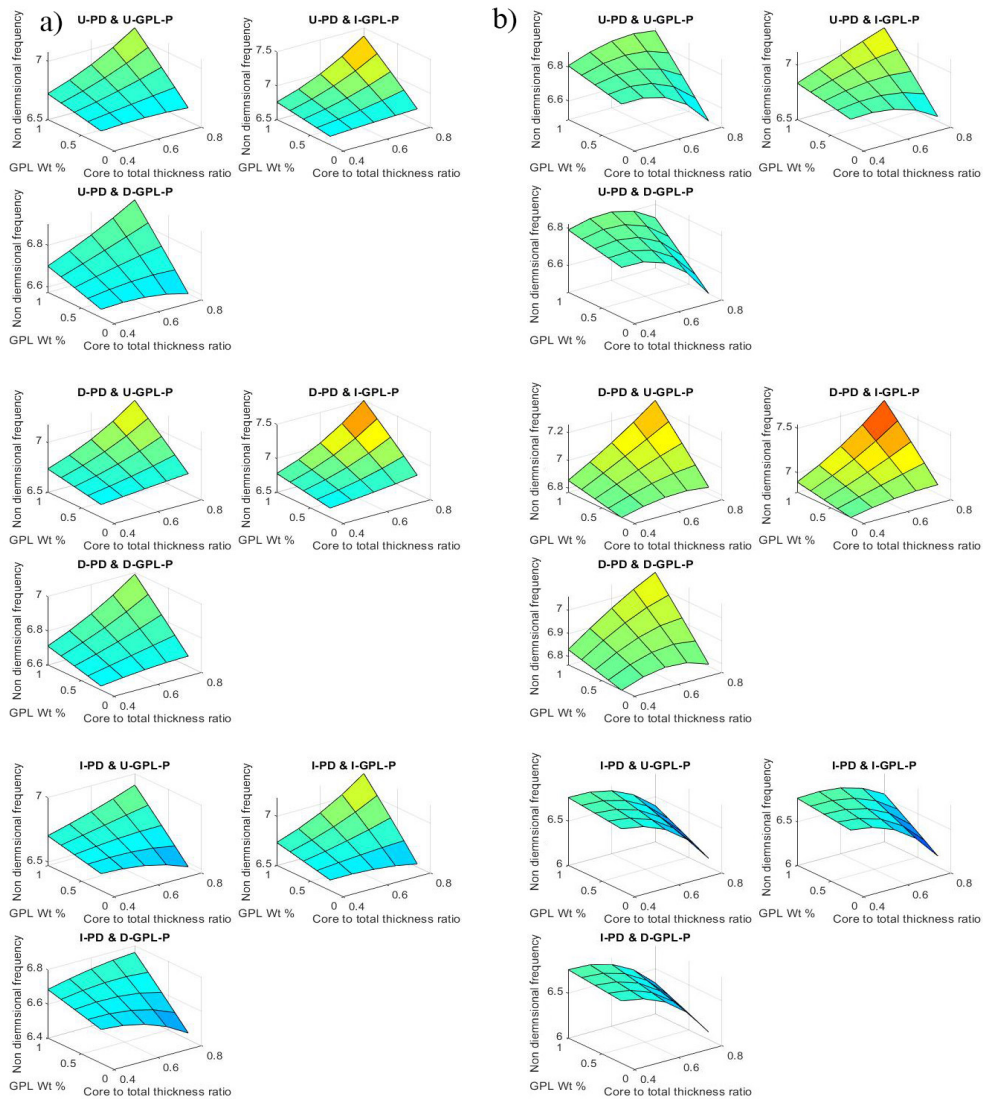


Figure 4.13: 3D surface plots of non dimensional frequency of sandwich cylindrical panel indicating the effect of GPL weight fraction and core to total thickness ratio under uniform loading (a)porosity coefficient(e_0)=0.2 (b)porosity coefficient(e_0)=0.6

observed that sandwich panel with decreasing porosity shows an increase in frequency even at high porosity. This is because of the influence of D-PD porosity variation in improving stiffness and high GPL content. U-PD & I-GPL-P core sandwich panel shows an increasing buckling coefficient value with increase in $\frac{h_c}{h_t}$ ratio at high GPL content. This can be attributed to the influence of high GPL content in improving stiffness.

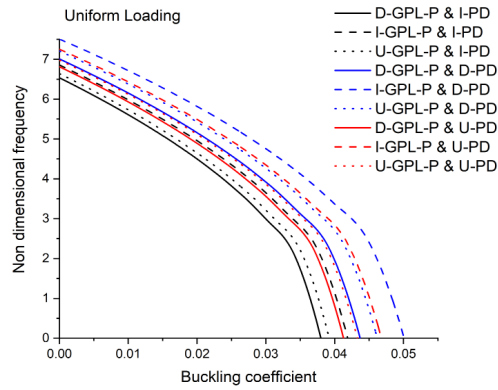


Figure 4.14: Variation of non-dimensional frequency with uniform compressive load for GPL reinforced porous sandwich cylindrical panel under SSSS boundary condition

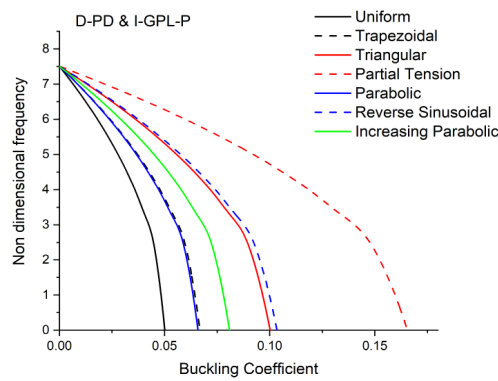


Figure 4.15: Variation of non-dimensional frequency with compressive load of D-PD & I-GPL-P sandwich panel under SSSS boundary condition subject to uniform, linearly and non-linearly varying in-plane compressive loads.

To demonstrate the influence of gradually applied compressive load on the fundamental non-dimensional frequency of GPL reinforced porous sandwich cylindrical panel, Figures 4.14 and 4.15 are plotted. Figure 4.14 shows the variation of the non-dimensional frequency of a GPL reinforced porous cylindrical panel with increase in UEL. The magnitude of UEL is increased in small steps of critical buckling load ($0.1\bar{N}_0$, $0.2\bar{N}_0$, $0.3\bar{N}_0$,..... $1\bar{N}_0$) and corresponding variation in natural frequency is plotted. The displayed results reveal that natural frequency reduces with increase in compressive load for all the different GPL and porosity combinations and follows a similar reduc-

tion path. The highest value of non-dimensional frequency and buckling coefficient is observed for D-PD & I-GPL-P core sandwich panel and lowest for I-PD & D-GPL-P core sandwich panel. Further, Figure 4.15 shows the reduction in fundamental natural frequency of D-PD & I-GPL-P core sandwich cylindrical panel under different in-plane loads. Interestingly, the natural frequency reaches to zero when applied load is equal to the critical buckling load. More interestingly, the intensity of load required to reduce non-dimensional natural frequency to a minimum value is different for different edge loads. This is expected as increase in magnitude of the compressive loading reduces the transverse stiffness of the structure and thus highly dependent on the distribution of compressive load. For uniform loading, very small amount of compressive load is required to reduce the frequency to a minimum value. Compared to linear loading, non-linearly varying compressive load seems to be effective as non-linearly varying loading induces stress resultants in more than one direction which has a clear influence on stiffness reduction. The free vibration mode shape remains same as (1,1) with increase in edge load for all the loading conditions.

4.5 Closure

The buckling and free vibration response of GPL reinforced porous sandwich cylindrical panel subjected to different type of NELs was investigated. Different combinations of porosity and GPL distributions for the sandwich core are considered. The Eigen value problems of buckling and free vibration are obtained by utilizing a higher order shear deformation theory and semi analytical method. The influence of different distributions of GPL and porosity, core to total thickness ratio, radius of curvature, GPL weight fraction, porosity coefficient on buckling and free vibration under uniform, NEL-I, NEL-II is analyzed. From the parametric study, it is found that the sandwich cylindrical panel with D-PD & I-GPL-P core has the maximum buckling resistance and better free vibration frequency while the panel with I-PD & D-GPL-P core has the minimum. The

critical buckling load is largely influenced by the type of NEL and uniform loading has the minimum value while partial tension loading possesses the maximum. The enhancement in buckling resistance and free vibration frequency with core to total thickness ratio depends on the amount of porosity in the core. In sandwich cylindrical panels with low porosity coefficient, in the presence of high GPL content the buckling coefficient and free vibration frequency increases with rise in core to total thickness ratio. In sandwich cylindrical panels with high porosity coefficient, in the presence of high GPL content the variation of buckling coefficient and free vibration frequency depending on porosity distribution and GPL pattern. The shifting of mode shape associated with critical buckling load from (1,1)(single half wave) to (2,1) (double half wave) occurs for different values of aspect ratio for different types of non-uniform edge loads. The reduction of natural frequency with compressive load depends on the type of non-uniform edge load. The low magnitude of edge load to reduce the natural frequency to minimum is observed for uniform load while, large magnitude is required for partial tension loading.

CHAPTER 5

FREE VIBRATION-BUCKLING ANALYSIS ON CNT REINFORCED CYLINDRICAL PANEL

5.1 Introduction

In the present chapter, buckling and free vibration behaviour of agglomerated CNT reinforced nano cylindrical panel under the influence of NELs considering the non-local effect has been investigated. The presence of nano reinforcements in these nano scaled structures helps in improvement of stiffness, however, consideration of size effects is important to predict the results accurately. Further, the consideration of CNT agglomeration is important for predicting the buckling and free vibration characteristics of structures under practical conditions. Therefore, critical buckling load and free vibration frequencies of agglomerated CNTs reinforced cylindrical shell panel subjected to different kinds of NELs considering the size effect are investigated.

5.2 Non-Local Elasticity Modelling of CNT Reinforced Cylindrical Panel

5.2.1 Mathematical Material Modelling

This section presents the constitutive equations for cylindrical panels reinforced with CNTs considering its agglomeration effect as well as size effect. The effective mechanical properties of cylindrical panels can be obtained by direct method if the CNTs are dispersed uniformly throughout the matrix. However, CNTs are often not uniformly

distributed and tend to bundle together due to Van-der-Waals forces, high aspect ratio, and low bending stiffness. The effective material properties of CNT reinforced composites are given in Shi *et al.* (2004) using a two-parameter micromechanics model. The non-uniform distribution of CNTs in the matrix leads to the formation of spherical bundles with different elastic properties of the surrounding material as shown in Figure 5.1.

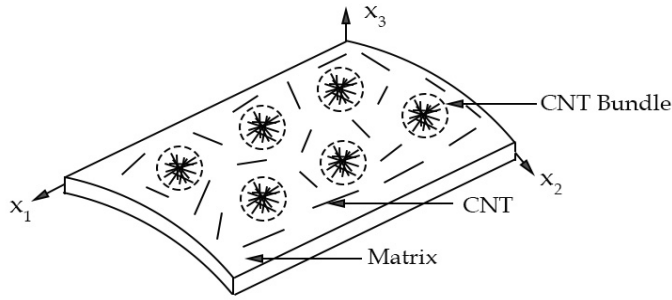


Figure 5.1: CNT bundling model with agglomeration

The total volume of CNTs (V_r^{CNT}) in the RVE (representative volume element) is given by:

$$V_r^{CNT} = V_r^m + V_r^{bundle} \quad (5.1)$$

where, V_r^{bundle} and V_r^m represents the volume of CNTs inside the bundle and matrix respectively. The agglomeration phenomenon is represented by two parameters as follows:

$$\epsilon = \frac{V_{bundle}}{V} \quad \text{and} \quad \eta = \frac{V_r^{bundle}}{V_r^{CNT}} \quad (5.2)$$

where, V_{bundle} , V represents the volume of bundles in the RVE and total volume of RVE respectively. The parameters ϵ represents the volume fraction of bundles to the total volume of the RVE and η represents the volume ratio of CNTs present in the bundle to the total volume of CNTs in the RVE. In Equation 5.2, $\epsilon = 1$ denotes uniform distribution of CNTs in the matrix and decrease in ϵ value denotes increase in

agglomeration degree. When $\eta = 1$, all the CNTs are dispersed in inclusions and the case of $\epsilon = \eta$ denotes CNTs are uniformly dispersed in the cylindrical panel.

The ratio of volume of CNTs to the total volume is given as average volume fraction (r_v) as:

$$r_v = \frac{V_r^{CNT}}{V} \quad (5.3)$$

The effective shear modulus (G_{out}) and bulk modulus (K_{out}) outside the bundles, and the effective shear modulus (G_{in}) and bulk modulus (K_{in}) of the bundles are given as (Shi *et al.* 2004):

$$G_{out} = G_m + \frac{r_v(\eta_r - 2G_m\beta_r)(1-\eta)}{2[1-\epsilon - r_v(1-\eta) + r_v(1-\eta)\beta_r]} \quad (5.4a)$$

$$K_{out} = K_m + \frac{r_v(\delta_r - 3K_m\alpha_r)(1-\eta)}{3[1-\epsilon - r_v(1-\eta) + r_v(1-\eta)\alpha_r]} \quad (5.4b)$$

$$G_{in} = G_m + \frac{r_v(\eta_r - 2G_m\beta_r)\eta}{2[\epsilon - r_v\eta + r_v\eta\beta_r]} \quad (5.4c)$$

$$K_{in} = K_m + \frac{r_v(\delta_r - 3K_m\alpha_r)\eta}{3[\epsilon - r_v\eta + r_v\eta\alpha_r]} \quad (5.4d)$$

where,

$$G_m = \frac{E_m}{2(1+\nu_m)} \quad (5.5a)$$

$$\eta_r = \frac{1}{5} \left[\frac{2}{3}(n_r - l_r) + \frac{8G_m p_r}{G_m + p_r} + \frac{8m_r G_m (3K_m + 4G_m)}{3K_m(m_r + G_m) + G_m(7m_r + G_m)} + \frac{2(k_r - l_r)(2G_m + l_r)}{3(G_m + k_r)} \right] \quad (5.5b)$$

$$\beta_r = \frac{1}{5} \left[\frac{4G_m + 2k_r + l_r}{3(G_m + k_r)} + \frac{4G_m}{G_m + p_r} + \frac{2[G_m(3K_m + G_m) + G_m(3K_m + 7G_m)]}{G_m(3K_m + G_m) + m_r(3K_m + 7G_m)} \right] \quad (5.5c)$$

$$K_m = \frac{E_m}{3(1-2\nu_m)} \quad (5.5d)$$

$$\delta_r = \frac{1}{3} \left[n_r + 2l_r + \frac{(2k_r + l_r)(3K_m + 2G_m - l_r)}{G_m + k_r} \right] \quad (5.5e)$$

$$\alpha_r = \frac{3(K_m + G_m) + k_r - l_r}{3(G_m + k_r)} \quad (5.5f)$$

Here, k_r, l_r, m_r, n_r and p_r denotes Hill's Elastic moduli (Hill 1965) for the CNT reinforcement and G_m, E_m, ν_m and K_m represents the shear modulus, Young's modulus, Poisson's ratio and the bulk modulus of the matrix phase.

The Mori-Tanaka model is used to calculate the effective material properties as:

$$K = K_{out} \left[1 + \frac{\epsilon \left(\frac{K_{in}}{K_{out}} - 1 \right)}{1 + \alpha_c (1 - \epsilon) \left(\frac{K_{in}}{K_{out}} - 1 \right)} \right] \quad (5.6a)$$

$$G = G_{out} \left[1 + \frac{\epsilon \left(\frac{G_{in}}{G_{out}} - 1 \right)}{1 + \beta_c (1 - \epsilon) \left(\frac{G_{in}}{G_{out}} - 1 \right)} \right] \quad (5.6b)$$

$$E = \frac{9KG}{3K+G} \quad (5.6c)$$

$$\nu = \frac{3K-2G}{6K+2G} \quad (5.6d)$$

where,

$$\alpha_c = \frac{1 + \nu_{out}}{3(1 - \nu_{out})} \quad (5.7a)$$

$$\beta_c = \frac{8 - 10\nu_{out}}{15(1 - \nu_{out})} \quad (5.7b)$$

and

$$\nu_{out} = \frac{3K_{out} - 2G_{out}}{6K_{out} + 2G_{out}} \quad (5.8)$$

The variation in material properties K_{in}, K_{out}, K and G_{in}, G_{out}, G with variation in agglomeration parameter η for partially agglomerated condition ($\epsilon = 0.5$) is given in Figure 5.2. It is observed that with increase in amount of CNTs inside bundle (increase in η) leads to reduction in both effective bulk modulus (K) and shear modulus (G) of

cylindrical panel.

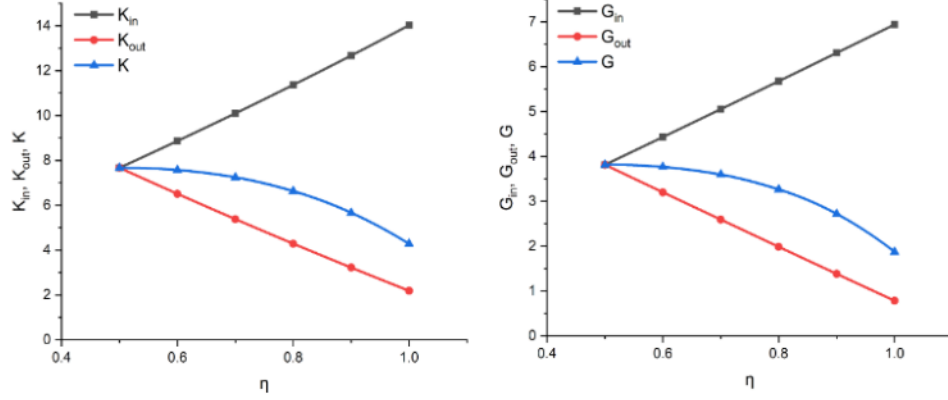


Figure 5.2: The variation of material properties of a partially agglomerated ($\epsilon = 0.5$) CNT reinforced cylindrical panel with increase in agglomeration parameter η .

5.2.2 Nonlocal Elasticity Theory

When CNTs are dispersed uniformly in the matrix, the resulting composite panel is considered as an isotropic material. However, at the scale of the intrinsic characteristic length, the microstructural heterogeneity is present. Thus, non-local elasticity theory (Eringen 1972, 1983, 2002) is applied which suggests the stress at a reference point is dependent on the point and all other parts in the domain.

The constitutive equations for non-local elasticity (Eringen 1972) based on gradient model is given as:

$$\sigma^l = \sigma^{nl} - \mu^2 \nabla^2 \sigma^{nl} \quad (5.9)$$

where, σ^l and σ^{nl} denotes non-local and local stress respectively and ∇ is the Laplacian operator given as $\nabla^2 = \frac{\partial^2}{\partial x^2} + \frac{\partial^2}{\partial y^2}$ and non-local parameter is given by μ . The non-local parameter estimation using experiments for structures reinforced with CNTs is not carried out yet (Hu *et al.* 2008), hence the present analysis is carried out with assumed values. However, some experimental studies for estimating the length scale

parameter using various non local theories are available in the open literature (Lei *et al.* 2016; Li *et al.* 2019c; Xie *et al.* 2022). The general approach for estimation of non-local parameter is by minimisation of least square error between experimental and theoretical results (Lei *et al.* 2016).

The stress-strain relations considering non-local effect is given as:

$$(1 - \mu^2 \nabla^2) \begin{Bmatrix} \sigma_{xx} \\ \sigma_{yy} \\ \tau_{xy} \\ \tau_{xz} \\ \tau_{yz} \end{Bmatrix} = \begin{bmatrix} Q_{11} & Q_{12} & 0 & 0 & 0 \\ Q_{12} & Q_{22} & 0 & 0 & 0 \\ 0 & 0 & Q_{66} & 0 & 0 \\ 0 & 0 & 0 & Q_{55} & 0 \\ 0 & 0 & 0 & 0 & Q_{44} \end{bmatrix} \begin{Bmatrix} \epsilon_{xx} \\ \epsilon_{yy} \\ \gamma_{xy} \\ \gamma_{xz} \\ \gamma_{yz} \end{Bmatrix} \quad (5.10)$$

Q_{ij} are stiffness matrix coefficients and defined as follows:

$$\begin{aligned} Q_{11} &= Q_{22} = \frac{E}{1-\nu^2} \\ Q_{12} &= Q_{21} = \frac{E\nu}{1-\nu^2} \\ Q_{66} &= Q_{55} = Q_{44} = G \end{aligned} \quad (5.11)$$

Using non-local elasticity theory the stress-strain relations are considered by incorporating the non-local parameter as discussed in this section. Using these equations, the governing differential equations are formulated and buckling and free vibration parameters are calculated as discussed in Section 2.

5.3 Validation

In this section, the comparison of effective material properties, buckling and free vibration results of agglomerated CNTs reinforced cylindrical panel obtained using the present method with the results available in literature is presented.

5.3.1 Verification of Material Properties Estimation

Firstly, the effective Young's modulus reported by Bisheh *et al.* (2020) is compared to verify the correctness of micro mechanics model followed in the present work. Bisheh *et al.* (2020) also used Mori-Tanaka micro-mechanics model to evaluate the effective Young's modulus. The matrix and CNT properties as given in Bisheh *et al.* (2020) are adopted. For the matrix : $E_m=1.9$ GPa, $\nu_m=0.3$ and for SWCNT : $n_r= 450$ GPa, $k_r= 350$ GPa, $m_r= 1$ GPa, $p_r= 1$ GPa, and $l_r= 10$ GPa. Table 5.1 presents the comparison of Young's modulus for the CNT reinforcement with complete agglomeration ($\eta = 1$). It is found that the results are in good agreement. In Table 5.2, the effective Young's modulus reported by Bisheh *et al.* (2020) is compared with current results for partial agglomeration condition ($\epsilon = 0.5$). The present results are in good agreement with the results reported by Bisheh *et al.* (2020). Finally, in Table 5.3 the results for randomly oriented CNTs ($\epsilon = \eta = 1$) in the matrix are compared with the results of Bisheh *et al.* (2020). The comparison is done to check the equivalence of randomly oriented and uniformly distributed CNTs (Bisheh and Wu 2019) in the matrix. The material properties used are : For matrix: $E_m=78$ GPa, $\nu_m=0.31$ and SWCNT : $n_r= 1089$ GPa, $k_r= 271$ GPa, $m_r= 17$ GPa, $p_r= 442$ GPa, and $l_r= 88$ GPa. It is observed that the present results matches well with the results reported by Bisheh *et al.* (2020). This also indicates the effectiveness of the proposed model to calculate the effective elastic properties of the material analyzed.

5.3.2 Buckling Load Calculation

The estimation of the buckling load considering the non-local effect is validated by comparing the present results with Hosseini-Hashemi *et al.* (2015) as shown in Table 5.4. An analytical method based on HSDT is used by Hosseini-Hashemi *et al.* (2015) to obtain the results. The excellent agreement between references and present results are obtained.

Table 5.1: Comparison of Young's modulus of completely agglomerated CNTs ($\eta = 1$) reinforced composite with Bisheh *et al.* (2020) for different agglomeration parameter

r_v	Agglomeration parameter(ϵ)											
	0.4			0.6			0.8			1		
	Bisheh <i>et al.</i> (2020)	Present	Error%	Bisheh <i>et al.</i> (2020)	Present	Error%	Bisheh <i>et al.</i> (2020)	Present	Error%	Bisheh <i>et al.</i> (2020)	Present	Error%
0.05	3.4467	3.4526	0.17	4.2076	4.2199	0.29	4.9609	4.9818	0.42	5.7070	5.7386	0.55
0.1	3.8461	3.8515	0.14	5.2270	5.2412	0.27	7.0596	7.0917	0.45	9.6100	9.6789	0.71
0.2	4.1346	4.1393	0.11	6.1712	6.1853	0.22	9.7558	9.7988	0.44	17.7442	17.9080	0.92
0.4	4.3136	4.3176	0.09	6.8779	6.8908	0.18	12.5373	12.5880	0.4	35.4761	35.9280	1.2

Table 5.2: Comparison of Young's modulus of partially agglomerated CNTs ($\epsilon = 0.5$) reinforced composite with Bisheh *et al.* (2020) for different agglomeration parameters

r_v	Agglomeration parameter(η)											
	0.5			0.7			0.9					
	Bisheh <i>et al.</i> (2020)	Present	Error%	Bisheh <i>et al.</i> (2020)	Present	Error%	Bisheh <i>et al.</i> (2020)	Present	Error%	Bisheh <i>et al.</i> (2020)	Present	Error%
0.05	5.7070	5.7386	0.55	5.4763	5.5054	0.53	4.6137	4.6325	0.4			
0.1	9.6100	9.6789	0.71	9.0248	9.0874	0.69	6.7096	6.7450	0.52			
0.2	17.7442	17.9080	0.92	16.3563	16.5030	0.89	10.6392	10.7130	0.69			

Table 5.3: Elastic properties comparison of composite reinforced with uniformly dispersed CNTs ($\epsilon = \eta = 1$)

r_v	Elastic properties					
	E(GPa)			K(GPa)		
	Bisheh <i>et al.</i> (2020)	Present	Bisheh <i>et al.</i> (2020)	Present	Bisheh <i>et al.</i> (2020)	Present
0.1	99.2871	99.287	38.1208	38.121	83.6888	83.689
0.2	121.7183	121.72	46.8785	46.878	100.5433	100.54
0.3	145.4283	145.43	56.0746	56.075	119.2454	119.25
0.4	170.5544	170.55	65.7431	65.743	140.1167	140.12

Table 5.4: Comparison of buckling coefficients $\left(\frac{N_{cr}a^2}{D}\right)$ for CNT reinforced simply supported flat panels with Hosseini-Hashemi *et al.* (2015)

	$\frac{a}{b} = 1$			
	$\frac{h}{a} = 0.1$		$\frac{h}{a} = 0.01$	
	Hosseini-Hashemi <i>et al.</i> (2015) HSDT	Present SSDT	Hosseini-Hashemi <i>et al.</i> (2015) HSDT	Present SSDT
$\mu = 0$	18.6861	18.8585	19.7281	19.7299
$\mu = 0.1$	15.6057	15.7497	16.4916	16.4774
$\mu = 0.2$	10.4408	10.5380	11.0136	11.0250
$\mu = 0.3$	6.7200	6.7921	7.1030	7.1060

Table 5.5: Non-dimensional frequency $\left(\Omega = \omega_n\left(\frac{a^2}{h}\sqrt{\frac{\rho_m}{E_m}}\right)\right)$ for CNT reinforced simply supported flat panels with Phung-Van *et al.* (2017)

V_{CNT}	$\frac{a}{h}$	$\mu = 1.5$		$\mu = 4$	
		Phung-Van <i>et al.</i> (2017) HSDT	Present SSDT	Phung-Van <i>et al.</i> (2017) HSDT	Present SSDT
		0.11	10	2.044	2.0415
	20	2.477	2.4729	1.523	1.5207
	50	2.688	2.6879	1.653	1.6529
0.14	10	2.123	2.1224	1.306	1.3052
	20	2.637	2.6334	1.622	1.6194
	50	2.909	2.9099	1.789	1.7894

5.3.3 Free Vibration Frequency Calculation

Natural frequencies of CNT reinforced plate considering the non-local effect presented in Phung-Van *et al.* (2017) is considered since there is no study on the CNT reinforced cylindrical panel. Isogeometric analysis based on HSDT is used in Phung-Van *et al.* (2017) to obtain the free vibration frequencies. The comparison of the results in Table 5.5 indicate that both the results are in good agreement. Excellent agreements of the presence solutions with reference solutions are observed which confirms the accuracy of the semi analytical method.

Table 5.6: Properties of matrix and CNT(Chakraborty *et al.* 2019; Shi *et al.* 2004)

Matrix(PmPV)	Single Walled Carbon Nanotube (SWCNT)
$E_m=2.1\text{GPa}, \nu_m=0.34, \rho_m=1150\frac{\text{kg}}{\text{m}^3}$	$\nu_r=0.175, \rho_r=1400\frac{\text{kg}}{\text{m}^3}$
Hills elastic moduli(GPa): $p_r=1, l_r=10, k_r=30, m_r=1, n_r=450$	

5.4 Free Vibration and Buckling Characteristics for CNT Reinforced Cylindrical Panel

The numerical results for CNT reinforced nanocomposite cylindrical panel considering agglomeration are presented in this section. The matrix is assumed to be poly{(m-phenylenevinylene)-co-[(2,5-dioctoxy-p-phenylene) vinylene]}, known as PmPV, and reinforcement is assumed to be single-walled carbon nanotubes (SWCNTs) and their properties are listed in Table 5.6. In the numerical investigation, the following values are used : $\frac{a}{b} = 1, \frac{a}{h} = 20$.

5.4.1 Buckling Analysis

The buckling analysis under different loads is performed on a square cylindrical panel ($\frac{a}{b} = 1$) having thickness ratio of ($\frac{a}{h} = 20$). Three different type of CNT distributions considered are: a) Uniformly distributed ($\epsilon = \eta = 1$), b) Partially agglomerated ($\epsilon = 0.5, \eta = 0.75$), c) Fully agglomerated ($\epsilon = 0.5, \eta = 1$). The schematic diagram of different CNT distributions is presented in Figure 5.3. Firstly, the panel is assumed to have a fixed volume fraction of CNT ($r_v = 0.1$) and simply supported (SSSS) boundary condition is considered. Three different radius ratios ($\frac{R}{a} = 5, 10, 20$) are considered.

Table 5.7 presents the buckling coefficient, $\bar{N}_0 = (\frac{N_{cr}b^2}{100\rho_r h^3})$, variation for different distributions of CNT and at different values of nonlocal parameter. It is observed that cylindrical panel has high buckling strength for $\epsilon = \eta = 1$ (uniformly distributed) and the increase in agglomeration degree reduces the buckling strength. The lowest buckling coefficient value is observed for $\epsilon = 0.5, \eta = 1$ (fully agglomerated). This is

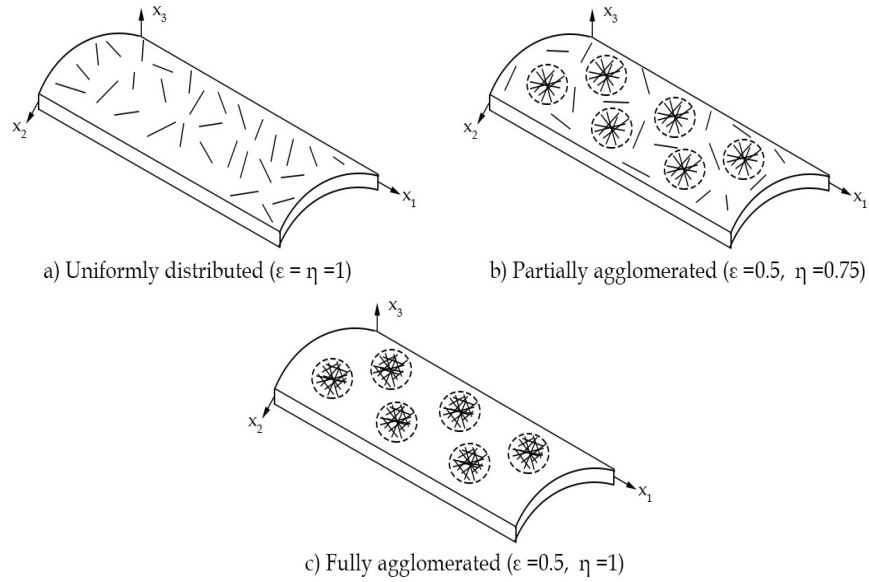


Figure 5.3: Schematic representation of different level of agglomeration

expected as the increase in agglomeration leads to a decrease in stiffness of the structure. It is also observed that with the increase in non-local parameter, the buckling coefficient reduces for all the values of radius ratio. Thus, the non-local effects must be considered while estimating the buckling characteristics. It is also observed that with the increase in radius, the buckling coefficient value reduces. This is due to the reduction of structural stiffness with the increase in the radius of the panel. It is found that the buckling coefficient varies with the type of non-uniform edge loading. The highest and lowest buckling loads are observed for partial tension loading and uniform loading respectively. The presence of a small amount of tension in the loading pattern makes partial tension loading less effective as discussed in the previous chapters.

Figure 5.4 is a graphical representation showing the variation of the buckling coefficient with changes in the non-local parameter, radius ratio, and agglomeration. From Figure 5.4 a) it is clear that buckling coefficient value for a particular radius ratio ($\frac{R}{a} = 5$) and agglomeration degree ($\epsilon = \eta = 1$) reduces with increase in non-local parameter value for all the loading conditions. This is expected as the non-local effect

Table 5.7: Buckling coefficients ($\frac{N_{cr}b^2}{100p_r h^3}$) for CNT reinforced nano composite cylindrical panel under SSSS boundary condition ($a/b=1$, $a/h=20$, $r_v = 0.1$) subject to different NELs

R/a	Dispersed uniformly ($\epsilon = \eta = 1$)			Agglomerated partially ($\epsilon = 0.5, \eta = 0.75$)			Fully agglomerated ($\epsilon = 0.5, \eta = 1$)		
	$\mu = 0$	$\mu = 0.1$	$\mu = 0.2$	$\mu = 0$	$\mu = 0.1$	$\mu = 0.2$	$\mu = 0$	$\mu = 0.1$	$\mu = 0.2$
Uniform Loading									
5	0.3865	0.3228	0.2160	0.3502	0.2925	0.1957	0.1955	0.1633	0.1093
10	0.3575	0.2986	0.1998	0.3240	0.2706	0.1810	0.1811	0.1512	0.1012
20	0.3503	0.2925	0.1957	0.3174	0.2651	0.1774	0.1775	0.1482	0.0992
Trapezoidal Loading									
5	0.5153	0.4304	0.2880	0.4669	0.3900	0.2609	0.2607	0.2177	0.1457
10	0.4767	0.3981	0.2664	0.4320	0.3607	0.2414	0.2414	0.2016	0.1349
20	0.4670	0.3900	0.2610	0.4232	0.3534	0.2365	0.2366	0.1976	0.1322
Triangular Loading									
5	0.7730	0.6455	0.4319	0.7004	0.5849	0.3914	0.3911	0.3266	0.2185
10	0.7150	0.5972	0.3996	0.6479	0.5411	0.3621	0.3621	0.3024	0.2024
20	0.7005	0.5851	0.3915	0.6348	0.5302	0.3547	0.3549	0.2964	0.1983
Partial tension Loading									
5	1.5459	1.2911	0.8639	1.4008	1.1699	0.7828	0.7821	0.6532	0.4370
10	1.4301	1.1943	0.7991	1.2959	1.0822	0.7241	0.7243	0.6049	0.4047
20	1.4011	1.1701	0.7829	1.2696	1.0603	0.7095	0.7098	0.5928	0.3966

is to reduce the buckling load value. Similarly, a reduction in buckling coefficient value is observed with increase in radius ratio as shown in Figure 5.4 b) corresponding to non-local parameter ($\mu = 0.1$) and uniformly distributed CNT ($\epsilon = \eta = 1$). This is because of the reduction in structural stiffness with the increase in radius ratio. Figure 5.4 c) shows the variation in buckling coefficient value with changes in degree of agglomeration of cylindrical panel with radius ratio ($\frac{R}{a} = 5$) and non-local parameter ($\mu = 0.1$). The buckling coefficient reduces with the degree of agglomeration for all the loading conditions. This is due to the reduction in material properties as a result of CNT agglomeration. It is also noted from Figure 5.4 that highest buckling coefficient value is observed for partial tension load while lowest buckling coefficient value is for uniform loading. This is due to the fact that in uniform loading the entire edge is subjected to maximum compressive load whereas in partial tension loading, the edge is subjected to a combined compressive and tensile load. The buckling coefficient values of trapezoidal and triangular value are in between uniform and partial tension loading. The trapezoidal

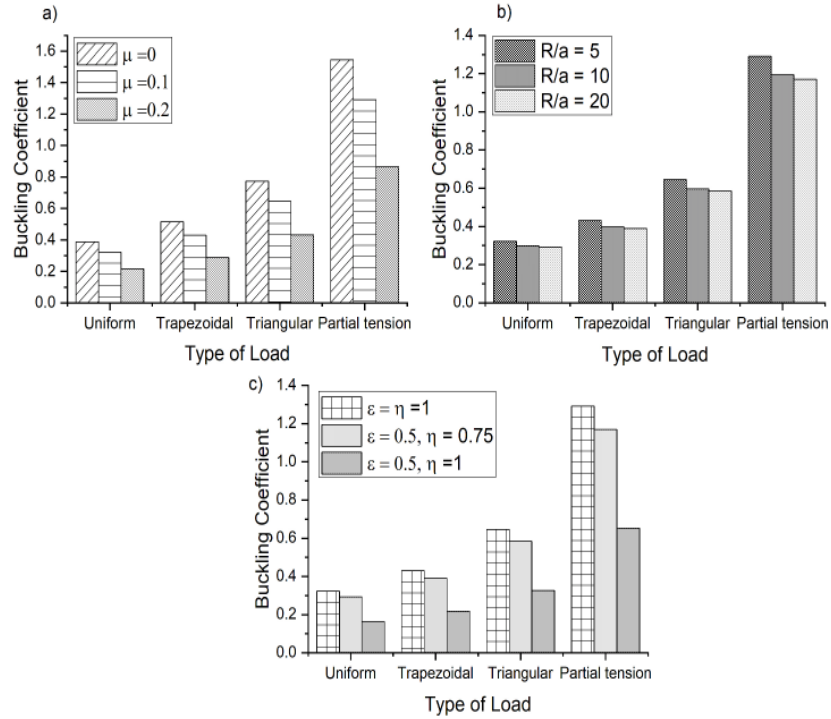


Figure 5.4: Effect of a) non-local parameter(μ) b) radius ratio($\frac{R}{a}$) c) agglomeration on buckling coefficient ($\frac{N_{cr}b^2}{100\rho_r h^3}$) for different type of loading.

loading has a higher effective compressive loading on the edge compared to triangular loading, thus variation in buckling coefficient value is well expected.

Figure 5.5 shows the effect of agglomeration parameter (ϵ -volume fraction of bundle) considering full agglomeration (all the CNTs are in the bundle) on the buckling coefficient of cylindrical panel. The radius ratio($\frac{R}{a}$) and $\frac{a}{h}$ maintained as 20 and volume fraction of CNT(r_v) is 0.2. It is observed that with the increase in the volume fraction of bundle, the buckling coefficient increases for all the loading conditions. This is because when all the CNTs are in bundles the increase in bundle size contributes to improved dispersion of CNTs in the matrix. For the uniformly distributed CNT condition, i. e., $\epsilon = 1$, the highest value of buckling coefficient is obtained. There is a change in buckling coefficient value with an increase in the volume fraction of CNT (r_v) and non-local

parameter (μ) is observed. It can be observed that with the increase in agglomeration parameter (ϵ), there is not much increase in buckling coefficient even though the volume fraction of CNT (r_v) is increased up to $\epsilon = 0.5$ which denotes complete agglomeration. This is because of the agglomeration which can cause only a marginal improvement in material properties. Further, as ϵ increases beyond 0.5 distribution start to improve and the influence of volume fraction will become more evident. It can be observed that the increase in volume fraction causes a very high increase in buckling coefficient. For instance, the rate of increase in buckling coefficient is very high for $r_v=0.2$ compared to $r_v=0.1$. This is expected as the increased amount of CNTs in the matrix enhances the mechanical performance of the composite. One can also be observed that the non-local parameter causes a similar reduction in the buckling coefficient in the buckling coefficient for all the load cases. Furthermore, the effect of volume fraction of CNT (r_v) dominates the non-local effect when CNT distribution is uniform. As seen from Figure 5.5, the buckling coefficient value for $r_v=0.2$ and $\mu=0.2$ is higher than $r_v=0.1$ and $\mu=0.1$. Even though the non-local parameter is higher in the first case, the dominating effect of the volume fraction of CNT is the reason for the higher buckling coefficient value.

The influence of partial CNT agglomeration ($\epsilon = 0.5$ and $\epsilon \leq \eta$) on the buckling coefficient for various value of η are presented in Figure 5.6. The agglomeration changes from fully agglomerated ($\epsilon = 0.5, \eta=1$) to uniformly distributed ($\epsilon = 0.5, \eta=0.5$). Similar to Figure 5.5 the effect of increased volume fraction of CNT dominates the non-local effect as the CNT distribution becomes uniform. For instance, the cylindrical panel with $r_v=0.2$ and $\mu=0.2$ provides better buckling strength than $r_v=0.1$ and $\mu=0.1$ as CNT distribution tend towards uniform. This is due to the enhancement of material properties as a result of increased CNT volume fraction. The highest buckling coefficient is observed for $\epsilon=\eta=0.5$ and the lowest value is observed for $\epsilon = 0.5$ and $\eta=1$. This is expected as $\eta=\epsilon=0.5$ represents uniform distribution and $\epsilon = 0.5$ and $\eta=1$ denotes full agglomeration. Thus it is evident that with the increase in agglomeration the buckling coefficient reduces for all the loading conditions due to the reduction in material properties.

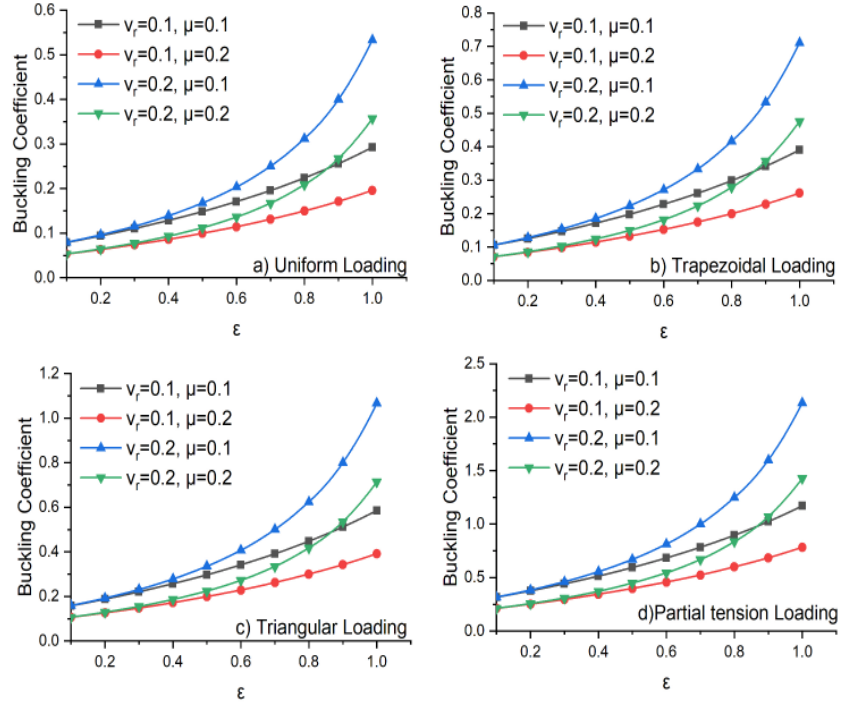


Figure 5.5: Variation of buckling coefficient ($\frac{N_{cr} b^2}{100 p_r h^3}$) considering complete agglomeration ($\eta = 1$) with change in agglomeration parameter(ϵ) for different CNT volume fractions(v_r)

Figure 5.7 presents the variation of the buckling coefficient for different values of ϵ and η as the non-local parameter is increased. It is evident that the buckling coefficients reduce as the non-local parameter increases for all the different loading conditions. It is observed that the uniformly distributed CNT case results in the highest buckling coefficient. This is due to enhanced material properties as a result of uniform distribution. As seen from Figure 5.7, a drastic reduction of the buckling coefficient for uniformly distributed case ($\epsilon = \eta = 1$) is observed as μ increases from 0.2. This is because of the dominant influence of non-local parameter on the buckling coefficient value. It is evident from the fact that for a high non-local parameter value, $\mu = 1$, the buckling coefficient value becomes very less.

The variation of the buckling coefficient with the non-local parameter for partially

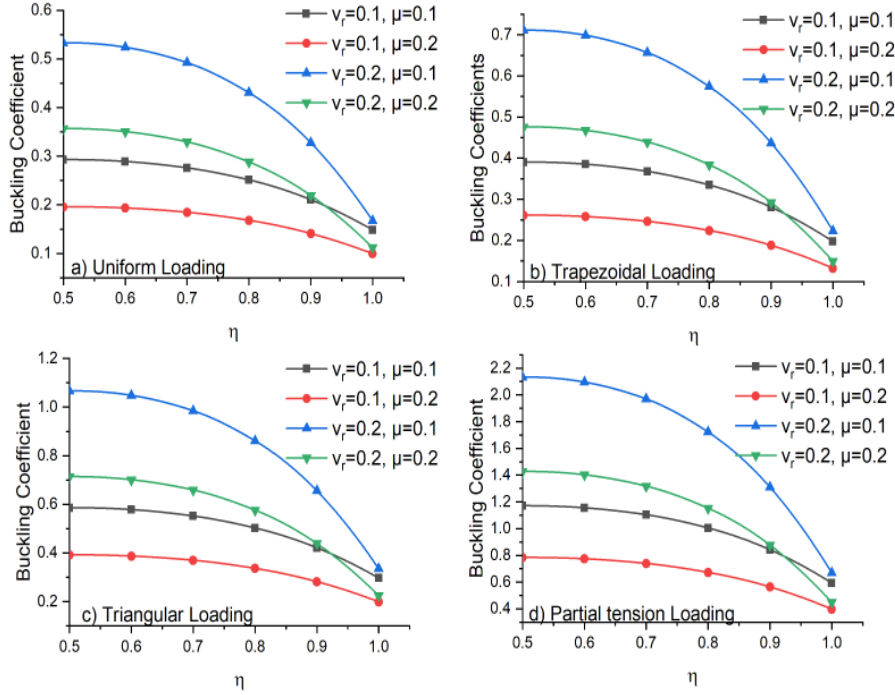


Figure 5.6: Variation of buckling coefficient ($\frac{N_{cr}b^2}{100p_r h^3}$) considering partial agglomeration ($\epsilon = 0.5$) with change in agglomeration parameter(η) for different CNT volume fractions(v_r)

agglomerated ($\epsilon = 0.5$) cylindrical panel under different loading conditions is shown in Figure 5.8. It is observed that the highest buckling coefficient value is observed for $\epsilon = \eta = 0.5$ case, i. e., for the uniformly distributed CNT panel. With the increase of non-local parameter, the buckling coefficient value reduces for all the cases. This is expected as the non-local parameter value increases, its influence on geometric stiffness increases which leads to the dominating effect such that buckling coefficient value reduces drastically.

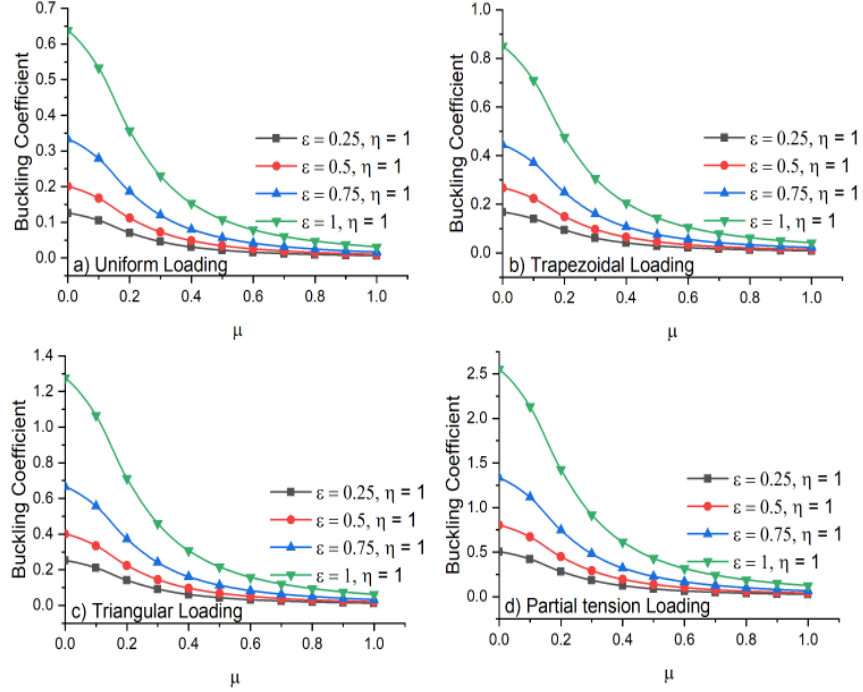


Figure 5.7: Variation of buckling coefficient ($\frac{N_{cr} b^2}{100 \rho_r h^3}$) considering full agglomeration ($\eta = 1$) with change in non-local parameter (μ) for different combinations of ϵ and η

5.4.2 Free Vibration Analysis

The non-dimensional fundamental frequency of agglomerated CNT reinforced cylindrical panel under different non-uniform edge loads is presented in this section. The cylindrical panel having the dimensions ($\frac{a}{b} = 1, \frac{a}{h} = 20, \frac{R}{a} = 5, 10, 20$) considered for buckling analysis is considered for free vibration studies also. The volume fraction of CNT is maintained as $r_v = 0.1$ and free vibration frequency is presented in non-dimensional form as $\Omega = \omega_n \left(\frac{a^2}{h} \sqrt{\frac{\rho_m}{\rho_r}} \right)$.

Non-dimensional frequency of CNT reinforced cylindrical panel considering agglomeration effect under various radius ratio ($\frac{R}{a} = 5, 10, 20$) for different values of non-local parameter is presented in Table 5.8. Notably, the non-dimensional frequency reduces with an increase in the degree of agglomeration. It is due to a reduction in

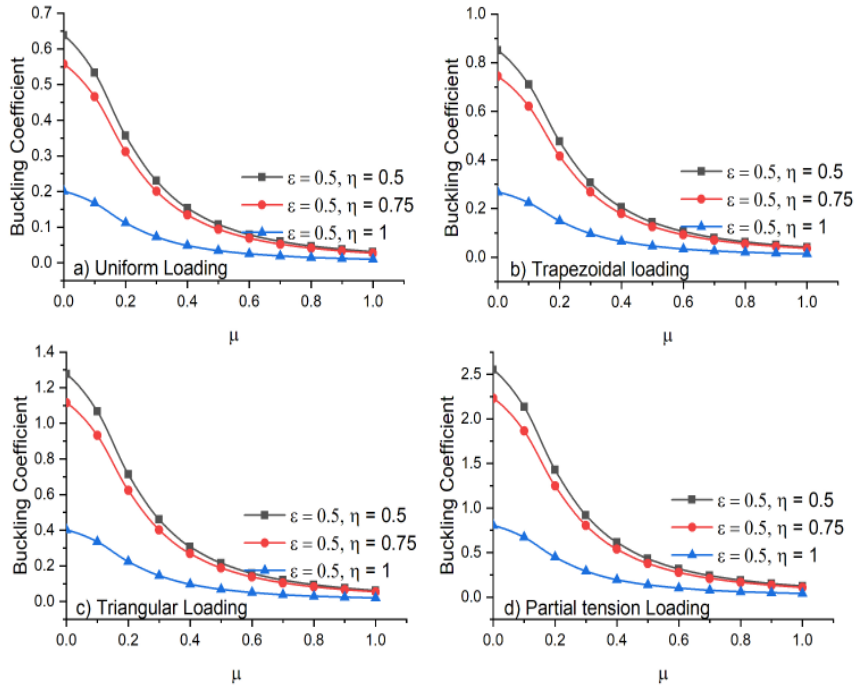


Figure 5.8: Variation of buckling coefficient ($N_{cr}b^2/100p_rh^3$) considering partial agglomeration ($\epsilon = 0.5$) with change in non-local parameter(μ) for different combinations of ϵ and η

structural stiffness with the increase in the degree of agglomeration. It is also noted that the increase in non-local parameter reduces the natural frequency. This is because of the influence of non-local parameter in increasing the mass matrix coefficients without altering the structural stiffness. It is also observed that the natural frequency changes with boundary conditions and the highest value of frequency are observed in the CCCC boundary condition, which is due to the presence of clamped edges in the fully clamped boundary condition.

The variation of the non-dimensional natural frequency of CNT reinforced cylindrical panel with changes in the local parameter is depicted in Figure 5.9. The first part (a) denotes the reduction of the natural frequency with an increase in non-local parameter for the SSSS boundary condition. This is due to the influence of the nonlocal parameter

Table 5.8: Non-dimensional frequency ($\Omega = \omega_n \left(\frac{a^2}{h} \sqrt{\frac{\rho_m}{p_r}} \right)$) for CNT reinforced nano composite cylindrical panel under SSSS boundary condition ($a/b=1, a/h=20, r_v = 0.1$).

R/a	Dispersed uniformly ($\epsilon = \eta = 1$)			Agglomerated partially ($\epsilon = 0.5, \eta = 0.75$)			Fully agglomerated ($\epsilon = 0.5, \eta = 1$)		
	$\mu = 0$	$\mu = 0.1$	$\mu = 0.2$	$\mu = 0$	$\mu = 0.1$	$\mu = 0.2$	$\mu = 0$	$\mu = 0.1$	$\mu = 0.2$
SSSS									
5	19.2845	17.6234	14.4157	18.3570	16.7758	13.7223	13.7166	12.5351	10.2535
10	18.5472	16.9497	13.8645	17.6556	16.1348	13.1980	13.1993	12.0624	9.8668
20	18.3578	16.7765	13.7229	17.4753	15.9701	13.0633	13.0664	11.9409	9.7675
CCCC									
5	34.1172	30.5478	24.1889	32.4770	29.0793	23.0260	24.2803	21.7401	17.2146
10	33.6532	30.1311	23.8573	32.0356	28.6828	22.7106	23.9543	21.4473	16.9816
20	33.5359	30.0257	23.7735	31.9240	28.5826	22.6308	23.8719	21.3732	16.9227

on the natural frequency. Here $\mu = 0$ denotes results obtained based on classical mechanics theory. The highest value for frequency is observed for $\epsilon = \eta = 1$ (uniformly distributed) condition. This is expected as the elastic properties are improved with the uniform dispersion of CNTs in the matrix. Part (b) of Figure 5.9 shows the influence of the nonlocal parameter on non-dimensional natural frequency for fully clamped (CCCC) boundary condition. The natural frequencies reduce the same as the simply supported condition and the highest frequency is observed for the uniformly distributed CNT condition.

The influence of the different type of non-uniform edge load on the fundamental frequency of CNT reinforced panel at different degree of agglomeration and the non-local parameter is presented in Figure 5.10. It is observed that as the intensity of edge loading increases, the natural frequency of the cylindrical panel decreases. This is due to the influence of the edge load on the stiffness of the structure. The reduction of natural frequency to zero happens at a very low load for fully agglomerated case ($\epsilon = 0.5, \eta = 1$) and non-local parameter (μ) 0.2. This is expected as the reduction in stiffness happens with agglomeration and increased influence of non-local parameter on mass. Further to understand the effect of different type of loading pattern on the reduction in natural frequency value, Figure 5.11 is plotted for uniformly CNT distributed cylindrical panel. $\epsilon = 1, \eta = 1$ and $\mu = 0.1$ is considered. It is clear from Figure 5.11 that reduction rate

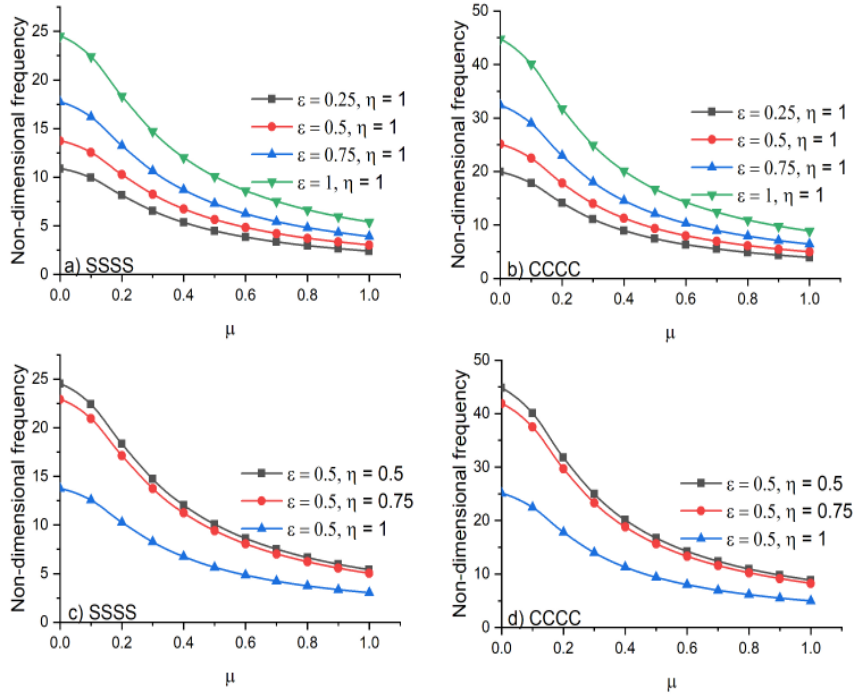


Figure 5.9: Variation of non-dimensional frequency ($\Omega = \omega_n(\frac{a^2}{h} \sqrt{\frac{\rho_m}{p_r}})$) considering partial agglomeration ($\epsilon = 0.5$) with change in agglomeration parameter(η) for different CNT volume fractions(v_r)

of natural frequency with increase in compressive load is different for various loading conditions. This is expected as the reduction in transverse stiffness occurs with increase in magnitude of in plane loading which in turn is highly depend upon the nature of variation of the non-uniform edge load. The free vibration mode shape remains same as (1,1) with increase in intensity of the edge load.

5.5 Closure

The size dependent buckling and free vibration behaviour of CNT reinforced cylindrical nano panel considering agglomeration subject to different NELs using a semi-analytical

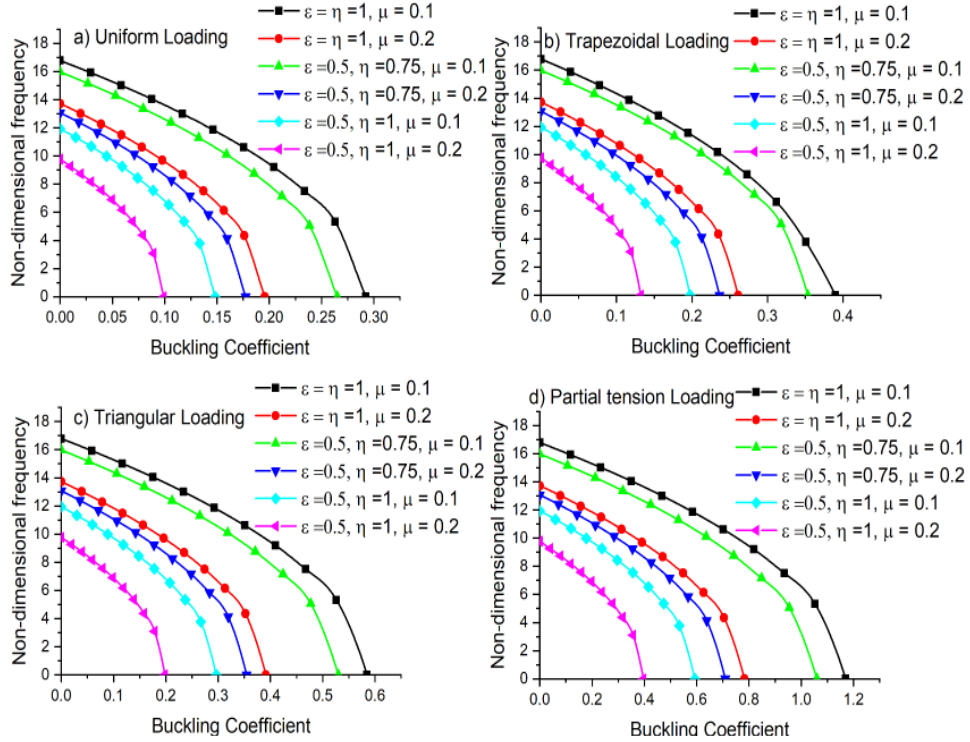


Figure 5.10: Effect of compressive load on non-dimensional frequency ($\Omega = \omega_n \left(\frac{a^2}{h} \sqrt{\frac{\rho_m}{p_r}} \right)$) of SSSS cylindrical panel for all the type of loadings

method utilizing Galerkin's method considering non-local elasticity theory is presented. Two parameter micro mechanical model is used for the estimation of mechanical properties. A non-local parameter is introduced to evaluate the size effects. The accuracy of the present solutions are verified by comparing authors results with various analytical solutions available in the literature. The influence of non-local parameter, CNT agglomeration, NELs on buckling, and free vibration response is presented. The buckling strength of cylindrical nano panel depends primarily on the non-local parameter, type of NEL and degree of CNT agglomeration. The free vibration response of cylindrical nano panel depends largely on non-local parameter, degree of CNT agglomeration and boundary conditions. The critical buckling load is influenced by the type of NEL. The highest value of buckling load is observed for partial tension loading and the lowest for uniformly distributed edge load. For the CNT reinforced cylindrical nano panel, the

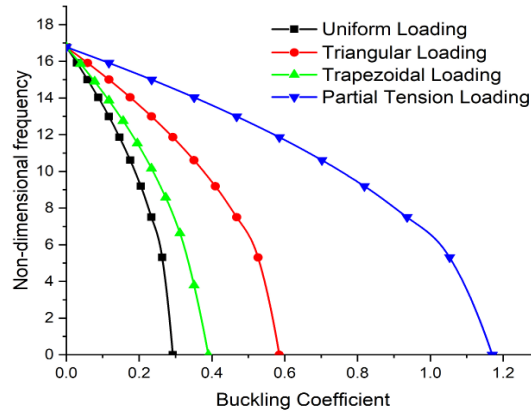


Figure 5.11: Effect of compressive load on non-dimensional frequency ($\Omega = \omega_n \left(\frac{a^2}{h} \sqrt{\frac{\rho_m}{p_r}} \right)$) of uniformly distributed CNT reinforced cylindrical panel under SSSS boundary condition for different loadings

consideration of size effect reduces the stiffness thus the buckling and free vibration performance is poor. The reduction in natural frequency with the increase in buckling load is different for various NELs.

CHAPTER 6

FREE VIBRATION-BUCKLING ANALYSIS ON GOP REINFORCED CYLINDRICAL PANEL

6.1 Introduction

In the previous chapters, buckling and free vibration of cylindrical panels reinforced with GPL and CNT are investigated. The buckling and free vibration characteristics of Graphene oxide powder (GOP) reinforced cylindrical panels need to be analysed next since it has several advantages such as ease of availability and ability to form better interfaces with polymer matrix.

In this chapter, the buckling and free vibration response under different non-uniform edge and partial edge loads of functionally graded graphene oxide powder reinforced cylindrical panel is analyzed. The graphene oxide powder is functionally graded along the thickness in three different patterns and amount of GOP reinforcement is also varied. To obtain the solutions, the governing differential equations are solved for natural frequency, critical buckling load and mode shapes utilizing Galerkin's method subjected to different types NELs.

6.2 Material Modelling of GOP Reinforced Composite

The GOP reinforced composite cylindrical panel has material properties varying in thickness direction in three different patterns given as : (a) U-GOPRC-in which GOP is distributed uniformly through the thickness, (b) X-GOPRC-in which the concentration of GOP increases from center to the surfaces, (c) O-GOPRC-in which the concentration

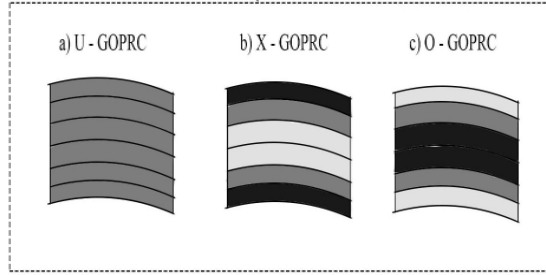


Figure 6.1: Different types of GOP distribution patterns

of GOP increases from surface to the center (Figure 6.1). Thus, considering Ebrahimi *et al.* (2021); Zheng *et al.* (2021) the material properties of GOP reinforced cylindrical panel such as density (ρ_{GOPRC}), Poisson's ratio (ν_{GOPRC}) and Young's modulus (E_{GOPRC}) are estimated by Halpin-Tsai model given as:

$$\begin{aligned}
 \rho_{GOPRC} &= \rho_{GOP}V_{GOP} + \rho_m V_m \\
 \nu_{GOPRC} &= \nu_{GOP}V_{GOP} + \nu_m V_m \\
 E_{GOPRC} &= 0.49E_l + 0.51E_t
 \end{aligned} \tag{6.1}$$

Where, ρ_{GOP} , ρ_m represent density of reinforcement(GOP), matrix, V_{GOP} , V_m represent volume fraction of reinforcement, matrix and ν_{GOP} , ν_m represent Poisson's ratio of reinforcement (GOP), matrix respectively. E_t and E_l represents transverse and longitudinal moduli of the nano composite cylindrical panel reinforced with GOP. The volume fraction of GOP (V_{GOP}) for different layers varies according to the different patterns and it is defined as:

$$\begin{aligned}
 U - GOPRC : V_{GOP}(l) &= V'_{GOP} \\
 X - GOPRC : V_{GOP}(l) &= \frac{2}{NL}|2l - NL - 1|V'_{GOP} \\
 O - GOPRC : V_{GOP}(l) &= \frac{2}{NL}(1 - |2l - NL - 1|)V'_{GOP}
 \end{aligned} \tag{6.2}$$

Here, total number of layers is represented by NL and $l=1, 2, \dots, NL$. The relationship between volume fraction of matrix (V_m) and volume fraction of GOP's (V_{GOP}) are

related as:

$$V_{GOP} + V_m = 1 \quad (6.3)$$

In Equation 6.2, V'_{GOP} is the total volume fraction of GOP in the cylindrical panel and given as:

$$V'_{GOP} = \frac{W_{GOP}}{W_{GOP} + (1 - W_{GOP})(\rho_{GOP}/\rho_m)} \quad (6.4)$$

Here, W_{GOP} represents the weight fraction of GOP. The longitudinal (E_l) and transverse (E_t) moduli of the composite in Equation 6.1 is given as:

$$\begin{aligned} E_l &= \frac{1 + \xi_l \eta_l V_{GOP}}{1 - \eta_l V_{GOP}} \times E_m \\ E_t &= \frac{1 + \xi_t \eta_t V_{GOP}}{1 - \eta_t V_{GOP}} \times E_m \end{aligned} \quad (6.5)$$

Here, η_l , η_t represents parameters and E_m represents Young's moduli of the matrix material which are defined as:

$$\eta_l = \frac{\frac{E_{GOP} - 1}{E_m}}{\frac{E_{GOP} - 1}{E_m} + \xi_l}, \quad \eta_t = \frac{\frac{E_{GOP} - 1}{E_m}}{\frac{E_{GOP} - 1}{E_m} + \xi_t} \quad (6.6)$$

where, ξ_l and ξ_t are geometry factors given as:

$$\xi_l = \xi_t = \frac{2d_{GOP}}{h_{GOP}} \quad (6.7)$$

where, h_{GOP} and d_{GOP} are the thickness and diameter of GOP respectively. Using the Young's modulus (E_{GOP}), Poisson's ratio (ν_{GOP}) and density (ρ_{GOP}) the different coefficients are calculated and buckling and free vibration characteristics are obtained as mentioned in Section 2.

6.3 Validation of Material Modelling

To assure the accuracy and effectiveness of the present mathematical model of GOP reinforced composite validation study is conducted based on results available in the

literature and presented in this section.

The dimensionless buckling load $\left\{ \bar{N}_0 = N_{cr} \left(\frac{R\sqrt{3(1-\nu_m)}}{100E_m h^3} \right) \right\}$ of a cylindrical shell reinforced with GOP for different weight fractions of GOP are presented in Figure 6.2 together with results of Ebrahimi *et al.* (2021). In Section 4, the material properties used for the present study are presented. The cylindrical shell is considered simply supported with the geometric parameters defined as: $\frac{L}{h} = \frac{R}{h} = 20$. The dimensionless buckling load obtained using present study and those obtained by Ebrahimi *et al.* (2021) are in close agreement.

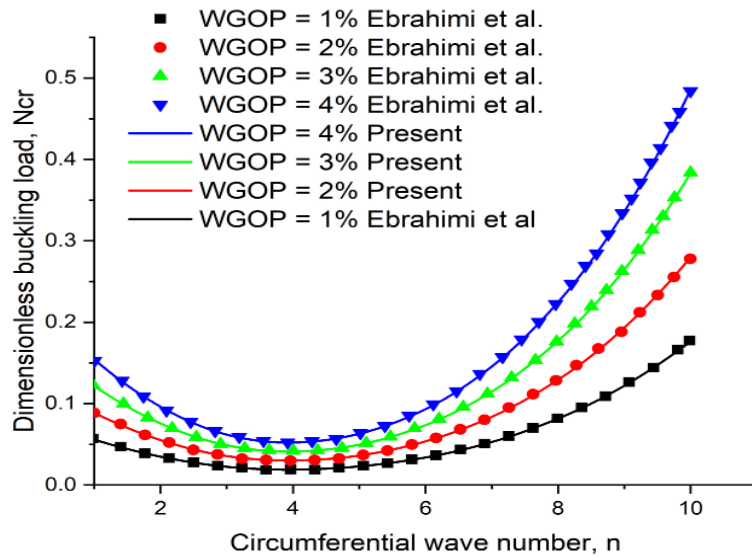


Figure 6.2: Comparison of dimensionless buckling load ($\bar{N}_0 = N_{cr} \left(\frac{R\sqrt{3(1-\nu_m)}}{100E_m h^3} \right)$) of SSSS GOP cylindrical shell

6.4 Free Vibration and Buckling Characteristics for GOP Reinforced Cylindrical Panel

The present study aims to investigate the influence of NELs on free vibration and buckling response of FG-GOP reinforced cylindrical panel. The matrix is assumed to be Epoxy and reinforcement is graphene oxide powder (GOP) with the following properties (Zhang *et al.* 2020), (Lin *et al.* 2014):

$$\begin{aligned} E_m &= 3.0GPa, \nu_m = 0.34 \text{ and } \rho_m = 1200 \frac{kg}{m^3} : \text{Epoxy Matrix} \\ E_{GOP} &= 444.8GPa, \nu_{GOP} = 0.165 \text{ and } \rho_{GOP} = 1090 \frac{kg}{m^3} : \text{GOP Reinforcement} \end{aligned} \quad (6.8)$$

The GOP is considered as a circular shaped reinforcement having a thickness $t = 0.95$ nm and diameter $d = 500$ nm as given in (Lin *et al.* 2014). The following convention is used for boundary conditions, for instance, 'C' and 'S' denotes clamped and simply supported boundary conditions respectively. Thus, 'CCCC' and 'SSSS' denotes all edges clamped and all edges simply supported boundary conditions respectively. The geometric properties are assumed as the following though out the study unless otherwise mentioned as: $\frac{a}{b} = 1$, $\frac{R}{a} = 20$, $W_{GOP} = 2wt\%$ and cylindrical panel thickness ratio is assumed as $\frac{a}{h} = 100$.

6.4.1 Buckling Studies

In this section, the influence of GOP distribution and it's concentration on buckling behaviour under different NELs is studied first. Following that the influence of aspect ratio ($\frac{a}{b}$) on buckling characteristics of nano composite cylindrical panel is analysed in detail. The expression for critical buckling coefficient is given as $\bar{N}_0 = N_{cr}(\frac{b^2}{100E_m h^3})$. Here, λ denotes the lowest eigen-value obtained from the buckling problem.

6.4.1.1 Influence of GOP Distribution and Its Volume Fraction

As a first study, the GOP cylindrical panel is assumed to be square ($\frac{a}{b} = 1$) with thickness ratio ($\frac{a}{h} = 100$) and radius ratio ($\frac{R}{a} = 20$) and boundary condition is considered to be simply supported (SSSS). The variation of buckling coefficient for a GOP reinforced cylindrical panel is affected by two different factors, namely GOP weight fraction and GOP distribution. Therefore, buckling coefficient value is calculated for different values of GOP weight fraction for different distribution are shown in Figure 6.3. The sub figure (a) in Figure 6.3 denotes variation of buckling coefficients for uniformly distributed GOP reinforced cylindrical panel. The buckling coefficient value increases with increase in GOP concentration, due to enhancement in structural stiffness due to addition of GOP. It can be seen that minimum buckling coefficient is observed for partial edge loading and maximum for reverse sinusoidal loading. The highest intensity of load at the center of the nano composite cylindrical panel is the main reasoning for lowest buckling coefficient value for partial edge loading. While for reverse sinusoidal loading highest intensity of loading is at the edges and results in higher buckling coefficient value. A glance again at Figure 6.3 reveals that buckling coefficient value varies in the increasing order of uniform loading, parabolic loading followed by increasing parabolic loading. The highest buckling coefficient value is observed for X-GOPRC distribution and lowest is observed for O-GOPRC for all the loading conditions. This is due to higher quantity of GOP at the top and bottom fibres for X-GOPRC giving rise to enhance the buckling strength. On the other hand, for O-GOPRC distribution, less amount of GOP at the top and bottom layers leading to reduction in buckling strength because of lower bending stiffness.

Further, to show the influence of GOP distribution on the buckling coefficient value with increase in GOP weight fraction, Figure 6.4 is plotted. The cylindrical panel is assumed to be simply supported with $\frac{a}{b} = 1$, $\frac{a}{h} = 100$ and $\frac{R}{a} = 20$. The GOP weight fraction is varied from 0 to 3 and the corresponding change in buckling coefficient value is plotted. The variation in buckling coefficient is shown for two different type of load-

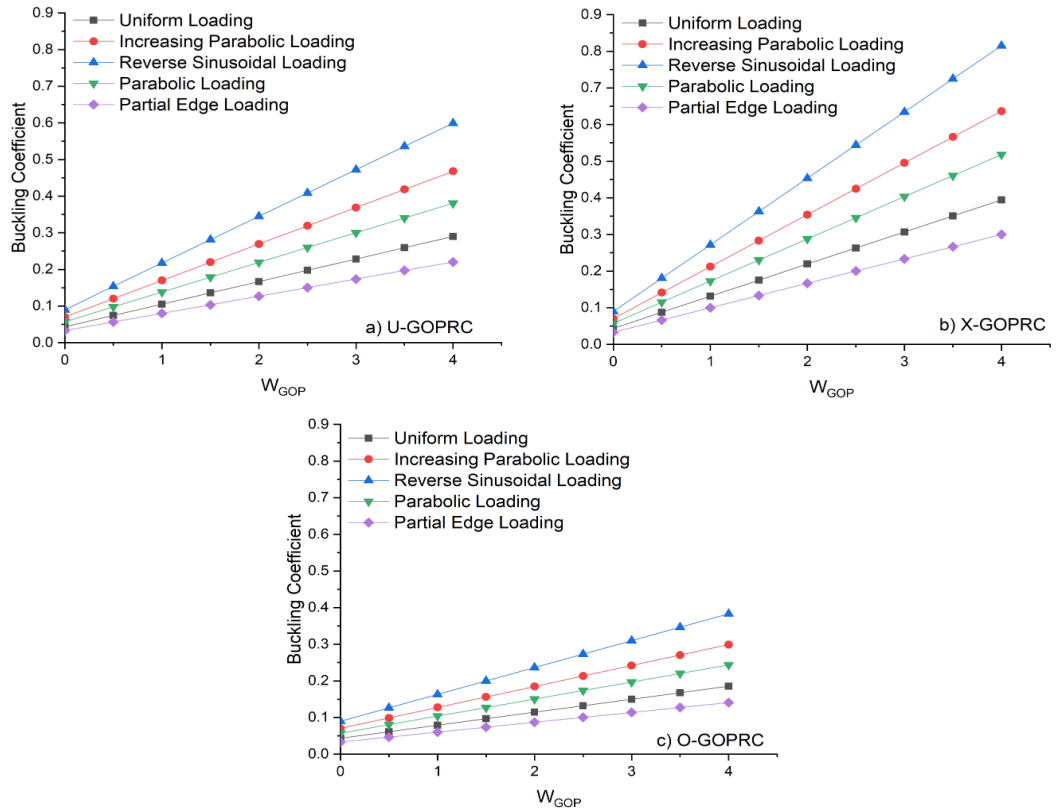


Figure 6.3: Buckling coefficients ($N_{cr}(\frac{b^2}{100E_m h^3})$) for a square, SSSS, GOP reinforced nano composite cylindrical panel under different edge loading: Influence of various distribution and weight fraction of GOP.

ing conditions namely, uniform and partial edge loading. It is observed that there is a 70 % increase in buckling coefficient value with the addition of 0.5 wt fraction of GOP for U-GOPRC, 100 % increase for X-GOPRC and 40 % increase for O-GOPRC distributions respectively. The reason being the presence of large amount of GOP at the extreme surfaces for X-GOPRC while less amount for O-GOPRC as already discussed. This establishes the influence of various distribution of GOP reinforcement in enhancing the buckling strength of the cylindrical panel.

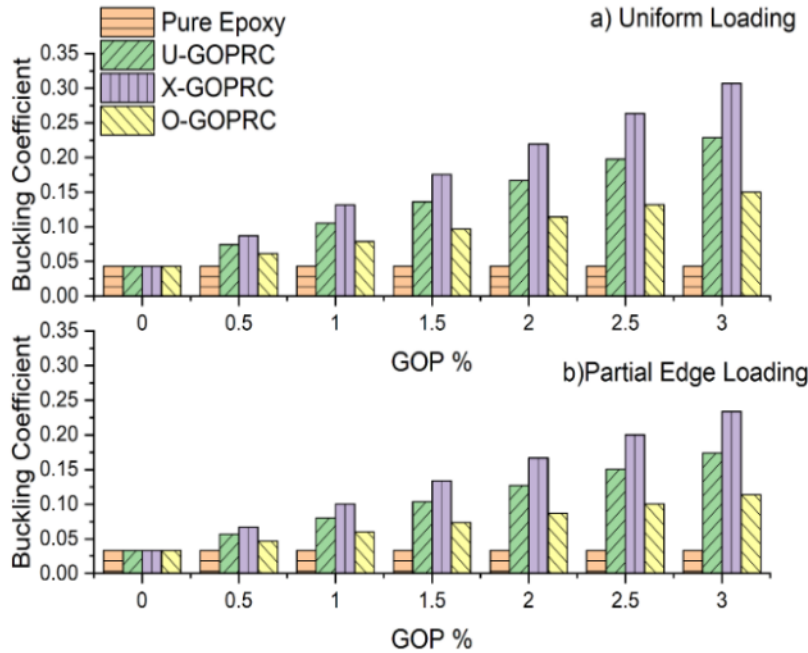


Figure 6.4: Increase of buckling coefficients ($N_{cr}(\frac{b^2}{100E_m h^3})$) for various distributions of GOP (SSSS square cylindrical panel) with increase in GOP content (a)uniform loading (b)partial edge loading.

6.4.1.2 Influence of Aspect Ratio

The change in buckling coefficient value with the change in aspect ratio is presented in Figure 6.5. Fixed amount of GOP weight fraction is considered as 2 wt% and thickness and radius ratio are assumed as $\frac{a}{h} = 100$, $\frac{R}{a} = 20$ respectively. Influence of type of GOP distribution on the buckling coefficient with respect to aspect ratio ($\frac{a}{b}$) is analyzed in Figure 6.5. The buckling coefficient value differs with the type of GOP distribution. The minimal buckling coefficient value is observed for O-GOPRC cylindrical panel while the maximal buckling coefficient value is observed for X-GOPRC cylindrical panel for different type of loadings considered. This is due to higher amount of GOP in the top and bottom fibres for X-GOPRC and least amount for O-GOPRC. The results also indicate that variation of fundamental buckling mode from (1,1) to (2,1) for a type of loading occurs at the same aspect ratio ($\frac{a}{b}$) and doesn't vary with the type of

GOP distribution. Further analysis of Figure 6.5 indicate that the variation of buckling coefficient with the change in aspect ratio is different for various type of loading. The shift of fundamental buckling mode to (2,1) from (1,1) with increase in aspect ratio ($\frac{a}{b}$) occurs for all type of loadings. The reason for changes in buckling modes with increase in aspect ratio can be explained as follows: as aspect ratio increases, the energy input required for large buckling deformation is least for (2,1) mode rather than (1,1). Thus, (2,1) buckling mode shapes becomes the primary buckling mode shape. It is also interesting to know that this change in aspect ratio occurs at different aspect ratio for different loadings. This is due to the fact that concentrated type of loadings has the highest efficiency in facilitating this energy transformation. Thus, for partial edge loading and parabolic loading, which has center concentrated loading give rise to mode shape change at a low aspect ratio. For clear understanding, buckling coefficients with change in aspect ratio for X-GOPRC composite cylindrical panel is presented in Figure 6.6. The change from (1,1) to (2,1) occurs at aspect ratios namely, 1.5 for uniform loading, 1.6 for increasing parabolic loading, 1.9 for reverse sinusoidal loading, 1.3 for parabolic loading and 1.3 for partial edge loading. This can be related to the effectiveness of the different applied non-uniform edge loads as already explained. For the case of partial edge and parabolic loading, highest intensity of load is present at the center which is the reason for its high effectiveness. On the other hand, reverse sinusoidal loading has least concentration of load at the center making it the least effective load.

6.4.2 Free Vibration Studies

In this study, influence of GOP concentration and distribution on the fundamental free vibration frequency is analysed first. In order to analyze the variation of free vibration frequency with different boundary conditions, SSSS(simply supported) and CCCC (clamped) are considered. Later, the influence of different types of non-uniform edge loadings on the first two natural frequencies of the cylindrical panel is analysed in detail. The non-dimensional form, $\Omega = \omega_n \left(\frac{a^2}{h} \sqrt{\frac{\rho_m}{E_m}} \right)$, is used for the free vibration frequency.

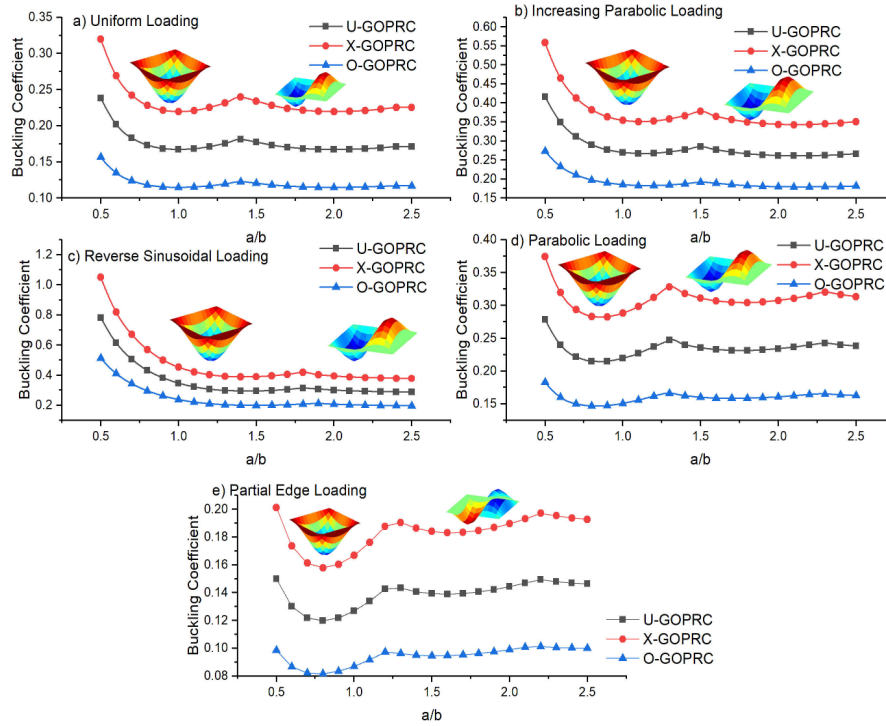


Figure 6.5: Variation of buckling coefficients $\left(N_{cr}\left(\frac{b^2}{100E_m h^3}\right)\right)$ for simply supported, GOP reinforced cylindrical panel subjected different edge loading: Influence of aspect ratio

6.4.2.1 Influence of GOP Volume Fraction and Its Distribution

In Figure 6.7, the influence of weight fraction of GOP and distribution on the fundamental free vibration frequency is presented. The nano composite cylindrical panel is considered to be square ($\frac{a}{b} = 1$) with thickness ratio ($\frac{a}{h} = 100$) and radius ratio ($\frac{R}{a} = 20$). It can be seen from Figure 6.7 that free vibration frequency increases as GOP concentration rises. This is due to the fact that as the amount of GOP increases an improvement in the structural stiffness of the panel occurs which in turn leads to the increase in frequency. A glance again on Figure 6.7 reveals that X-GOPRC distribution has the maximum natural frequency value. This indicate that the distribution of GOP

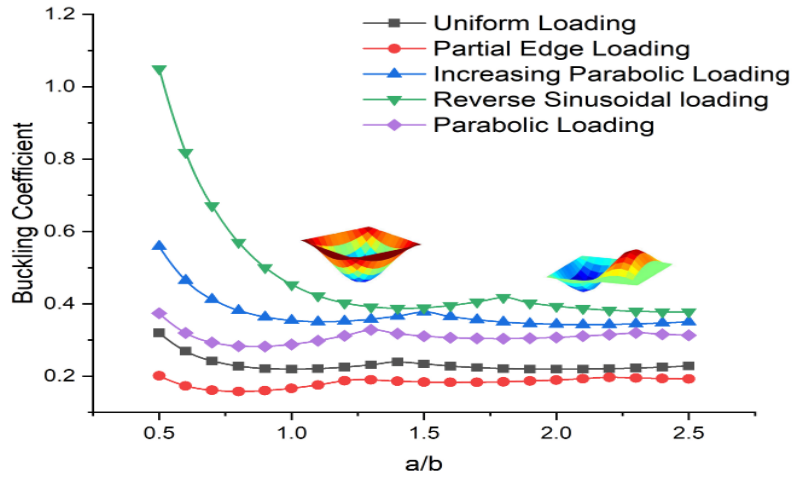


Figure 6.6: Variation of buckling coefficients ($N_{cr}(\frac{b^2}{100E_m h^3})$) with aspect ratio for a simply supported, GOP reinforced cylindrical panel under X-GOPRC distribution: Influence of edge loading.

has a higher influence than GOP concentration. The reason for the higher value of frequency for X-GOPRC distribution is due to that fact that higher concentration of GOP is present at the top and bottom layers giving rise to higher stiffness. It can be seen from Figure 6.7 (b) that free vibration frequency varies with the type of boundary condition. Further, the fully clamped (CCCC) nano composite cylindrical panel notes the the highest free vibration frequency value. The clamped nano composite cylindrical panel also shows a similar trend of increase in natural frequency with GOP concentration.

6.4.2.2 Influence of Type of NEL and Aspect Ratio

It is interesting to know the variation of free vibration frequency and mode with increase in compressive load for different type of loadings. For this reason, in Figures 6.8 and 6.9, the variation of first two free vibration frequencies with increase in compressive load upto lowest critical buckling load for the nano composite cylindrical panel with aspect ratios 1 and 1.3 respectively are presented.

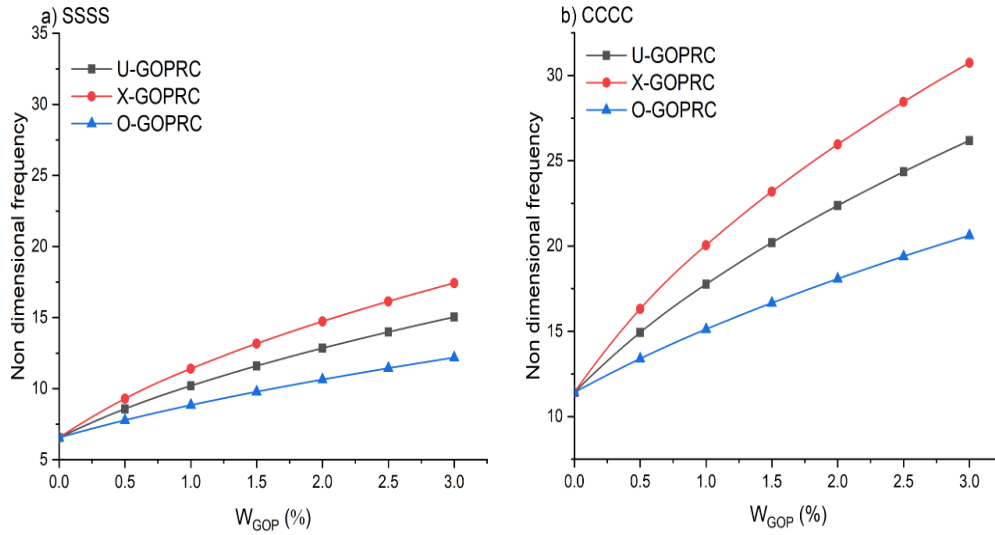


Figure 6.7: Variation of non dimensional frequency ($\Omega = \omega(\frac{a^2}{h} \sqrt{\frac{\rho m}{E_m}})$) of clamped and simply supported GOP reinforced cylindrical panel: Influence of various distribution and weight fraction of GOP.

The influence of increase in compressive load on non-dimensional frequencies for a square ($\frac{a}{b}=1$) GOP reinforced cylindrical panel is presented in Figure 6.8. A close observation of Figure 6.8 reveals that there is a reduction in the first two natural frequencies with increase in compressive load. The partial edge loading notes the highest rate of reduction whereas reverse sinusoidal loading notes the lowest reduction rate. This is expected as panel center has the highest intensity of load for partial edge loading leading to its high effectiveness while panel center has lowest intensity for reverse sinusoidal loading. In increasing steps, the amount of compressive load is varied upto lowest critical buckling load corresponding to a type of loading. It is observed that the natural frequency corresponding to (1,1) mode reduces to zero at critical buckling load. The application of uniform load, parabolic load, increasing parabolic load shows a similar trend of reduction in natural frequency according to the effectiveness of the load as already discussed. The free vibration frequency corresponding to (2,1) mode also reduces and attains a value according to the type of loading. It is also observed that frequencies corresponding to all the type of distribution of GOP show a similar

reduction with values varying according to the distribution.

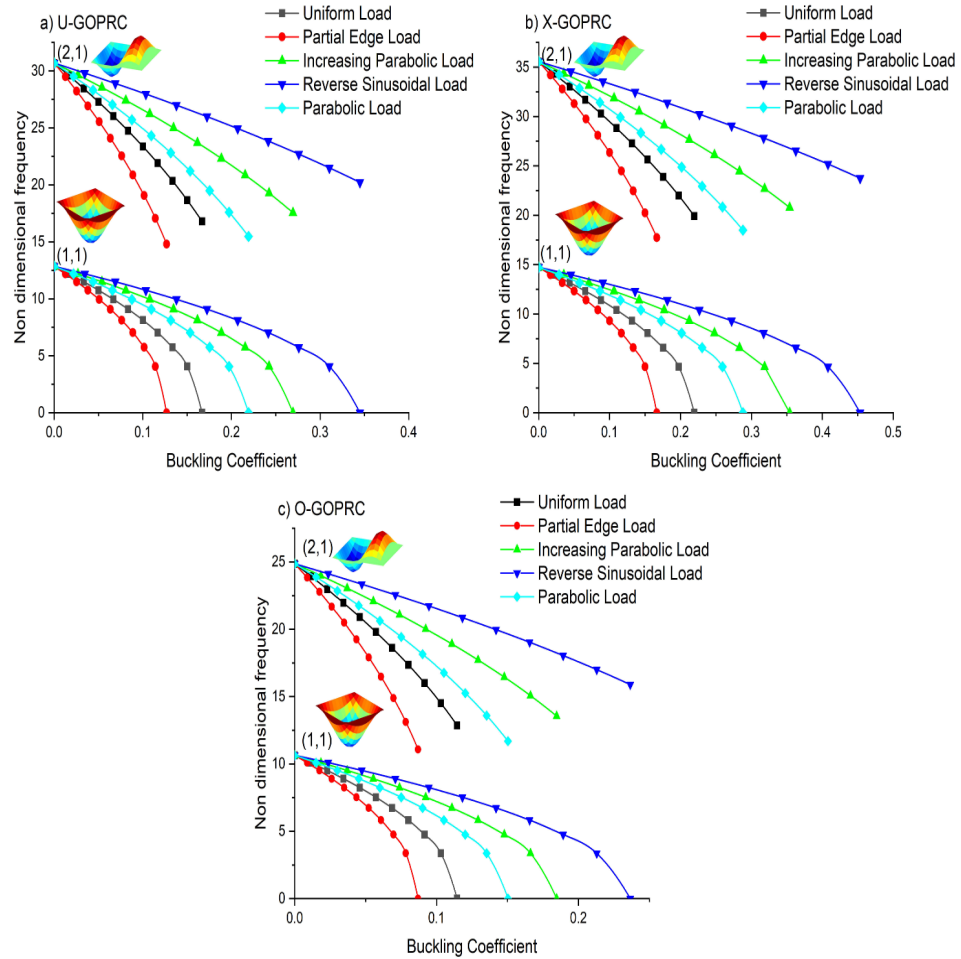


Figure 6.8: Non dimensional frequency ($\Omega = \omega_n \left(\frac{a^2}{h} \sqrt{\frac{\rho_m}{E_m}} \right)$) change for a simply supported GOP reinforced cylindrical panel (aspect ratio 1) : Influence of increase in compressive load.

To get more insight into the influence of type of loading on the vibration characteristics of GOP reinforced cylindrical panel, the change in frequencies with increase in load for aspect ratio 1.3 is plotted in Figure 6.9. The natural frequency reduction with compressive load increase is observed similar to aspect ratio 1 for loads except partial edge loading and parabolic loading. The free vibration frequency change with compressive load increase for partial edge loading and parabolic loading is such that

nearby critical buckling load, the frequency corresponding to (2,1) mode reduces to zero instead of frequency of (1,1) mode. The explanation of the behaviour is given as follows: for parabolic and partial edge loading, when aspect ratio is 1.3, the mode corresponding to minimum buckling load is (2,1) instead of (1,1). Consequently, near by critical buckling load, the free vibration mode (1,1) changes to (2,1). On the other hand, corresponding to critical buckling load, (1,1) is the buckling mode for all the other loading conditions. As a consequence, there is no change in free vibration mode and also (1,1) mode reduces to zero at critical buckling load. The main reason for resemblance between buckling mode and free vibration mode near critical buckling load is due to the fact that, nearby critical buckling load a minimum amount of energy is required for the vibration mode shape which exactly same as buckling mode shape. Thus for aspect ratio 1.3, free vibration mode shift from (1,1) to (2,1) occurs only for the case of parabolic and partial edge loading.

6.4.2.3 Comparison of Buckling Loads for Different Types of Nano Filler Reinforced Cylindrical Panels

The comparison of buckling load per unit mass ($\frac{N_{cr}}{I_{1ab}}$) of the cylindrical panel for UEL under the influence of different types of materials analyzed in the present study is presented in this section. The cylindrical panel with $\frac{a}{b} = 1$, $\frac{a}{h} = 100$ and $\frac{R}{a} = 20$ under simply supported boundary condition is considered for this comparison study. Effect of volume fraction on the buckling load per unit mass of the cylindrical panel is shown in Figure 6.10. Four different types of cylindrical panels namely, porous GPL reinforced cylindrical panel, sandwich cylindrical panel with porous GPL core, GOP reinforced cylindrical panel and CNT reinforced cylindrical panel are considered. For comparison purposes, the epoxy matrix given in Section 6.4 is considered for all the different kinds of cylindrical panels. For porous cylindrical panels, small amount of porosity ($e_0 = 0.2$) is considered. $e_0 = 0.2$ is selected to compare the lightweight nature of GPL porous cylindrical panel and GPL porous sandwich cylindrical panel. It is seen that in

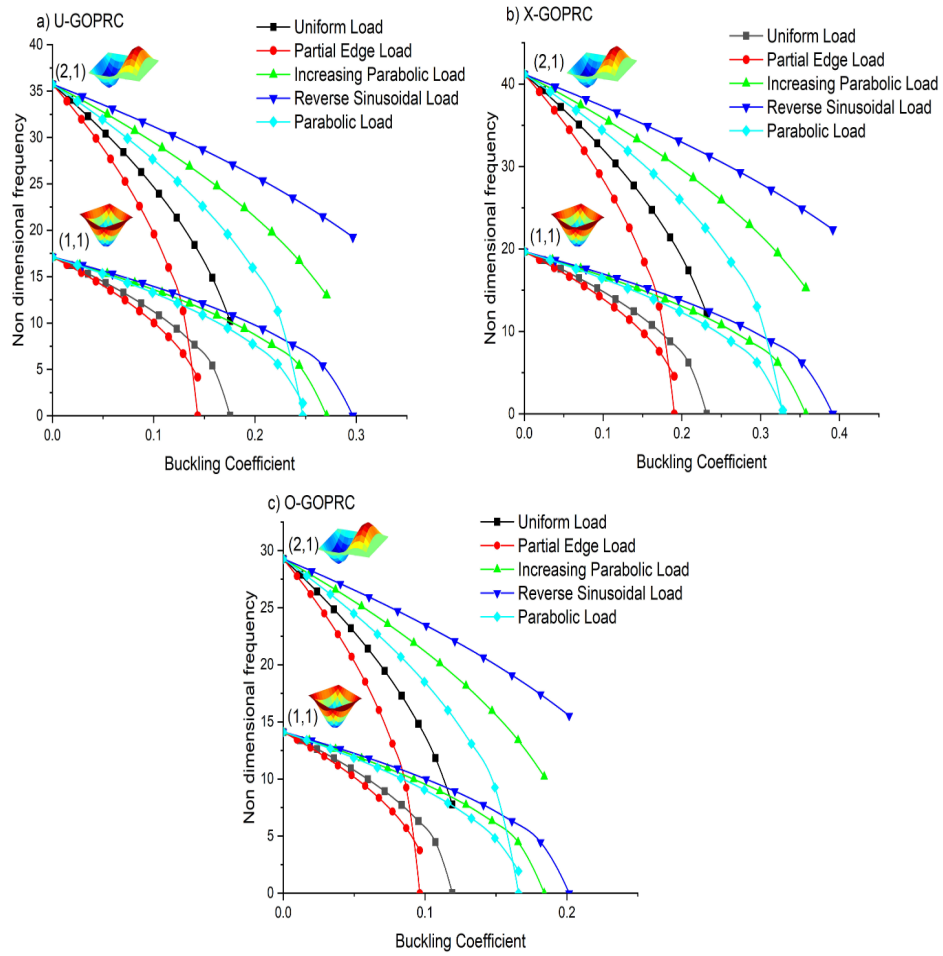


Figure 6.9: Non dimensional frequency ($\Omega = \omega_n \left(\frac{a^2}{h} \sqrt{\frac{\rho_m}{E_m}} \right)$) change for a simply supported GOP reinforced cylindrical panel (aspect ratio 1.3) : Influence of increase in compressive load.

the absence of nano reinforcement, buckling strength per unit mass is high for sandwich cylindrical panel with decreasing porosity distribution. This is due to the ability of sandwich cylindrical panel with porous core in reducing the overall weight without much reduction in stiffness. Furthermore, with increase in volume fraction of nano reinforcement, the buckling load per unit mass increases for all the cases. The GPL reinforced porous cylindrical panel with higher amount of GPL at the extreme surfaces exhibits high buckling load per unit mass value. This is expected as GPL enhances the

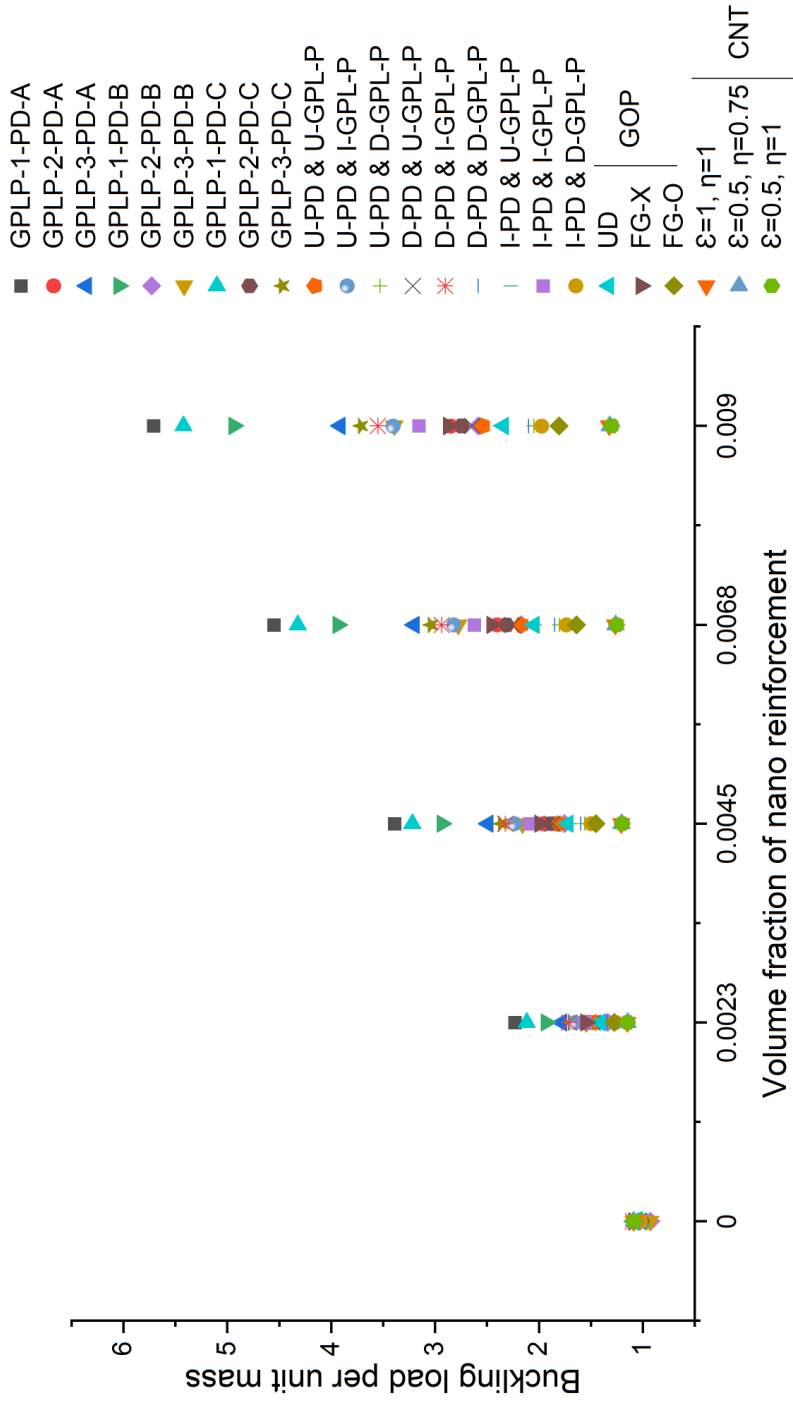


Figure 6.10: Comparison of buckling load per unit mass ($\frac{N_{cr}}{I_{1,ab}}$) for different nano composite cylindrical panels.

structural stiffness even at low concentrations. Next to the GPL reinforced cylindrical panel, the sandwich cylindrical panel with GPL reinforced porous core is having better buckling strength followed by this, the GOP reinforced reinforced cylindrical and the CNT reinforced cylindrical panels are having the lower buckling strength values.

Figure 6.11 depicts the variation in buckling load per unit mass with increase in porosity for GPL reinforced porous cylindrical panel and sandwich cylindrical panel with GPL reinforced porous core. The volume fraction of nano reinforcements is considered as a minimum i.e., 0.011. The GOP and CNT reinforced cylindrical panels are shown in the graph for comparison. In the absence of porosity, it is seen that highest value of buckling load per unit mass is observed for GPL reinforced cylindrical panel with maximum amount of GPL at the extreme surfaces. This is due to influence of GPL in improving the stiffness of the cylindrical panel. The next highest value of buckling load per unit mass is observed for sandwich cylindrical panel then followed by GOP reinforced cylindrical panel and finally CNT reinforced cylindrical panel. The increase in porosity lead to a small reduction in buckling load per unit mass for all the case. This is because the increase in porosity lead to a reduction in structural stiffness of the cylindrical panel.

6.5 Closure

The investigation carried out on dynamic and buckling characteristics of GOP embedded composite cylindrical panel under different edge loadings are presented. Three different type of GOP distribution namely, O-GOPRC, X-GOPRC and U-GOPRC are considered. The influence of GOP distribution and concentration, aspect ratio and nature of different type of edge loading on the vibration and buckling response is analyzed in detail. The buckling strength of GOP reinforced cylindrical panel is largely influenced by the type of GOP distribution. Highest buckling coefficient value is observed for X-GOPRC distribution and lowest for O-GOPRC distribution. The buckling

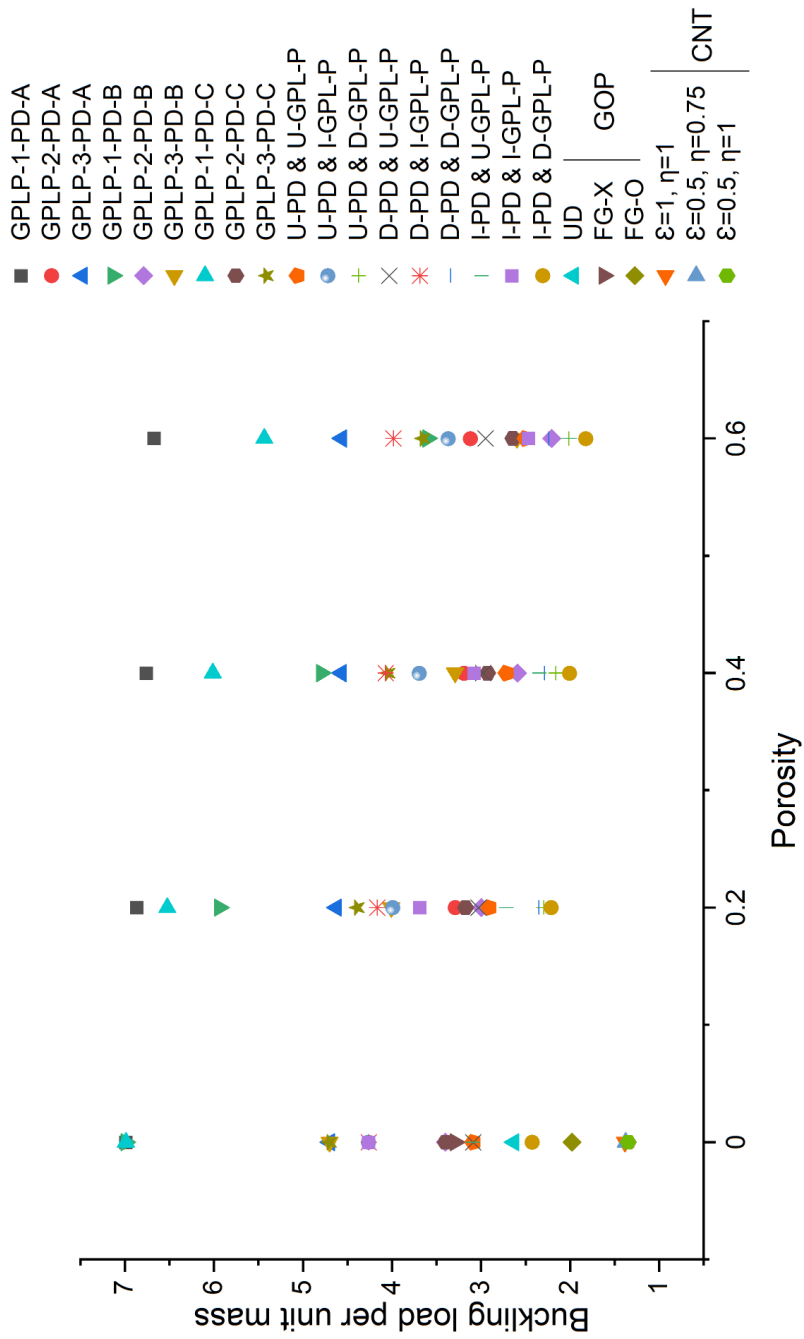


Figure 6.11: Comparison of buckling load per unit mass ($\frac{N_{cr}}{I_{1,ab}}$) for different nano composite cylindrical panels.

strength enhances by 100 % for X-GOPRC distribution, 70 % for U-GOPRC and 40 % for O-GOPRC with the addition of 0.5 weight fraction of GOP. The type of edge loading alters the critical buckling load value significantly. The lowest buckling load value belongs to partial edge loading while highest value belongs to reverse sinusoidal loading. An increase in weight fraction of GOP leads to compelling increasing in buckling coefficient of GOP reinforced composite cylindrical panel. The lowest buckling mode of the cylindrical panel becomes (2,1) from (1,1) at some aspect ratios depending upon the type of loading. For the partial edge loading the shift happens at very low aspect ratio while it happens at high aspect ratio for reverse sinusoidal loading. A significant increase in free vibration frequency is observed with an increase in GOP weight fraction. X-GOPRC distribution leads to higher natural frequency and O-GOPRC distribution of GOP notes the lowest natural frequency. A reduction in frequencies with increase in compressive load for a nano composite cylindrical panel depends largely on the type of edge loading. The partial edge loading leads to higher reduction while lowest reduction is observed for reverse sinusoidal loading. A change in fundamental free vibration mode in presence of compressive load is observed for partial edge loading and parabolic loading. Nearby critical buckling load, free vibration mode changes from (1,1) to (2,1) for parabolic and partial edge loadings for a nano composite cylindrical panel at aspect ratio 1.3.

CHAPTER 7

SUMMARY AND CONCLUSIONS

7.1 Summary

The buckling and free vibration characteristics of different types of nano composite cylindrical panels subjected to uniform and different NELs are presented. The usage of nano composite reinforced structures for various structural application leads to significant reductions in overall weight of the structure without compromising the stiffness. Considering a higher order shear deformation theory, Hamilton's principle is used to formulate the governing partial differential equations and buckling and free vibration solutions are obtained by employing the semi analytical method based on Galerkin's method. Initially, the membrane stress resultants due to the applied edge loads are calculated through Airy's stress function expansion. The Eigen value problems of buckling and free vibration are obtained by utilizing semi analytical solution method on the governing differential equations.

Firstly, buckling and free vibration characteristics of GPL reinforced porous cylindrical panel subjected to uniform and different NELs are investigated. The influences of grading patterns of GPL, porosity coefficient on buckling and dynamic characteristics of functionally graded GPL reinforced porous cylindrical panel under uniform and non-uniform in-plane loads are investigated. Then, the buckling and free vibration characteristics of sandwich cylindrical panel with GPL reinforced porous core are also investigated. The influence of different distributions of GPL and porosity, core to total thickness ratio, radius of curvature, GPL weight fraction, porosity coefficient on buckling and free vibration characteristics are analysed. The size dependent buckling and free vibration behaviour of CNT reinforced cylindrical nano panel considering agglom-

eration considering non local elasticity theory is investigated next. The influence of non-local parameter, CNT agglomeration, non-uniform in-plane loads on buckling, and free vibration response is presented next. Finally, the buckling characteristics of GOP embedded composite cylindrical panel is investigated. The influence of GOP distribution and concentration, aspect ratio and nature of different type of edge loading on the vibration and buckling response is analyzed in detail.

7.2 Conclusions

The following conclusions are made :

7.2.1 Free Vibration-Buckling Analysis on GPL-Porous Cylindrical Panel

- The type of NEL greatly influences the critical buckling load of the panel. Highest critical buckling load is observed for partial tension loading and the lowest critical buckling load is observed for the uniform edge load.
- The buckling coefficients and natural frequencies varies according to the particular combination of porosity and GPL distributions. The maximum buckling strength and free vibration resistance is observed for GPLP-1-PD-A combination.
- The buckling and free vibration parameters are influenced by changes in the porosity coefficient and porosity grading pattern. The maximum reduction in stiffness is observed for porosity distribution B while porosity distribution A has minimum reduction in stiffness, with increase in porosity.
- The critical buckling mode of functionally graded GPL reinforced porous cylindrical panel is influenced by the aspect ratio of the panel.

7.2.2 Free Vibration-Buckling Analysis on GPL-Porous Sandwich Cylindrical Panel

- The critical buckling load is largely influenced by the type of NEL and uniform loading has the minimum value while partial tension loading possesses the maximum value.
- The sandwich cylindrical panel with D-PD & I-GPL-P core has the higher buckling resistance and better free vibration frequency while the panel with I-PD & D-GPL-P core has the lower values.
- The enhancement in buckling resistance and free vibration frequency with respect to core to total thickness ratio depends on the amount of porosity in the core.
 - For the low porosity coefficient, in the presence of high GPL content the buckling coefficient and free vibration frequency increases with the core to total thickness ratio.
 - For the high porosity coefficient, in the presence of high GPL content the variation of buckling coefficient and free vibration frequency depending on porosity distribution and GPL pattern.
- The shifting of buckling mode shape from (1,1)(single half wave) to (2,1) (double half wave) occurs at different values of aspect ratio for different loads.
- The reduction of natural frequency with increase in compressive load intensity depends on the type of the non-uniform edge load.

7.2.3 Free Vibration-Buckling Analysis on CNT Reinforced Cylindrical Panel

- The buckling response of cylindrical nano panel depends primarily on the non-local parameter, type of edge load and degree of CNT agglomeration.
- The free vibration frequency of cylindrical nano panel depends largely on non-local parameter, degree of CNT agglomeration and boundary conditions.
- The critical buckling load is influenced by the type of edge load. The highest value of buckling load is observed for partial tension loading and the lowest value is observed for uniformly distributed load.
- For the CNT reinforced cylindrical nano panel, the consideration of size effect reduces the stiffness thus the buckling load and free vibration frequencies are reduced.
- The reduction in natural frequency with the increase in buckling load is different for various NELs. The reduction rate is high for the uniform load case and low for partial tension loading.

7.2.4 Free Vibration-Buckling Analysis on GOP Reinforced Cylindrical Panel

- The buckling strength of GOP reinforced cylindrical panel is largely influenced by the type of GOP distribution. Highest buckling coefficient value is observed for X-GOPRC distribution and lowest value occurs for O-GOPRC distribution.
- The buckling strength is enhanced by 100 % for X-GOPRC distribution, 70 % for U-GOPRC and 40 % for O-GOPRC with the addition of 0.5 weight fraction of GOP.

- The type of edge loading alters the critical buckling load value. The lowest buckling load value belongs to partial edge loading while highest value belongs to reverse sinusoidal loading.
- The lowest buckling mode of the cylindrical panel becomes (2,1) from (1,1) at different aspect ratios depending upon the type of loading. For partial edge loading the shift happens at very low value of aspect ratio while it happens at higher aspect ratio for reverse sinusoidal loading.
- X-GOPRC distribution leads to higher natural frequency and O-GOPRC distribution of GOP notes the lowest natural frequency.
- A reduction in frequencies with increase in compressive load for a nano composite cylindrical panel depends largely on the type of edge loading. The partial edge loading leads to higher reduction while lowest reduction is observed for reverse sinusoidal loading.
- A change in fundamental free vibration mode in presence of compressive load is observed for partial edge and parabolic loading cases.
- Nearby critical buckling load, free vibration mode changes from (1,1) to (2,1) for parabolic and partial edge loadings for a nano composite cylindrical panel at aspect ratio 1.3.

7.3 Scope for Future Work

The current research work analyses the buckling and free vibration characteristics of various light weight cylindrical panel structures under the influence of uniform and non uniform edge loads. Various future extensions of the present work can be summarised as:

- The buckling and free vibration characteristics of nano composite structures under various multi physics loadings such as hygrothermal loading, thermal loading and supersonic air flow can be studied.
- Non linear vibration and buckling characteristics of these nano composite structures can be studied.
- Vibro acoustic characteristics of nano composite cylindrical panels under various multi physics loadings including non uniform edge loads can be studied.

REFERENCES

- Abolghasemi, S., H. Eipakchi, and M. Shariati (2019). An analytical solution for buckling of plates with circular cutout subjected to non-uniform in-plane loading. *Archive of Applied Mechanics*, 89(12), 2519–2543.
- Adhikari, B., P. Dash, and B. Singh (2020). Buckling analysis of porous fgm sandwich plates under various types nonuniform edge compression based on higher order shear deformation theory. *Composite Structures*, 251, 112597.
- Adhikari, B. and B. Singh (2020). Parametric instability analysis of laminated composite plate subject to various types of non-uniform periodic in-plane edge load. *Applied Mathematics and Computation*, 373, 125026.
- Akbaş, Ş. D. (2017). Thermal effects on the vibration of functionally graded deep beams with porosity. *International Journal of Applied Mechanics*, 9(05), 1750076.
- Amir, M., S.-W. Kim, and M. Talha (2022). Comparative study of different porosity models for the nonlinear free vibration analysis of the functionally graded cylindrical panels. *Mechanics Based Design of Structures and Machines*, 1–27.
- Anamagh, M. R. and B. Bediz (2020). Free vibration and buckling behavior of functionally graded porous plates reinforced by graphene platelets using spectral chebyshev approach. *Composite Structures*, 253, 112765.
- Ansari, R., J. Torabi, and R. Hassani (2019). A comprehensive study on the free vibration of arbitrary shaped thick functionally graded cnt-reinforced composite plates. *Engineering Structures*, 181, 653–669.
- Arefi, M. (2020). Electro-mechanical vibration characteristics of piezoelectric nano shells. *Thin-Walled Structures*, 155, 106912.

- Ashby, M. F., T. Evans, N. A. Fleck, J. Hutchinson, H. Wadley, and L. Gibson, *Metal foams: a design guide*. Elsevier, 2000.
- Banhart, J. (2005). Aluminium foams for lighter vehicles. *International Journal of Vehicle Design*, 37(2-3), 114–125.
- Banhart, J., F. García-Moreno, K. Heim, and H.-W. Seeliger, Light-weighting in transportation and defence using aluminium foam sandwich structures. *In Light Weighting for Defense, Aerospace, and Transportation*. Springer, 2019, 61–72.
- Barati, M. R. and A. M. Zenkour (2019). Vibration analysis of functionally graded graphene platelet reinforced cylindrical shells with different porosity distributions. *Mechanics of Advanced Materials and Structures*, 26(18), 1580–1588.
- Bisheh, H. and Ö. Civalek (2020). Vibration of smart laminated carbon nanotube-reinforced composite cylindrical panels on elastic foundations in hygrothermal environments. *Thin-Walled Structures*, 155, 106945.
- Bisheh, H., T. Rabczuk, and N. Wu (2020). Effects of nanotube agglomeration on wave dynamics of carbon nanotube-reinforced piezocomposite cylindrical shells. *Composites Part B: Engineering*, 187, 107739.
- Bisheh, H. and N. Wu (2019). Wave propagation in piezoelectric cylindrical composite shells reinforced with angled and randomly oriented carbon nanotubes. *Composites Part B: Engineering*, 160, 10–30.
- Chakraborty, S., T. Dey, and R. Kumar (2019). Stability and vibration analysis of cnt-reinforced functionally graded laminated composite cylindrical shell panels using semi-analytical approach. *Composites Part B: Engineering*, 168, 1–14.
- Chen, D., J. Yang, and S. Kitipornchai (2016). Free and forced vibrations of shear deformable functionally graded porous beams. *International journal of mechanical sciences*, 108, 14–22.

Cheshmeh, E., M. Karbon, A. Eyvazian, D. w. Jung, M. Habibi, and M. Safarpour (2022). Buckling and vibration analysis of fg-cntrc plate subjected to thermo-mechanical load based on higher order shear deformation theory. *Mechanics Based Design of Structures and Machines*, 50(4), 1137–1160.

Civalek, Ö., S. Dastjerdi, and B. Akgöz (2022). Buckling and free vibrations of cnt-reinforced cross-ply laminated composite plates. *Mechanics Based Design of Structures and Machines*, 50(6), 1914–1931.

Coleman, J. N., U. Khan, W. J. Blau, and Y. K. Gun'ko (2006). Small but strong: a review of the mechanical properties of carbon nanotube–polymer composites. *Carbon*, 44(9), 1624–1652.

Daghigh, H. and V. Daghigh (2019). Free vibration of size and temperature-dependent carbon nanotube (cnt)-reinforced composite nanoplates with cnt agglomeration. *Polymer Composites*, 40(S2), E1479–E1494.

Daghigh, H., V. Daghigh, A. Milani, D. Tannant, T. E. Lacy Jr, and J. Reddy (2020). Nonlocal bending and buckling of agglomerated cnt-reinforced composite nanoplates. *Composites Part B: Engineering*, 183, 107716.

Dey, T. and L. Ramachandra (2014). Static and dynamic instability analysis of composite cylindrical shell panels subjected to partial edge loading. *International Journal of Non-Linear Mechanics*, 64, 46–56.

Dindarloo, M. H. and L. Li (2019). Vibration analysis of carbon nanotubes reinforced isotropic doubly-curved nanoshells using nonlocal elasticity theory based on a new higher order shear deformation theory. *Composites Part B: Engineering*, 175, 107170.

Dzenis, Y. (2008). Structural nanocomposites. *Science*, 319(5862), 419–420.

Ebrahimi, F. and M. R. Barati (2018). Vibration analysis of nonlocal strain gradient embedded single-layer graphene sheets under nonuniform in-plane loads. *Journal of Vibration and Control*, 24(20), 4751–4763.

- Ebrahimi, F., A. Dabbagh, and Ö. Civalek (2019). Vibration analysis of magnetically affected graphene oxide-reinforced nanocomposite beams. *Journal of Vibration and Control*, 25(23-24), 2837–2849.
- Ebrahimi, F., P. Hafezi, and A. Dabbagh (2021). Buckling analysis of embedded graphene oxide powder-reinforced nanocomposite shells. *Defence Technology*, 17(1), 226–233.
- Ebrahimi, F., M. Nouraei, and A. Dabbagh (2020). Modeling vibration behavior of embedded graphene-oxide powder-reinforced nanocomposite plates in thermal environment. *Mechanics Based Design of Structures and Machines*, 48(2), 217–240.
- Eringen, A. C. (1972). Nonlocal polar elastic continua. *International Journal of Engineering Science*, 10(1), 1–16.
- Eringen, A. C. (1983). On differential equations of nonlocal elasticity and solutions of screw dislocation and surface waves. *Journal of Applied Physics*, 54(9), 4703–4710.
- Eringen, A. C., *Nonlocal continuum field theories*. Springer Science & Business Media, 2002.
- Feng, C., S. Kitipornchai, and J. Yang (2017). Nonlinear free vibration of functionally graded polymer composite beams reinforced with graphene nanoplatelets (gpls). *Engineering Structures*, 140, 110–119.
- Ghasemi, A. R., M. Mohandes, R. Dimitri, and F. Tornabene (2019). Agglomeration effects on the vibrations of cnts/fiber/polymer/metal hybrid laminates cylindrical shell. *Composites Part B: Engineering*, 167, 700–716.
- Gibson, I. and M. F. Ashby (1982). The mechanics of three-dimensional cellular materials. *Proceedings of the Royal Society of London. A. Mathematical and Physical Sciences*, 382(1782), 43–59.
- Gibson, L. and M. Ashby (1999). *Cellular solids: Structure and properties*, cambridge univ.

Gunasekaran, V., J. Pitchaimani, and L. B. M. Chinnapandi (2020a). Analytical investigation on free vibration frequencies of polymer nano composite plate: Effect of graphene grading and non-uniform edge loading. *Materials Today Communications*, 24, 100910.

Gunasekaran, V., J. Pitchaimani, and L. B. M. Chinnapandi (2020b). Vibro-acoustics response of an isotropic plate under non-uniform edge loading: an analytical investigation. *Aerospace Science and Technology*, 105, 106052.

Haggenmueller, R., H. Gommans, A. Rinzler, J. E. Fischer, and K. Winey (2000). Aligned single-wall carbon nanotubes in composites by melt processing methods. *Chemical Physics Letters*, 330(3-4), 219–225.

Hamedani, S. J. and A. R. Ranji (2013). Buckling analysis of stiffened plates subjected to non-uniform biaxial compressive loads using conventional and super finite elements. *Thin-Walled Structures*, 64, 41–49.

Hedayati, H. and B. S. Aragh (2012). Influence of graded agglomerated cnts on vibration of cnt-reinforced annular sectorial plates resting on pasternak foundation. *Applied Mathematics and Computation*, 218(17), 8715–8735.

Hill, R. (1965). A self-consistent mechanics of composite materials. *Journal of the Mechanics and Physics of Solids*, 13(4), 213–222.

Hosseini-Hashemi, S., M. Kermajani, and R. Nazemnezhad (2015). An analytical study on the buckling and free vibration of rectangular nanoplates using nonlocal third-order shear deformation plate theory. *European Journal of Mechanics-A/Solids*, 51, 29–43.

Hu, Y.-G., K. M. Liew, Q. Wang, X. He, and B. Yakobson (2008). Nonlocal shell model for elastic wave propagation in single-and double-walled carbon nanotubes. *Journal of the Mechanics and Physics of Solids*, 56(12), 3475–3485.

Hummers Jr, W. S. and R. E. Offeman (1958). Preparation of graphitic oxide. *Journal of the American Chemical Society*, 80(6), 1339–1339.

- Jana, P. and K. Bhaskar (2006). Stability analysis of simply-supported rectangular plates under non-uniform uniaxial compression using rigorous and approximate plane stress solutions. *Thin-Walled Structures*, 44(5), 507–516.
- Jiao, P., Z. Chen, H. Ma, D. Zhang, and P. Ge (2019). Buckling analysis of thin rectangular fg-cntc plate subjected to arbitrarily distributed partial edge compression loads based on differential quadrature method. *Thin-Walled Structures*, 145, 106417.
- Jones, R. M., *Buckling of bars, plates, and shells*. Bull Ridge Corporation, 2006.
- Kamarian, S., M. Salim, R. Dimitri, and F. Tornabene (2016). Free vibration analysis of conical shells reinforced with agglomerated carbon nanotubes. *International Journal of Mechanical Sciences*, 108, 157–165.
- Kang, J.-H. and A. W. Leissa (2005). Exact solutions for the buckling of rectangular plates having linearly varying in-plane loading on two opposite simply supported edges. *International Journal of Solids and Structures*, 42(14), 4220–4238.
- Kiani, Y. (2017). Buckling of fg-cnt-reinforced composite plates subjected to parabolic loading. *Acta Mechanica*, 228(4), 1303–1319.
- Kumar, R., B. Banerjee, and L. Ramachandra (2016). Nonlinear stability and dynamics of composite skew plates under nonuniform loadings using differential quadrature method. *Mechanics Research Communications*, 73, 76–90.
- Lee, C., X. Wei, J. W. Kysar, and J. Hone (2008). Measurement of the elastic properties and intrinsic strength of monolayer graphene. *Science*, 321(5887), 385–388.
- Lei, J., Y. He, S. Guo, Z. Li, and D. Liu (2016). Size-dependent vibration of nickel cantilever microbeams: experiment and gradient elasticity. *Aip Advances*, 6(10), 105202.
- Leissa, A. W. and J.-H. Kang (2002). Exact solutions for vibration and buckling of an ss-c-ss-c rectangular plate loaded by linearly varying in-plane stresses. *International Journal of Mechanical Sciences*, 44(9), 1925–1945.

- Li, H., F. Pang, H. Chen, and Y. Du (2019a). Vibration analysis of functionally graded porous cylindrical shell with arbitrary boundary restraints by using a semi analytical method. *Composites Part B: Engineering*, 164, 249–264.
- Li, H., F. Pang, Y. Ren, X. Miao, and K. Ye (2019b). Free vibration characteristics of functionally graded porous spherical shell with general boundary conditions by using first-order shear deformation theory. *Thin-Walled Structures*, 144, 106331.
- Li, Q., D. Wu, X. Chen, L. Liu, Y. Yu, and W. Gao (2018). Nonlinear vibration and dynamic buckling analyses of sandwich functionally graded porous plate with graphene platelet reinforcement resting on winkler–pasternak elastic foundation. *International Journal of Mechanical Sciences*, 148, 596–610.
- Li, Z., Y. He, J. Lei, S. Han, S. Guo, and D. Liu (2019c). Experimental investigation on size-dependent higher-mode vibration of cantilever microbeams. *Microsystem Technologies*, 25, 3005–3015.
- Li, Z., J. Zheng, and Z. Zhang (2019d). Mechanics of the confined functionally graded porous arch reinforced by graphene platelets. *Engineering Structures*, 201, 109817.
- Lin, D., C. R. Liu, and G. J. Cheng (2014). Single-layer graphene oxide reinforced metal matrix composites by laser sintering: Microstructure and mechanical property enhancement. *Acta Materialia*, 80, 183–193.
- Liu, D., S. Kitipornchai, W. Chen, and J. Yang (2018). Three-dimensional buckling and free vibration analyses of initially stressed functionally graded graphene reinforced composite cylindrical shell. *Composite Structures*, 189, 560–569.
- Liu, F., P. Ming, and J. Li (2007). Ab initio calculation of ideal strength and phonon instability of graphene under tension. *Physical Review B*, 76(6), 064120.
- Liu, J., H. Yan, and K. Jiang (2013). Mechanical properties of graphene platelet-reinforced alumina ceramic composites. *Ceramics International*, 39(6), 6215–6221.

- Magnucka-Blandzi, E. (2008). Axi-symmetrical deflection and buckling of circular porous-cellular plate. *Thin-walled structures*, 46(3), 333–337.
- Mantari, J., A. Oktem, and C. G. Soares (2011). Static and dynamic analysis of laminated composite and sandwich plates and shells by using a new higher-order shear deformation theory. *Composite Structures*, 94(1), 37–49.
- Mittal, G., V. Dhand, K. Y. Rhee, S.-J. Park, and W. R. Lee (2015). A review on carbon nanotubes and graphene as fillers in reinforced polymer nanocomposites. *Journal of Industrial and Engineering Chemistry*, 21, 11–25.
- Moayedi, H., F. Ebrahimi, M. Habibi, H. Safarpour, and L. K. Foong (2021). Application of nonlocal strain–stress gradient theory and gdqem for thermo-vibration responses of a laminated composite nanoshell. *Engineering with Computers*, 37(4), 3359–3374.
- Naghsh, M. A., S. Sarrami-Foroushani, M. Azhari, and S. Mohajeri (2021). Static and dynamic instability analysis of tapered cntrc sandwich plates under uniform and non-uniform in-plane loadings using spline finite strip method. *Aerospace Science and Technology*, 110, 106514.
- Nguyen, T. N., C. H. Thai, H. Nguyen-Xuan, and J. Lee (2018). Nurbs-based analyses of functionally graded carbon nanotube-reinforced composite shells. *Composite Structures*, 203, 349–360.
- Panda, S. K. and L. Ramachandra (2010). Buckling of rectangular plates with various boundary conditions loaded by non-uniform inplane loads. *International Journal of Mechanical Sciences*, 52(6), 819–828.
- Phung-Van, P., Q. X. Lieu, H. Nguyen-Xuan, and M. A. Wahab (2017). Size-dependent isogeometric analysis of functionally graded carbon nanotube-reinforced composite nanoplates. *Composite Structures*, 166, 120–135.
- Pollien, A., Y. Conde, L. Pambaguian, and A. Mortensen (2005). Graded open-cell

- aluminium foam core sandwich beams. *Materials Science and Engineering: A*, 404(1-2), 9–18.
- Pourjabari, A., Z. E. Hajilak, A. Mohammadi, M. Habibi, and H. Safarpour (2019). Effect of porosity on free and forced vibration characteristics of the gpl reinforcement composite nanostructures. *Computers & Mathematics with Applications*, 77(10), 2608–2626.
- Qian, D., E. C. Dickey, R. Andrews, and T. Rantell (2000). Load transfer and deformation mechanisms in carbon nanotube-polystyrene composites. *Applied physics letters*, 76(20), 2868–2870.
- Qian, D., G. J. Wagner, and, W. K. Liu, M.-F. Yu, and R. S. Ruoff (2002). Mechanics of carbon nanotubes. *Applied Mechanics Reviews*, 55(6), 495–533.
- Rafiee, M. A., J. Rafiee, Z. Wang, H. Song, Z.-Z. Yu, and N. Koratkar (2009). Enhanced mechanical properties of nanocomposites at low graphene content. *ACS nano*, 3(12), 3884–3890.
- Rahimi, A., A. Alibeigloo, and M. Safarpour (2020). Three-dimensional static and free vibration analysis of graphene platelet–reinforced porous composite cylindrical shell. *Journal of Vibration and Control*, 26(19-20), 1627–1645.
- Ramteke, P. M. (2019). Effect of grading pattern and porosity on the eigen characteristics of porous functionally graded structure. *Steel and Composite Structures, An International Journal*, 33(6), 865–875.
- Reddy, J. (2000). Analysis of functionally graded plates. *International Journal for Numerical Methods in Engineering*, 47(1-3), 663–684.
- Reich, S., C. Thomsen, and J. Maultzsch, *Carbon nanotubes: basic concepts and physical properties*. John Wiley & Sons, 2008.

Safdari, M. and M. S. Al-Haik (2018). A review on polymeric nanocomposites: effect of hybridization and synergy on electrical properties. *Carbon-Based Polymer Nanocomposites for Environmental and Energy Applications*, 113–146.

Sayyad, A. S. and Y. M. Ghugal (2019). Static and free vibration analysis of laminated composite and sandwich spherical shells using a generalized higher-order shell theory. *Composite Structures*, 219, 129–146.

Shahgholian, D., M. Safarpour, A. Rahimi, and A. Alibeigloo (2020). Buckling analyses of functionally graded graphene-reinforced porous cylindrical shell using the rayleigh–ritz method. *Acta Mechanica*, 231(5), 1887–1902.

Shakir, M. and M. Talha (2022). Influence of material uncertainty on higher-order fg-gpls reinforced porous spherical panels under blast loading. *Thin-Walled Structures*, 176, 109319.

Shariyat, M. and K. Asemi (2014). 3d b-spline finite element nonlinear elasticity buckling analysis of rectangular fgm plates under non-uniform edge loads, using a micromechanical model. *Composite Structures*, 112, 397–408.

Shi, D.-L., X.-Q. Feng, Y. Y. Huang, K.-C. Hwang, and H. Gao (2004). The effect of nanotube waviness and agglomeration on the elastic property of carbon nanotube-reinforced composites. *Journal of Engineering Materials Technology*, 126(3), 250–257.

Singh, V., R. Vescovini, R. Kumar, S. Patel, and G. Watts (2022). Nonlinear vibration and instability of a randomly distributed cnt-reinforced composite plate subjected to localized in-plane parametric excitation. *Applied Mathematical Modelling*, 101, 453–480.

Smith, B., S. Szyniszewski, J. Hajjar, B. Schafer, and S. Arwade (2012). Steel foam for structures: A review of applications, manufacturing and material properties. *Journal of Constructional Steel Research*, 71, 1–10.

- Song, M., S. Kitipornchai, and J. Yang (2017). Free and forced vibrations of functionally graded polymer composite plates reinforced with graphene nanoplatelets. *Composite Structures*, 159, 579–588.
- Song, M., J. Yang, and S. Kitipornchai (2018). Bending and buckling analyses of functionally graded polymer composite plates reinforced with graphene nanoplatelets. *Composites Part B: Engineering*, 134, 106–113.
- Suk, J. W., R. D. Piner, J. An, and R. S. Ruoff (2010). Mechanical properties of monolayer graphene oxide. *ACS Nano*, 4(11), 6557–6564.
- Tao, C. and T. Dai (2021). Isogeometric analysis for postbuckling of sandwich cylindrical shell panels with graphene platelet reinforced functionally graded porous core. *Composite Structures*, 260, 113258.
- Teng, M. W. and Y. Q. Wang (2020). Nonlinear free vibration of rectangular plates reinforced with 3d graphene foam: Approximate analytical solution. *Results in Physics*, 17, 103147.
- Thang, P. T., T.-T. Nguyen, and J. Lee (2017). A new approach for nonlinear buckling analysis of imperfect functionally graded carbon nanotube-reinforced composite plates. *Composites Part B: Engineering*, 127, 166–174.
- Thang, P. T., T. Nguyen-Thoi, D. Lee, J. Kang, and J. Lee (2018). Elastic buckling and free vibration analyses of porous-cellular plates with uniform and non-uniform porosity distributions. *Aerospace Science and Technology*, 79, 278–287.
- Thang, P. T., T. N. Thoi, and J. Lee (2019). Closed-form solution for nonlinear buckling analysis of fg-cntrc cylindrical shells with initial geometric imperfections. *European Journal of Mechanics-A/Solids*, 73, 483–491.
- Thomson, W. T., *Theory of vibration with applications*. CRC Press, 2018.

Tjong, S. C. (2013). Recent progress in the development and properties of novel metal matrix nanocomposites reinforced with carbon nanotubes and graphene nanosheets. *Materials Science and Engineering: R: Reports*, 74(10), 281–350.

Toan Thang, P., T. Nguyen-Thoi, and J. Lee (2020). Mechanical stability of metal foam cylindrical shells with various porosity distributions. *Mechanics of Advanced Materials and Structures*, 27(4), 295–303.

Tornabene, F., N. Fantuzzi, M. Baccocchi, and E. Viola (2016). Effect of agglomeration on the natural frequencies of functionally graded carbon nanotube-reinforced laminated composite doubly-curved shells. *Composites Part B: Engineering*, 89, 187–218.

Van Do, V. N. and C.-H. Lee (2020). Static bending and free vibration analysis of multilayered composite cylindrical and spherical panels reinforced with graphene platelets by using isogeometric analysis method. *Engineering Structures*, 215, 110682.

Velasco-Santos, C., A. L. Martínez-Hernández, F. T. Fisher, R. Ruoff, and V. M. Castaño (2003). Improvement of thermal and mechanical properties of carbon nanotube composites through chemical functionalization. *Chemistry of Materials*, 15(23), 4470–4475.

Wang, A., H. Chen, Y. Hao, and W. Zhang (2018). Vibration and bending behavior of functionally graded nanocomposite doubly-curved shallow shells reinforced by graphene nanoplatelets. *Results in Physics*, 9, 550–559.

Wang, M., Y.-G. Xu, P. Qiao, and Z.-M. Li (2022a). Buckling and free vibration analysis of shear deformable graphene-reinforced composite laminated plates. *Composite Structures*, 280, 114854.

Wang, Y., K. Xie, and T. Fu (2020). Vibration analysis of functionally graded graphene oxide-reinforced composite beams using a new ritz-solution shape function. *Journal of the Brazilian Society of Mechanical Sciences and Engineering*, 42(4), 1–14.

- Wang, Y., K. Xie, T. Fu, and W. Zhang (2022b). A third order shear deformable model and its applications for nonlinear dynamic response of graphene oxides reinforced curved beams resting on visco-elastic foundation and subjected to moving loads. *Engineering with Computers*, 38(3), 2805–2819.
- Wang, Y. Q., C. Ye, and J. W. Zu (2019). Vibration analysis of circular cylindrical shells made of metal foams under various boundary conditions. *International Journal of Mechanics and Materials in Design*, 15(2), 333–344.
- Wang, Y. Q. and Z. Y. Zhang (2019). Bending and buckling of three-dimensional graphene foam plates. *Results in Physics*, 13, 102136.
- Wang, Y. Q. and H. L. Zhao (2019). Free vibration analysis of metal foam core sandwich beams on elastic foundation using chebyshev collocation method. *Archive of Applied Mechanics*, 89(11), 2335–2349.
- Watts, G., R. Kumar, S. Patel, and S. Singh (2021). Dynamic instability of trapezoidal composite plates under non-uniform compression using moving kriging based meshfree method. *Thin-Walled Structures*, 164, 107766.
- Wu, D., A. Liu, Y. Huang, Y. Huang, Y. Pi, and W. Gao (2018). Dynamic analysis of functionally graded porous structures through finite element analysis. *Engineering Structures*, 165, 287–301.
- Xie, Y., J. Lei, S. Guo, S. Han, J. Ruan, and Y. He (2022). Size-dependent vibration of multi-scale sandwich micro-beams: An experimental study and theoretical analysis. *Thin-Walled Structures*, 175, 109115.
- Xue, Y., G. Jin, X. Ma, H. Chen, T. Ye, M. Chen, and Y. Zhang (2019). Free vibration analysis of porous plates with porosity distributions in the thickness and in-plane directions using isogeometric approach. *International Journal of Mechanical Sciences*, 152, 346–362.

- Yaghoobi, H. and F. Taheri (2020). Analytical solution and statistical analysis of buckling capacity of sandwich plates with uniform and non-uniform porous core reinforced with graphene nanoplatelets. *Composite Structures*, 252, 112700.
- Yakobson, B. I. and P. Avouris, Mechanical properties of carbon nanotubes. *In Carbon nanotubes*. Springer, 2001, 287–327.
- Yang, J., D. Chen, and S. Kitipornchai (2018). Buckling and free vibration analyses of functionally graded graphene reinforced porous nanocomposite plates based on chebyshev-ritz method. *Composite Structures*, 193, 281–294.
- Yas, M., A. Pourasghar, S. Kamarian, and M. Heshmati (2013). Three-dimensional free vibration analysis of functionally graded nanocomposite cylindrical panels reinforced by carbon nanotube. *Materials & Design*, 49, 583–590.
- Young, R. J., I. A. Kinloch, L. Gong, and K. S. Novoselov (2012). The mechanics of graphene nanocomposites: a review. *Composites Science and Technology*, 72(12), 1459–1476.
- Zhang, Z., Y. Li, H. Wu, H. Zhang, H. Wu, S. Jiang, and G. Chai (2020). Mechanical analysis of functionally graded graphene oxide-reinforced composite beams based on the first-order shear deformation theory. *Mechanics of Advanced Materials and Structures*, 27(1), 3–11.
- Zhao, J., Q. Wang, X. Deng, K. Choe, R. Zhong, and C. Shuai (2019). Free vibrations of functionally graded porous rectangular plate with uniform elastic boundary conditions. *Composites Part B: Engineering*, 168, 106–120.
- Zheng, J., C. Zhang, F. Musharavati, A. Khan, T. A. Sebaey, and A. Eyvazian (2021). Forced vibration characteristics of embedded graphene oxide powder reinforced metal foam nanocomposite plate in thermal environment. *Case Studies in Thermal Engineering*, 101167.

Zhou, Z., Y. Ni, Z. Tong, S. Zhu, J. Sun, and X. Xu (2019). Accurate nonlinear buckling analysis of functionally graded porous graphene platelet reinforced composite cylindrical shells. *International Journal of Mechanical Sciences*, 151, 537–550.

LIST OF PUBLICATIONS

Journal Papers

1. Twinkle, C. M., & Pitchaimani, J. (2021). Free vibration and stability of graphene platelet reinforced porous nano-composite cylindrical panel: Influence of grading, porosity and non-uniform edge loads. *Engineering Structures*, 230, 111670.
2. Twinkle, C. M., & Pitchaimani, J. (2022). A semi-analytical nonlocal elasticity model for static stability and vibration behaviour of agglomerated CNTs reinforced nano cylindrical panel under non-uniform edge loads. *Applied Mathematical Modelling*, 103, 68-90.
3. Twinkle, C. M., & Pitchaimani, J. (2022). Static stability and vibration behavior of graphene platelets reinforced porous sandwich cylindrical panel under non-uniform edge loads using semi-analytical approach. *Composite Structures*, 280, 114837.
4. Twinkle, C. M., & Pitchaimani, J. (2022, June). Dynamic and buckling response modelling of functionally graded graphene oxide powder (GOP) reinforced cylindrical panels: Influence of GOP grading and non-uniformly, partially distributed edge loads. *Structures*, Vol. 40, pp. 840-854.

CURRICULUM VITAE

1. Name: **Twinkle C M**
2. Date of Birth: 25/08/1990
3. Permanent Address: Chettuthara House,
Kelamangalam P.O., Thakazhy
Alappuzha, Kerala
Pincode-688562
4. Educational Qualification:
 - 2012 **Bachelor of Technology**
Institution: Kerala University,
Trivandrum, Kerala, India
Specialization: Mechanical Engineering
 - 2017 **Master of Technology**
Institution: APJ Abdul Kalam
Technological University,
Trivandrum, Kerala, India
Specialization: Machine Design
 - 2022 **Doctor of Philosophy**
Institution: National Institute of Technology
Karnataka, Mangalore, Karnataka,
India
Registration Date: 08/07/2019
Thesis Submission Date: 30/08/2022
Viva-Voice Date: 18/04/2023